Fall 10-1-2021

Electrochemical Hydrogen Peroxide Generation with Anthraquinone Chemistry for Advanced Oxidation Process

Qianhong Zhu
Yale University Graduate School of Arts and Sciences, ashleyzhu0123@gmail.com

Abstract

Electrochemical Hydrogen Peroxide Generation with Anthraquinone Chemistry for Advanced Oxidation Process

Qianhong Zhu

2021

Hydrogen peroxide plays a critical role in many industrial applications, including chemical synthesis and environmental remediation. For example, in advanced oxidation process of water treatment, hydrogen peroxide is activated to hydroxyl radical by catalysts or UV light for non-selective and rapid degradation of non-biodegradable, toxic, recalcitrant organic micropollutants. Industrial anthraquinone process, which synthesizes hydrogen peroxide from hydrogen and oxygen gas in organic phase, requires intensive capital investment, expensive reactants, high energy inputs, and raises many environmental concerns. Electrochemical production of hydrogen peroxide with air, water and electricity as inputs has emerged as a promising alternative method because it is low-cost, easy-to-operate, and environmentally-friendly. It would also greatly reduce the costs and dangers related to handling and transportation of commercial concentrated hydrogen peroxide solution and it can be potentially used for in-situ advanced oxidation process in decentralized water treatment applications. However, electrocatalyst synthesis, electrochemical reactor design, and H_2O_2 activation method all require significant improvement for real world usage.

For electrocatalyst development, we propose to transfer anthraquinone's homogeneous chemistry to heterogeneous interfaces. Most of the electrocatalysts reported have either low selectivity or low overall production and accumulation, as their environmental applications are hindered by the unclear reaction mechanism and uncontrolled material structure. We expect to produce hydrogen peroxide at the well-defined reactive sites selectively and stably. Anthraquinone molecular catalyst is attached to conductive substrates to construct immobilized heterogeneous electrocatalysts, and their performance under various electrochemical conditions are measured and optimized. The electro-driven anthraquinone is hydrogenated and oxidized sequentially to produce hydrogen peroxide, as in industrial processes. Various conductive supports with high electron mobility, stability with reduction potential, and compatibility with peroxide are investigated, including polymeric carbon nitride and conductive polymers. The material characterizations prove that anthraquinone can be chemically attached to conductive substrates with a facile, one-step synthesis method, and both catalytic composites show capacities of producing H_2O_2 with high activity and selectivity.

For device-level optimization, two different electrode configurations, immersed electrode and gas diffusion electrode, are tested for their electrochemical performance respectively. Due to the oxygen mass transport limitation in the liquid phase, GDE electrode architecture is expected to boost the electrocatalytic activity and selectivity due to the formation of gas-liquid-solid triple phase boundary layer. We here present an electrochemical H_2O_2 generation cell that produces 1.8 mol $g_{catalyst}^{-1}$ hr^{-1} at 100 mA with a Faradaic efficiency of 96%. Our calculation indicates that H_2O_2 production consumes only 0.2 to 20% of the total electricity consumption of AOPs in various AOP application scenarios employing UV activation. We also demonstrate the H_2O_2

production capability of the device with simulated drinking water and wastewater as feed electrolytes to demonstrate its potential for real-world operation scenarios.

For H_2O_2 activation in an AOP system, we further explore the possibilities of activating H_2O_2 with no chemical input and with no or little energy input by utilizing a heterogeneous Fenton catalyst, iron oxychloride (FeOCl) in two configurations: packed bed reactor and electro-Fenton reactor. In packed bed reactor, FeOCl is loaded to molecular sieve substrate as heterogeneous catalyst for Fenton reaction, where H_2O_2 is activated to hydroxyl radical; in electro-Fenton reactor, FeOCl is loaded to conductive carbon substrate as electrocatalyst for electrochemically-driven Fenton-like reaction. Both reactors exhibit capacities to degrade the model contaminant compound. Based on these results, future research directions are outlined to fully realize the research goal of modular, electrified, and decentralized water treatment with in-situ H_2O_2 generation and in-situ H_2O_2 activation.

Electrochemical Hydrogen Peroxide Generation with Anthraquinone Chemistry for Advanced Oxidation Process

A Dissertation

Presented to the Faculty of the Graduate School

Of

Yale University

in Candidacy for the Degree of

Doctor of Philosophy

By

Qianhong Zhu

Dissertation Director: Jaehong Kim

December 2021

# ACKNOWLEDGEMENTS

I owe immense thanks to many people who have supported, encouraged, and cared for me during this five-year journey. Getting Ph.D. is never an easy path and I am so lucky to be surrounded by so much love.

First I would like to express my deep gratitude to my Ph.D. advisor Dr. Jaehong Kim. Thank you for never giving me up and for always emphasizing how capable I am. Your unconditional trust and support mean so much to me and shaped me into a more confident and competent self. Your timely advice, meticulous scrutiny, and scientific insights have helped me build a solid foundation for my future academic career.

My sincere thank also goes to Prof. Shu Hu for offering me guidance and education during my first 1.5 years. Thank you for leading me to the world electrocatalysis and for encouraging me to explore the various possibilities in science. I also thank my committee member Dr. John Fortner for your availability and guidance throughout my Ph.D.

My work benefitted greatly from the invaluable contributions from my collaborators. Dr. Zhenhua Pan – thank you for answering all my questions and I miss playing Pokemon Go with you around New Haven and West Haven. Marlena Hinkle – you are such an lovely person to work with and see you soon at Stanford. David Kim – it's been a pleasure learning electrochemistry and having wonderful discussions about H_2O_2 with you.

I want to thank all the Kim lab's members that I've worked with. Chiheng – thank you for the ceaseless "pushes" that stimulated my scientific growth. Xuechen – I will miss the discussions, complains, and teases we shared and the wonderful camaraderie we established over the past five years. Haoran and Mohan – I will always remember our roommate years and the

food, game, laughter, and joy we had together. Dahong – I really appreciate your trust and invitation as a collaborator in many of your work at Yale. Shuo – it's so kind of you to always generously offer me compliments and academic advice. Beza, Anna, Stephanie, Min Jeong, Eric – I feel so lucky to have all of you to look up to in the group. You are all amazing role models to me, professionally and personally, and I am truly honored to be your colleague. Brenna – I could not have asked for better friend and I would not have made it without you.

Additionally, I would like to thank the friends and colleagues in Chemical and Environmental Engineering Department. Jiahui – you are such an amazing friend and I will remember all that you have done for me for my life. Georges – I learned a lot about courage and proper use of English word from you. Eric, Cass, An – we will support each other for more than this five years. Julianne and Mary Kate– you truly inspired and encouraged me to speak up in discussions about diversity, equity, and inclusion and to become a better person who care and a better citizen who act.

I would like to acknowledge the tremendous help from the staff members at Yale: Dr. Min Li from Yale West Campus Material Characterization Core (MCC), Dr. Eric Paulson from Yale Chemical and Biophysical Instrumentation Center (CBIC), Dr. Terence Wu from West Campus Analytical Core (WCAC), Vincent Bernado from Gibbs Machines Shop, Daryl Smith and Preston Smith from Glass shop. Thank you for teaching me how to operate instruments as well as materializing all the reactor designs. I also wish to thank the administrative staff in SEAS and CEE for all their hard, uncelebrated work.

I benefited a lot from my volunteer experience at Yale Peabody Museum of Natural History, where I've acquired much scientific knowledge and public speaking experience and become a better science educator. I would like to thank Stephanie Wratten, Andrea Motto, and

Ben Gibson for offering me the opportunity and trainings, Jim Sirch and Stefan Nicolescu for their invaluable teaching.

I feel obliged to thank all the other friends from all over the world. Jane, Chunnan, Ara, Zhifan, Yulu, Yinyi, Yongwei, Pengzi, Zishi – thank you for the trips, visits, phone calls, text messages that brightened my day and for the accompany on this journey.

I thank Yueshen for embracing all sides of me and for always being my biggest fan. Your understanding, trust, and love escorted me through all the ups and downs. Thank you for being such a perfect man in my life.

Finally I would like to thank my parents, Ziyu Liu and Gang Zhu, for their financial and emotional support, constant encouragement and love. Thank you both for giving me courage and strength to chase my dreams and to keep up when struggles become too overwhelming. I would not have come this far without you and you deserve as much compliment as I do.

Table of Contents

List of Figures

List of Tables

Chapter 1: Statement of Problem

1.1 Statement of problem

Hydrogen peroxide (H_2O_2) is a widely used chemical with a broad range of applications in chemical, medical, and environmental industries.[1] Since H_2O_2 is an environment-friendly oxidant and generates only water and oxygen as by-products, it is commonly used in advanced oxidation process (AOP) in water and wastewater treatment. In AOP, H_2O_2 are used are precursors to produce hydroxyl radicals via UV irradiation or catalyst activation,[2-4] and hydroxyl radicals are one of the most powerful oxidants to degrade a wide range of toxic, recalcitrant contaminants including solvents, hydrocarbons, industrial chemicals, pharmaceuticals, etc., that cannot be easily removed by biological methods.[5]

Industrial hydrogen peroxide production is mainly based on anthraquinone (AQ) process, where 2-alkylanthraquinone (R-AQ) is first hydrogenated by reacting with H_2 gas on a noble metal catalyst surface in organic solvent phase, and then R-AQ was auto-oxidized by O_2 gas back to AQ with concomitant H_2O_2 production.[1] However, this process requires expensive hydrogen gas and noble metal, toxic organic solvents, and high energy input for separation,[6] which make H_2O_2 production far from being carbon neutral within its life cycle and significantly limit its potential environmental applications.[7] The high costs and hazards associated with storage and transportation of commercially concentrated H_2O_2, in addition to environmental concerns, call for facile and sustainable H_2O_2 generation with low energy input and low-cost, ecofriendly catalysts.

Can H_2O_2 be produced in a green and carbon-neutral way such that it is sustainable throughout its life cycle? Can H_2O_2 be produced via electrochemical methods that require only electricity, oxygen in air, and water as inputs? Can such production be competitive with the established industrial processes? Can H_2O_2 be produced at point of use for in-situ water treatment with AOP? Can H_2O_2 be activated without additional chemical input and with no or low energy consumption? The goal of this research is to answer these questions by developing an electrochemical H_2O_2 production device and an H_2O_2 activation device as an alternative, green, and sustainable technology of choice.

Recently, non-metal electrocatalysts have been reported as promising candidates, such as carbon catalysts,[8-10] modified graphite felt,[11-12] nitrogen-doped porous carbon,[13-15] boron nitride in carbon materials,[16] reduced graphene oxide,[17] etc. However, most of these materials were utilizing nitrogen or oxygen-containing functional groups, sp^3-C hybridization, or “defects” as catalytic sites and could not precisely control catalyst structures or functionality densities to manipulate and optimize their electrochemical activities.

Therefore, the central idea of this research is to leverage the exceptional selectivity of the AQ chemistry for electrochemical H_2O_2 production; i.e., different from the industrial process, the homogeneous AQ catalysts are immobilized onto heterogeneous surfaces of electrocatalysts such that AQ chemistry is electricity-driven. Previous works of catalysts with anthraquinone as reacting centers[18-21] were suffering from either low production and efficiency or high overpotential for operation, possibly due to low AQ loading or unstable and H_2O_2-uncompatible conductive substrates. Although some materials show high current density efficiency (>90%) for 2-electron oxygen reduction in rotating-disk tests, it is difficult to detect the expected amount of H_2O_2 during electrolysis for a prolonged experiment due to oxygen transport limitation or self-disproportion. Therefore, we expected to immobilize AQ molecules on stable and H_2O_2-friendly substrates as heterogeneous electrocatalysts for H_2O_2 generation and accumulation.

In addition to catalyst development, we will also focus on constructing a more effective electrochemical cell design with gas diffusion electrode architecture. The device demonstration is critical for moving forward the proposed sustainable production and use of H_2O_2 because if its industrial-scale production can be adapted to a variable-scale and spatially-distributed production, one can generate this water-treatment reagent wherever electricity is available. Current researches on electrochemical reactors focus on the performance in synthetic, clean matrix and neglect many complications in real-world scenarios. We aim to develop an electrochemical H_2O_2 generation module and perform it in complicated water matrices to test for its feasibility in decentralized water treatment applications.[22]

We will also explore the possibility of developing a H_2O_2 activation module with little or no energy consumption and no chemical input. We propose to take advantage of the efficient redox cycle of a novel Fenton catalyst iron oxychloride (FeOCl),[23-24] and test its performance as substrate-supported heterogeneous catalyst in a packed reactor, and as a conductor-supported electrocatalyst in an electrochemical cell. We expect that both designs will efficiently active hydrogen peroxide to hydroxyl radicals for the oxidation and degradation of organic micropollutants, and both systems will not need additional chemical supply and significantly reduce the energy requirement compared with the benchmark UV process.

Therefore, the ultimate goal of this research is to develop an autonomous, electrified, modular, and chemical-free system for in-situ water treatment applications. The proposed research mainly aims to 1) develop anthraquinone modified electrocatalyst for hydrogen peroxide generation via oxygen reduction reaction; 2) understand reaction mechanisms and optimize material's electrochemical performance; 3) design electrochemical generation modules for H_2O_2 electrosynthesis; 4) prepare H_2O_2 activation catalysts and reactors for advanced oxidation process.

1.2 References

1. Campos-Martin, J. M.; Blanco-Brieva, G.; Fierro, J. L. G. Hydrogen Peroxide Synthesis: An Outlook beyond the Anthraquinone Process. *Angewandte Chemie International Edition* **2006,** *45* (42), 6962-6984.

2. Raj, C. B. C.; Quen, H. L. Advanced oxidation processes for wastewater treatment: Optimization of UV/H_2O_2 process through a statistical technique. *Chem Eng Sci* **2005,** *60* (19), 5305-5311.

3. Nguyen, T. T. M.; Park, H. J.; Kim, J. Y.; Kim, H. E.; Lee, H.; Yoon, J.; Lee, C. Microbial Inactivation by Cupric Ion in Combination with H_2O_2: Role of Reactive Oxidants. *Environ Sci Technol* **2013,** *47* (23), 13661-13667.

4. Ruppert, G.; Bauer, R. UV-O_3, UV-H_2O_2, UV-TiO_2 and the photo-Fenton reaction - comparison of advanced oxidation processes for wastewater treatment. *Chemosphere* **1994,** *28* (8), 1447-1454.

5. Miklos, D. B.; Remy, C.; Jekel, M.; Linden, K. G.; Drewes, J. E.; Hübner, U. Evaluation of advanced oxidation processes for water and wastewater treatment – A critical review. *Water Research* **2018,** *139*, 118-131.

6. Hâncu, D.; Green, J.; Beckman, E. J. H_2O_2 in CO_2/H_2O Biphasic Systems: Green Synthesis and Epoxidation Reactions. *Industrial & Engineering Chemistry Research* **2002,** *41* (18), 4466-4474.

7. Althaus, H. J.; Chudacoff, M.; Hischier, R.; Jungbluth, N.; Osses, M.; Primas, A. *Life Cycle Inventories of Chemicals*; 2007.

8. Čolić, V.; Yang, S.; Révay, Z.; Stephens, I. E. L.; Chorkendorff, I. Carbon catalysts for electrochemical hydrogen peroxide production in acidic media. *Electrochimica Acta* **2018,** *272*, 192-202.

9. Liu, Y.; Quan, X.; Fan, X.; Wang, H.; Chen, S. High-Yield Electrosynthesis of Hydrogen Peroxide from Oxygen Reduction by Hierarchically Porous Carbon. *Angewandte Chemie* **2015,** *127* (23), 6941-6945.

10. Gao, G.; Zhang, Q.; Hao, Z.; Vecitis, C. D. Carbon Nanotube Membrane Stack for Flow-through Sequential Regenerative Electro-Fenton. *Environ Sci Technol* **2015,** *49* (4), 2375-2383.

11. Zhou, L.; Zhou, M.; Hu, Z.; Bi, Z.; Serrano, K. G. Chemically modified graphite felt as an efficient cathode in electro-Fenton for p-nitrophenol degradation. *Electrochimica Acta* **2014,** *140*, 376-383.

12. Pan, Z.; Wang, K.; Wang, Y.; Tsiakaras, P.; Song, S. In-situ electrosynthesis of hydrogen peroxide and wastewater treatment application: A novel strategy for graphite felt activation. *Applied Catalysis B: Environmental* **2018,** *237*, 392-400.

13. Sun, Y.; Sinev, I.; Ju, W.; Bergmann, A.; Dresp, S.; Kühl, S.; Spöri, C.; Schmies, H.; Wang, H.; Bernsmeier, D.; Paul, B.; Schmack, R.; Kraehnert, R.; Roldan Cuenya, B.; Strasser, P. Efficient Electrochemical Hydrogen Peroxide Production from Molecular Oxygen on Nitrogen-Doped Mesoporous Carbon Catalysts. *ACS Catalysis* **2018,** *8* (4), 2844-2856.

14. Sun, Y.; Li, S.; Jovanov, Z. P.; Bernsmeier, D.; Wang, H.; Paul, B.; Wang, X.; Kühl, S.; Strasser, P. Structure, Activity, and Faradaic Efficiency of Nitrogen-Doped Porous Carbon Catalysts for Direct Electrochemical Hydrogen Peroxide Production. *ChemSusChem* **2018,** *11* (19), 3388-3395.

15. Fellinger, T.-P.; Hasché, F.; Strasser, P.; Antonietti, M. Mesoporous Nitrogen-Doped Carbon for the Electrocatalytic Synthesis of Hydrogen Peroxide. *Journal of the American Chemical Society* **2012,** *134* (9), 4072-4075.

16. Chen, S.; Chen, Z.; Siahrostami, S.; Higgins, D.; Nordlund, D.; Sokaras, D.; Kim, T. R.; Liu, Y.; Yan, X.; Nilsson, E.; Sinclair, R.; Nørskov, J. K.; Jaramillo, T. F.; Bao, Z. Designing Boron Nitride Islands in Carbon Materials for Efficient Electrochemical Synthesis of Hydrogen Peroxide. *Journal of the American Chemical Society* **2018,** *140* (25), 7851-7859.

17. Kim, H. W.; Ross, M. B.; Kornienko, N.; Zhang, L.; Guo, J.; Yang, P.; McCloskey, B. D. Efficient hydrogen peroxide generation using reduced graphene oxide-based oxygen reduction electrocatalysts. *Nature Catalysis* **2018,** *1* (4), 282-290.

18. Wang, A.; Bonakdarpour, A.; Wilkinson, D. P.; Gyenge, E. Novel organic redox catalyst for the electroreduction of oxygen to hydrogen peroxide. *Electrochimica Acta* **2012,** *66*, 222-229.

19. Valim, R. B.; Reis, R. M.; Castro, P. S.; Lima, A. S.; Rocha, R. S.; Bertotti, M.; Lanza, M. R. V. Electrogeneration of hydrogen peroxide in gas diffusion electrodes modified with tert-butyl-anthraquinone on carbon black support. *Carbon* **2013,** *61*, 236-244.

20. Zhang, G.; Wang, S.; Zhao, S.; Fu, L.; Chen, G.; Yang, F. Oxidative degradation of azo dye by hydrogen peroxide electrogenerated in situ on anthraquinonemonosulphonate/polypyrrole composite cathode with heterogeneous CuO/γ-Al_2O_3 catalyst. *Applied Catalysis B: Environmental* **2011,** *106* (3), 370-378.

21. Zhao, S.; Zhang, G.; Fu, L.; Liu, L.; Fang, X.; Yang, F. Enhanced Electrocatalytic Performance of Anthraquinonemonosulfonate-Doped Polypyrrole Composite: Electroanalysis for the Specific Roles of Anthraquinone Derivative and Polypyrrole Layer on Oxygen Reduction Reaction. *Electroanalysis* **2010,** *23* (2), 355-363.

22. Hodges, B. C.; Cates, E. L.; Kim, J.-H. Challenges and prospects of advanced oxidation water treatment processes using catalytic nanomaterials. *Nature Nanotechnology* **2018,** *13* (8), 642-650.

23. Sun, M.; Chu, C.; Geng, F.; Lu, X.; Qu, J.; Crittenden, J.; Elimelech, M.; Kim, J.-H. Reinventing fenton chemistry: iron oxychloride nanosheet for pH-insensitive H2O2 activation. *Environmental Science & Technology Letters* **2018**.

24. Zhang, S.; Hedtke, T.; Zhou, X.; Elimelech, M.; Kim, J.-H. Environmental Applications of Engineered Materials with Nanoconfinement. *ACS ES&T Engineering* **2021,** *1* (4), 706-724.

Chapter 2: Background

2.1 Industrial H_2O_2 generation: anthraquinone process

The industry-standard AQ-based H_2O_2 production process, often referred to as Riedl–Pfleiderer process, is schematically shown in Figure 1.[1] In the first hydrogenation step, 2-alkylanthraquinone (R-AQ) reacts with H_2 on a catalyst surface in organic solvent phase (e.g., trioctyl phosphate and trimethyl benzene). The temperature and hydrogen partial pressure are typically maintained at 40–50 ^oC and 4 bar. The palladium particles supported on Al_2O_3, SiO_2, and SiO_2/Al_2O_3 are known as the most efficient catalyst;[2] less expensive catalysts such as nickel have been explored, while problems such as rapid deactivation and low selectivity have been of serious concern. In the second auto-oxidation step, the hydrogenated anthraquinone (H_2AQ) is oxidized by oxygen (typically by air) back to AQ with concomitant production of H_2O_2. This spontaneous reaction occurs without catalysts at temperature around 30–60 ^oC under near atmospheric pressure. Hydrogen peroxide in the working solution commonly has a concentration between 0.8 and 1.9 % w/w, and efficient extractors can recover more than 95% of the H_2O_2 generated. Further purification by extraction and distillation produces H_2O_2 up to 70 wt % for industrial applications.[3]

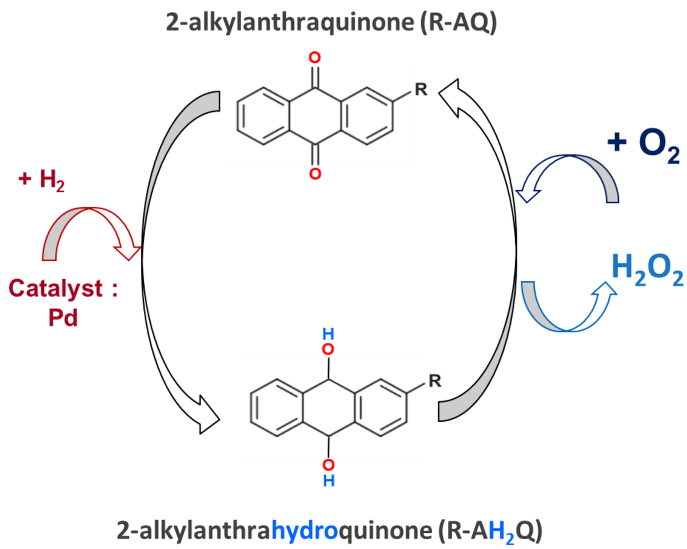

Figure 1. Industrial anthraquinone hydrogenation and anthrahydroquinone oxidation reactions for H_2O_2 production.

2.2 Transfer homogeneous chemistry to heterogeneous chemistry

The industrial process uses H_2 as the source of hydrogen, where a H_2 molecule splits over Pd surfaces into two surface adsorbed H*(ads) by a Langmuir–Hinshelwood mechanism. AQ in homogeneous solvent phase then reacts with surface H*(ads) to form H_2AQ, thus producing H_2O_2 selectively. Although the Pd catalysts can be recovered after each batch, industrial H_2O_2 process remains costly mainly because H_2 derives from steam reformation of methane, and separation of H_2O_2 from the organic solvent is via energy-intensive distillation.

Like industrial process, electrochemical peroxide production via AQ chemistry also contains two steps: 1) two electrons and two protons transfer to AQ to reduce AQ to hydrogenated anthraquinone (H_2AQ) (charge transfer); 2) H_2AQ reduces oxygen molecules to produce H_2O_2 and AQ (catalysis). However, AQ molecules are neither water-soluble nor electrically-conductive, so they cannot be directly utilized as electrodes operated in aqueous electrolyte. For electrons to flow to AQ's reactive sites, they need to be first to immobilized to a conductive substrate, so a reductive potential could be applied to the substrate and electrons could be driven to AQ molecules. After AQ are attached to heterogeneous conductive surfaces, simple filtration or electrode removal will allow easy separation and easy recovery, leaving the H_2O_2 concentrate as reactants for AOP or fuels. The H for AQ-R hydrogenation to H_2O_2 comes directly from H^+ in water, and the energy inputs can be directly from renewable electricity.

Previous works of anthraquinone utilized as heterogenous electrocatalysts[4-7] were suffering greatly from either low production and efficiency or high overpotential, possibly due to low AQ loading or unstable and H_2O_2-uncompatible conductive substrates. To design an efficient heterogeneous H_2O_2 generation electrocatalyst, the substrate-anthraquinone architecture with the following requirements: 1) substrate is conductive and will not decompose or adsorb H_2O_2 produced; 2) substrate contains plentiful functional groups/active sites for AQ immobilization; 3) charge transfer from substrate to AQ is one-directional and fast; 4) connection between substrate and AQ is strong and stable. Based on these criteria, several types of conductive substrates were proposed and discussed as the followings.

2.2.1 Carbon Nitride

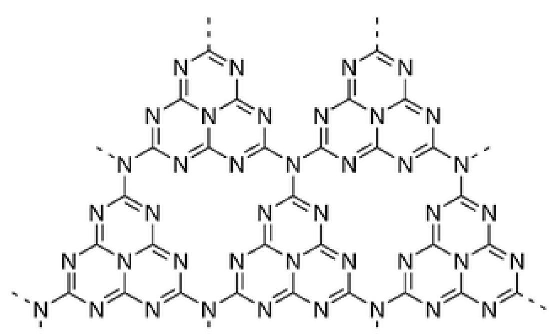

Figure 2. Chemical structure of C_3N_4.

Polymeric carbon nitride (C_3N_4) is a metal-free polymeric semiconductor that consists of mostly C and N and with a small amount of O as defects with its chemical structure shown in Figure 2. It can be readily synthesized by the facile, one-step, heat-induced polymerization of various precursors including cyanamide, dicyandiamide, and melamine at low cost.[8] Bulk as-synthesized C_3N_4 has a band gap of 2.6–2.7 eV, and is chemically stable in both acid and base.[9] C_3N_4 has a unique delocalized conjugated structure containing graphitic stacking of C_3N_4 layers, which are interconnected via tertiary amines and make it possesses high electronic conductivity.[10] With well-defined structure and available edge sites for functionalization, C_3N_4 functions as a good candidate for AQ augmentation.

Recent studies show that C_3N_4 has capability to photo-catalytically produce H_2O_2 via formation of 1,4-endoperoxide species on its surface,[11] and many modifications including non-metal atom incorporation[12-13] and hybridization with co-catalyst[14-15] have been reported with improved photocatalytic H_2O_2 generation and selectivity. Kim et al. recently developed anthraquinone-augmented polymeric carbon nitride for photocatalytic hydrogen peroxide production.[16] However, AQ molecules were only physically adsorbed to C_3N_4 through π-π interaction between basal planes and might be removed by intensive washing. Besides, both the stacking of as-synthesized bulk C_3N_4 layers and weak interaction between AQ and C_3N_4 will make this material unsuitable for electrocatalyst due to slow electron transfer, and very few terminal functional groups are exposed for further modification.

2.2.2 Polyaniline

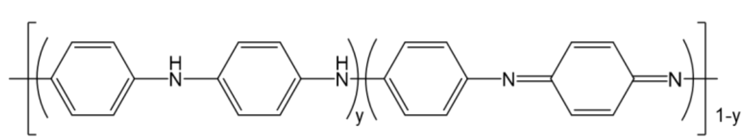

Figure 3. Chemical structure of polyaniline (emeraldine salt). Y is the average oxidation degree.

In addition to carbon nitride, another group of material that meets the criteria mentioned earlier is conductive polymer. Conductive polymers (CP) can be classified into several categories based on the mode of charge propagation, which is linked to the chemical structure of the polymer. Two main classes are electron-conducting and proton (ion)-conducting polymers; for conductive substrate, we are interested in electron-conducting polymers, which include redox polymers and electronically (intrinsically) conducting polymers (ECPs or ICPs).[17] As redox polymer's conductivity comes from oxidation/reduction of redox sites, this type of CP need to be avoided to eliminate competitive reactions in aqueous phase. Instead, we will mainly focus on exploring ICPs with available functional groups for AQ grafting, such as polyaniline (PANI).[18]

PANI's unique molecular structure and redox properties are responsible for its conductivity and catalytic activity. PANI is composed of monomer units of phenyl rings connected by a nitrogen heteroatom groups that can be either oxidized or reduced as shown in Figure 3. Depending on its degree of oxidation, PANI exhibits three distinct redox states with different conductivities, colors and electrochemical properties.[19-20] The redox states of PANI are: fully reduced leucoemeraldine (y = 0), fully oxidized pernigraniline (y = 1), and half-oxidized emeraldine base (y = 0.5). The only conductive form of PANI, emeraldine salt (green in color), is obtained by protonation of emeraldine base and yields the best performance as an electrocatalyst.[21] Polyaniline can be synthesized via many different pathways, including chemical (heterophane, interfacial, seeding, metathesis, self-assembling, and sonochemical polymerizations) , and electrochemical synthesis from aniline monomers.[22-23] Each synthesis method results in different PANI morphologies, conductivities, as well as electrochemical performance.[19] Polyaniline can function as potential candidates of AQ's conductive substrate as they are metal-free and contain abundant amine functional groups for AQ functionalization. Instead of only being attached to terminal edge sites, AQ molecules could be embedded in CP's main chains as pendant groups. As a result, both AQ's surface coverage density and H_2O_2 generation per unit mass of catalyst could be greatly increased.

2.3 Electrocatalysts for 2-electron oxygen reduction reaction

Over the past few years, much effort has been dedicated towards developing high-efficiency catalysts for the $2e^-$ ORR, spanning from pure metals, alloys, and nonmetal materials.[24-28] Unlike the 4-electron reduction pathway (Equation 1), which is intensively studied in fuel cells and metal-air batteries,[29-30] 2-electron reduction pathway (Equation 2) is thermodynamically less favored and thus requires fine tuning of material properties.

$O_2 + 4H^+ + 4e^- \rightarrow H_2O$ (1.23 V vs. RHE) (Equation 1)

$O_2 + 2H^+ + 2e^- \rightarrow H_2O_2$ (0.68 V vs. RHE) (Equation 2)

The key parameter determining the selectivity is the binding strength of *OOH, as either $4e^-$ or $2e^-$ ORR pathways share the same reactive intermediate,[26] where * means one reactive site on a catalytic surface:[27]

$O_2 + * + (H^+ + e^-) \rightarrow *OOH$ (Equation 3)

$*OOH + (H^+ + e^-) \rightarrow H_2O_2 + *$ (Equation 4, $2e^-$ pathway)

$*OOH + 3(H^+ + e^-) \rightarrow 2H_2O + *$ (Equation 5, $4e^-$ pathway)

Based on the volcano plot developed by Siahrostami et al., a catalytic surface of strong binding with *OOH will prefer $4e^-$ pathway, such as Pt and Pd; on the other hand, a catalytic surface of weak binding with *OOH will have high activity for both $4e^-$ and $2e^-$ pathways, while if the interaction is too weak, $2e^-$ selectivity will be increased while activity will be decreased. Therefore, a sophisticated design balancing activity and selectivity and regulating the adsorption and binding energy of reactive species will be of great importance for efficient H_2O_2 electrosynthesis.

Noble metals, such Ag-Hg and Pd-Hg alloys,[25, 31-32] have been reported to have both high activity and selectivity. Non-metal electrocatalyst, especially carbon-based materials have been of particular interest, since they are cheap, nontoxic, active, selective (FE >90%), and low cost. Carbon materials (carbon black, graphene, carbon nanotubes, porous carbons, etc.) mostly have intrinsic defect such as holes, edges, positive topological disclinations, and sp^3-C sites,[33] and these defect sites, along with oxygenated graphitic edge sites and oxygen-containing functional groups, can tailor the electrocatalytic properties and ORR activities.[34-36] In addition, carbon materials can be modified via heteroatom, such as nitrogen doping,[37-39] or single metal atom dopants.[40]

In water treatment applications, these electrocatalyst that achieve extraordinary performance in lab-scale, clean electrolyte with high ionic strength might face complications due to the other species existing in water matrices. Although noble metals and their relevant alloys are some of the most efficient catalysts for H_2O_2 production, they are limited by their cost and susceptibility to poisoning, particularly from species that are prevalent in a wastewater matrix (e.g., Cl^-)[41]. However, non-metal electrocatalysts are also susceptible to organic fouling and the oxygen functionalities can bind with divalent cations and resulting metal precipitation (*e.g.*, hydroxide and/or carbonate).

2.4 Electrode architecture

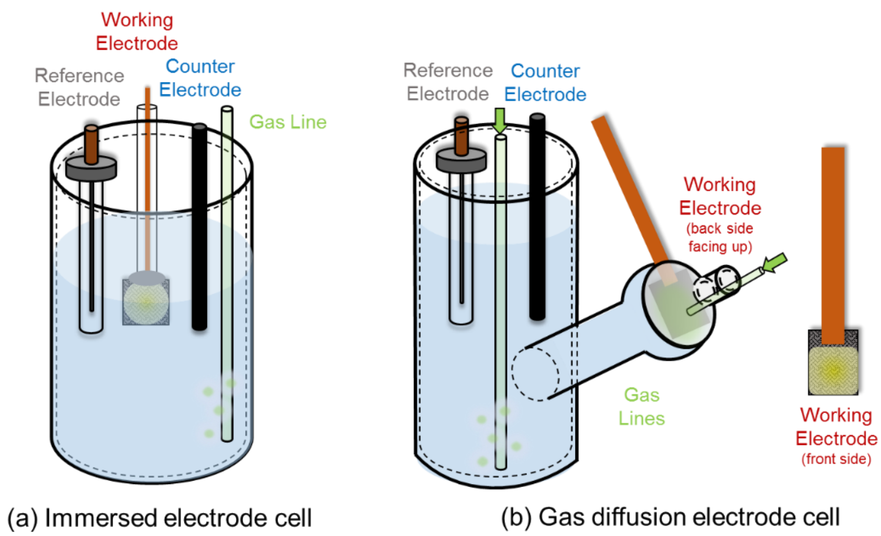

Figure 4. Electrode configurations.

In addition to electrocatalyst optimization, electrode architecture also plays an important role to maximize the electrochemical activity and selectivity. Traditionally, electrochemical experiments were performed in an immersed electrode (IM) cell (Figure 4a), where the whole electrode was immersed in electrolyte and gas were bubbled several centimeters away from the electrode surface and only in the bulk electrolyte. H_2O_2 generation from O_2 reduction reaction is a gas-consuming reaction (Equation 2), so it is critical that gas reactant could transfer to catalyst-electrolyte interface rapidly. However, due to O_2's low solubility in aqueous phase and its charge neutrality, oxygen mass transfer (OMT) is mainly via simple diffusion driven by concentration gradient, and thus it is well-reported that OMT is the limiting process determining ORR kinetics and performance in a traditional IM setup.[42-43]

On the contrary, gas diffusion electrode (GDE) provides an applicable solution to this deficiency (Figure 4b),[3, 44-45] where O_2 could be supplied directly to catalyst-electrolyte-gas triple-phase boundary region. Other than slowly diffusing in aqueous phase, O_2 will diffuse at a much faster rate in gas phase through the porous substrate to catalyst layer, where reactions happen. This additional gas diffusion pathway would maximize the catalytic activity of the material so we can directly observe the intrinsic properties of the catalyst.[46] By loading the electrocatalysts onto hydrophobic and porous electron conductor surface, gas transport process will be facilitated and a liquid/gas/solid interface will be created that favors the gas-involving reaction.

2.5 Electrochemical cell design

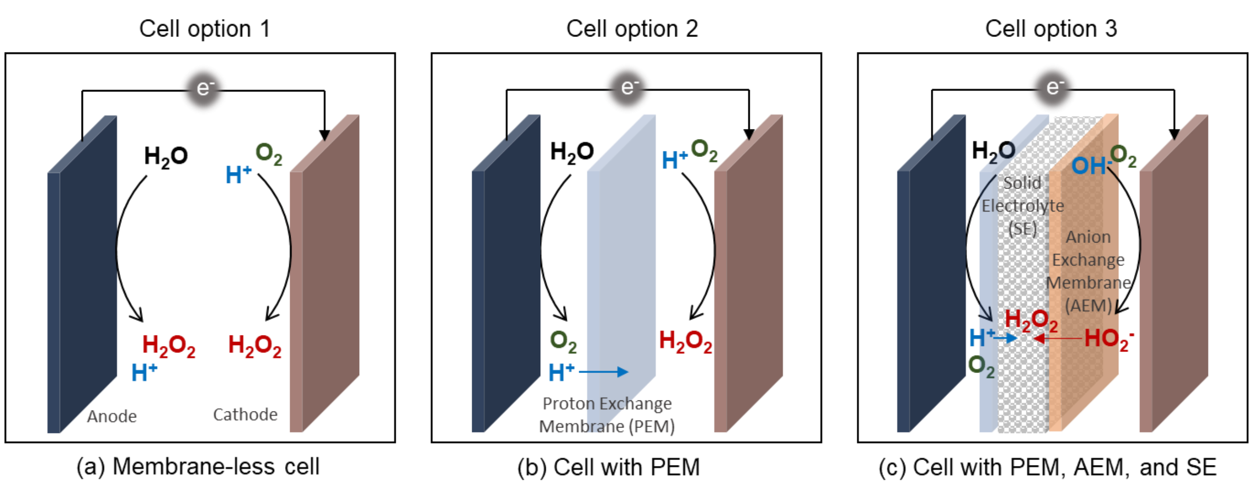

Figure 5. Cell configurations for H_2O_2 electrosynthesis.

Three distinct cell configurations are proposed in Figure 5 and they are commonly used by the researchers. Each option has unique pros and cons and therefore fits better to different process flow options and water compositions for treatment objectives. The first design (cell option 1, Figure 5a), a membrane-less cell, is a default design in many electrochemical water treatment processes, since it is easy to fabricate and maintain at low cost. The major drawback is the loss of performance due to the anode. Not only can the anode oxidize H_2O_2, but it can also lead to various parasitic reactions (such as chloride oxidation), depending on which constituents are present in the feed stream. This can be mitigated by designing an anode catalyst for the $2e^-$ water oxidation reaction to H_2O_2 ($2e^-$ WOR, Equation 6) to yield a maximal theoretical Faradaic efficiency (FE) of 200%. Nevertheless, designing $2e^-$ WOR catalysts has been very challenging due to competition with the more thermodynamically favorable $4e^-$ WOR (oxygen evolution, or OER, Equation 7).[24] With the advent of a suitable $2e^-$ WOR catalyst, contaminated water can be directly treated in the cell and this option may be appealing for water with sufficient ionic strength (*e.g.*, brackish water).

$$2H_2O \rightarrow H_2O_2 + 2(H^+ + e^-) \text{ (1.76 V vs. RHE)} \qquad \text{(Equation 6, } 2e^- \text{ WOR)}$$

$$2H_2O \rightarrow O_2 + 4(H^+ + e^-) \text{ (1.23 V vs. RHE)} \qquad \text{(Equation 7, } 4e^- \text{ WOR)}$$

Cell Option 2 (Figure 5b) may mitigate concerns such as chlorinated byproducts and H_2O_2 oxidation by separating the anodic and cathodic compartments using a proton exchange membrane (PEM). Here, the cathode is directly exposed to the feed waste stream where H_2O_2 is produced *in-situ*. The anode is recirculated with synthetic electrolyte (*i.e.*, a small fraction of treated water with addition of Na_2SO_4 or H_2SO_4)[47-49] that is not exposed to the waste stream. For this cell option where anode compartment is protected, it is possible that metal ions would precipitate on electrode surface (Mg^{2+} and Ca^{2+}) due to the local pH increase at the cathodic interface. Other species may be electroactive in the relevant reductive window of the system, such as copper ($Cu^{2+} + 2e^- \rightarrow Cu_{(s)}$, 0.34 V_{RHE}) and nitrate (which can form a variety of products). The targeted redox reactions potentials and likely side redox reaction potentials are plotted in Figure 6. The exact nature of how these species interact with the catalyst are unclear, but some mechanisms include irreversible poisoning (Cu chemisorption to the active site) or direct competition with O_2 to lower selectivity. Nevertheless, it is important to note that many of these species are reportedly present at relatively low concentrations in many industrial waste streams. In addition, cell option 2 is versatile, robust, and inexpensive, and can be applied in tandem with standard pretreatment measures for known problematic species (*e.g.*, water softening pretreatment). The research work in this thesis will be utilizing cell option 2 due to its simple structure and facile implementation to focus on the reduction reaction.

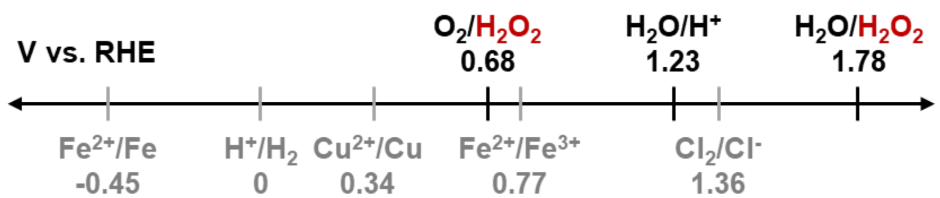

Figure 6. Redox reaction potentials for different cell options.Desired reactions and their potentials are marked above the scale, while undesired/side reactions and their potentials are marked below the scale.

Cell option 3 (Figure 5c), a fuel cell-like setup, employs a solid electrolyte (SE) for H_2O_2 production. Briefly, the 2e$^-$ ORR and hydrogen oxidation reactions (HOR) occur at the cathode and anode, respectively. The produced HO_2^- and H^+ traverse through the middle chamber housing the SE and combine to yield H_2O_2. Simultaneously, a small fraction of treated water flows through the SE to collect the H_2O_2, which is then mixed back with the intended waste stream. A highlight of this design is the fact that a highly conductive electrolyte is no longer needed; water with low ionic strength (*e.g.*, RO permeate) can be injected through the SE. The cell can be operated at lower overpotential for higher selectivity and H_2O_2 production efficiency. The large disadvantage is the stability of the materials needed, such as the membranes which are necessary to avoid flooding and the SE itself. Anion-exchange membranes (AEMs) pose several challenges, due to its slow HO_2^- transport velocity, low stability, and high local pH at the surface. The robustness and fouling potency of the SE must also be evaluated.

2.6 Advanced oxidation process

Advanced oxidation process (AOP) is recognized as an advanced water and wastewater treatment technique that is highly effective in delivering safe drinking water free of organics, inorganics, and microbes.[50] AOPs have been applied either as a pretreatment (*e.g.*, COD reduction) or as a polishing step (*e.g.*, after membrane filtration). Examples of industrial AOPs include treatment of organic-rich olive mill wastewater from the food and beverage industry,[51] dye-containing wastewaters in the textiles industry,[52-55] bleaching in pulp-and-paper industry,[56] water contaminated with biocides used in the agriculture industry,[57-59] and oily wastewater from the oil and gas industry.[60] AOPs have also been adopted for municipal water and wastewater treatment and recycling for removal of pathogens[61-62] and micropollutants,[63-64] as well as pretreatment for seawater desalination.[65]

AOP consists of several techniques for reactive oxygen species generation, including sonolysis (utilization of ultrasonic sound), ozonation (ozone as oxidant), UV photolysis, Fenton process, photocatalysis, and wet air oxidation.[66] AOP has many advantages: 1) it generally has fast reaction rates; 2) it can treat a wide range of organic and inorganic contaminants; 3) it can potentially reduce toxicity of contaminants by oxidizing them to more stable products; 4) it degrades contaminants in the same phase so does not require additional phase separation; 5) it does not produce materials that require further treatments such as "spent carbon" from activated carbon adsorption or sludge from biological processes.[67] However, it also has some disadvantages, including intensive capital investment, complex chemistry, and excess peroxide quenching in some applications.[67]

Typical AOPs require a continuous supply of precursor chemicals, such as H_2O_2, which is one of the most commonly used oxidants in AOP. H_2O_2 is usually first converted to hydroxyl radicals, which have high oxidation potential and can rapidly and non-selectively destroy nearly all electron-rich organic chemicals. OH radicals can be generated by Fenton reagent following Equation 8, or by UV irradiation following Equation 9.[68] Hydroxyl radicals can also be directly generated in some electro-Fenton processes.[53-55, 57-58]

$$H_2O_2 + Fe^{2+} \rightarrow OH^{\bullet} + OH^{-} + Fe^{3+} \quad \text{(Equation 8)}$$

$$H_2O_2 + UV \rightarrow OH^{\bullet} + OH^{\bullet} \quad \text{(Equation 9)}$$

2.7 References

1. Riedl, H.-J.; Pfleiderer, G. Production of hydrogen peroxide. US2158525, 1939.

2. Li, J.; Yao, H.; Wang, Y.; Luo, G. One-Step Preparation of Pd-SiO_2 Composite Microspheres by the Sol–Gel Process in a Microchannel. *Ind. Eng. Chem. Res.* **2014,** *53* (26), 10660–10666.

3. Campos-Martin, J. M.; Blanco-Brieva, G.; Fierro, J. L. G. Hydrogen Peroxide Synthesis: An Outlook beyond the Anthraquinone Process. *Angewandte Chemie International Edition* **2006,** *45* (42), 6962-6984.

4. Wang, A.; Bonakdarpour, A.; Wilkinson, D. P.; Gyenge, E. Novel organic redox catalyst for the electroreduction of oxygen to hydrogen peroxide. *Electrochimica Acta* **2012,** *66*, 222-229.

5. Valim, R. B.; Reis, R. M.; Castro, P. S.; Lima, A. S.; Rocha, R. S.; Bertotti, M.; Lanza, M. R. V. Electrogeneration of hydrogen peroxide in gas diffusion electrodes modified with tert-butyl-anthraquinone on carbon black support. *Carbon* **2013,** *61*, 236-244.

6. Zhang, G.; Wang, S.; Zhao, S.; Fu, L.; Chen, G.; Yang, F. Oxidative degradation of azo dye by hydrogen peroxide electrogenerated in situ on anthraquinonemonosulphonate/polypyrrole composite cathode with heterogeneous $CuO/\gamma\text{-}Al_2O_3$ catalyst. *Applied Catalysis B: Environmental* **2011,** *106* (3), 370-378.

7. Zhao, S.; Zhang, G.; Fu, L.; Liu, L.; Fang, X.; Yang, F. Enhanced Electrocatalytic Performance of Anthraquinonemonosulfonate-Doped Polypyrrole Composite: Electroanalysis for the Specific Roles of Anthraquinone Derivative and Polypyrrole Layer on Oxygen Reduction Reaction. *Electroanalysis* **2010,** *23* (2), 355-363.

8. Ismael, M. A review on graphitic carbon nitride (g-C3N4) based nanocomposites: Synthesis, categories, and their application in photocatalysis. *Journal of Alloys and Compounds* **2020,** *846*, 156446.

9. Kessler, F. K.; Zheng, Y.; Schwarz, D.; Merschjann, C.; Schnick, W.; Wang, X.; Bojdys, M. J. Functional carbon nitride materials — design strategies for electrochemical devices. *Nat. Rev. Mater.* **2017,** *2* (6).

10. Cao, S.; Yu, J. g-C3N4-Based Photocatalysts for Hydrogen Generation. *The Journal of Physical Chemistry Letters* **2014,** *5* (12), 2101-2107.

11. Shiraishi, Y.; Kanazawa, S.; Sugano, Y.; Tsukamoto, D.; Sakamoto, H.; Ichikawa, S.; Hirai, T. Highly Selective Production of Hydrogen Peroxide on Graphitic Carbon Nitride (g-C3N4) Photocatalyst Activated by Visible Light. *ACS Catalysis* **2014,** *4* (3), 774-780.

12. Wei, Z.; Liu, M.; Zhang, Z.; Yao, W.; Tan, H.; Zhu, Y. Efficient visible-light-driven selective oxygen reduction to hydrogen peroxide by oxygen-enriched graphitic carbon nitride polymers. *Energy & Environmental Science* **2018,** *11* (9), 2581-2589.

13. Moon, G.-h.; Fujitsuka, M.; Kim, S.; Majima, T.; Wang, X.; Choi, W. Eco-Friendly Photochemical Production of H2O2 through O2 Reduction over Carbon Nitride Frameworks Incorporated with Multiple Heteroelements. *ACS Catalysis* **2017,** *7* (4), 2886-2895.

14. Kofuji, Y.; Isobe, Y.; Shiraishi, Y.; Sakamoto, H.; Ichikawa, S.; Tanaka, S.; Hirai, T. Hydrogen Peroxide Production on a Carbon Nitride–Boron Nitride-Reduced Graphene Oxide Hybrid Photocatalyst under Visible Light. *ChemCatChem* **2018,** *10* (9), 2070-2077.

15. Zhao, S.; Guo, T.; Li, X.; Xu, T.; Yang, B.; Zhao, X. Carbon nanotubes covalent combined with graphitic carbon nitride for photocatalytic hydrogen peroxide production under visible light. *Applied Catalysis B: Environmental* **2018,** *224*, 725-732.

16. Kim, H. I., Choi, Y., Hu, S., Choi, W., & Kim, J. H. . Photocatalytic hydrogen peroxide production by anthraquinone-augmented polymeric carbon nitride. *Applied Catalysis B: Environmental* **2018,** *229*, 121-129.

17. Inzelt, G. Conducting polymers: past, present, future. *J. Electrochem. Sci. Eng.* **2018,** *8* (1), 3-37.

18. Zhan, C.; Yu, G.; Lu, Y.; Wang, L.; Wujcik, E.; Wei, S. Conductive polymer nanocomposites: a critical review of modern advanced devices. *Journal of Materials Chemistry C* **2017,** *5* (7), 1569-1585.

19. Boeva, Z. A.; Sergeyev, V. G. Polyaniline: Synthesis, properties, and application. *Polymer Science Series C* **2014,** *56* (1), 144-153.

20. Masters, J. G.; Sun, Y.; MacDiarmid, A. G.; Epstein, A. J. Polyaniline: Allowed oxidation states. *Synthetic Metals* **1991,** *41* (1), 715-718.

21. Silva, C. H. B.; Galiote, N. A.; Huguenin, F.; Teixeira-Neto, É.; Constantino, V. R. L.; Temperini, M. L. A. Spectroscopic, morphological and electrochromic characterization of layer-by-layer hybrid films of polyaniline and hexaniobate nanoscrolls. *Journal of Materials Chemistry* **2012,** *22* (28), 14052-14060.

22. Hatchett, D. W.; Josowicz, M.; Janata, J. Comparison of Chemically and Electrochemically Synthesized Polyaniline Films. *Journal of the Electrochemical Society* **1999,** *146* (12), 4535-4538.

23. Bhadra, S.; Khastgir, D.; Singha, N. K.; Lee, J. H. Progress in preparation, processing and applications of polyaniline. *Progress in Polymer Science* **2009,** *34* (8), 783-810.

24. Siahrostami, S.; Villegas, S. J.; Bagherzadeh Mostaghimi, A. H.; Back, S.; Farimani, A. B.; Wang, H.; Persson, K. A.; Montoya, J. A Review on Challenges and Successes in Atomic-Scale Design of Catalysts for Electrochemical Synthesis of Hydrogen Peroxide. *ACS Catalysis* **2020,** *10* (14), 7495-7511.

25. Jirkovský, J. S.; Panas, I.; Ahlberg, E.; Halasa, M.; Romani, S.; Schiffrin, D. J. Single Atom Hot-Spots at Au–Pd Nanoalloys for Electrocatalytic H2O2 Production. *Journal of the American Chemical Society* **2011,** *133* (48), 19432-19441.

26. Siahrostami, S.; Verdaguer-Casadevall, A.; Karamad, M.; Deiana, D.; Malacrida, P.; Wickman, B.; Escudero-Escribano, M.; Paoli, E. A.; Frydendal, R.; Hansen, T. W.; Chorkendorff, I.; Stephens, I. E. L.; Rossmeisl, J. Enabling direct H2O2 production through rational electrocatalyst design. *Nature Materials* **2013,** *12* (12), 1137-1143.

27. Jiang, K.; Zhao, J.; Wang, H. Catalyst Design for Electrochemical Oxygen Reduction toward Hydrogen Peroxide. *Advanced Functional Materials* **2020,** *30* (35), 2003321.

28. Wang, K.; Huang, J.; Chen, H.; Wang, Y.; Song, S. Recent advances in electrochemical 2e oxygen reduction reaction for on-site hydrogen peroxide production and beyond. *Chemical Communications* **2020,** *56* (81), 12109-12121.

29. Debe, M. K. Electrocatalyst approaches and challenges for automotive fuel cells. *Nature* **2012,** *486* (7401), 43-51.

30. Cheng, F.; Chen, J. Metal–air batteries: from oxygen reduction electrochemistry to cathode catalysts. *Chemical Society Reviews* **2012,** *41* (6), 2172-2192.

31. Verdaguer-Casadevall, A.; Deiana, D.; Karamad, M.; Siahrostami, S.; Malacrida, P.; Hansen, T. W.; Rossmeisl, J.; Chorkendorff, I.; Stephens, I. E. L. Trends in the Electrochemical Synthesis of H2O2: Enhancing Activity and Selectivity by Electrocatalytic Site Engineering. *Nano Letters* **2014,** *14* (3), 1603-1608.

32. Pizzutilo, E.; Kasian, O.; Choi, C. H.; Cherevko, S.; Hutchings, G. J.; Mayrhofer, K. J. J.; Freakley, S. J. Electrocatalytic synthesis of hydrogen peroxide on Au-Pd nanoparticles: From fundamentals to continuous production. *Chemical Physics Letters* **2017,** *683*, 436-442.

33. Jiang, Y.; Yang, L.; Sun, T.; Zhao, J.; Lyu, Z.; Zhuo, O.; Wang, X.; Wu, Q.; Ma, J.; Hu, Z. Significant Contribution of Intrinsic Carbon Defects to Oxygen Reduction Activity. *ACS Catalysis* **2015,** *5* (11), 6707-6712.

34. Hisatomi, T.; Kubota, J.; Domen, K. Recent advances in semiconductors for photocatalytic and photoelectrochemical water splitting. *Chemical Society Reviews* **2014,** *43* (22), 7520-7535.

35. Sa, Y. J.; Kim, J. H.; Joo, S. H. Active Edge-Site-Rich Carbon Nanocatalysts with Enhanced Electron Transfer for Efficient Electrochemical Hydrogen Peroxide Production. *Angewandte Chemie International Edition* **2019,** *58* (4), 1100-1105.

36. Lu, Z.; Chen, G.; Siahrostami, S.; Chen, Z.; Liu, K.; Xie, J.; Liao, L.; Wu, T.; Lin, D.; Liu, Y.; Jaramillo, T. F.; Nørskov, J. K.; Cui, Y. High-efficiency oxygen reduction to hydrogen peroxide catalysed by oxidized carbon materials. *Nature Catalysis* **2018,** *1* (2), 156-162.

37. Sun, Y.; Sinev, I.; Ju, W.; Bergmann, A.; Dresp, S.; Kühl, S.; Spöri, C.; Schmies, H.; Wang, H.; Bernsmeier, D.; Paul, B.; Schmack, R.; Kraehnert, R.; Roldan Cuenya, B.; Strasser, P. Efficient Electrochemical Hydrogen Peroxide Production from Molecular Oxygen on Nitrogen-Doped Mesoporous Carbon Catalysts. *ACS Catalysis* **2018,** *8* (4), 2844-2856.

38. Sun, Y.; Li, S.; Jovanov, Z. P.; Bernsmeier, D.; Wang, H.; Paul, B.; Wang, X.; Kühl, S.; Strasser, P. Structure, Activity, and Faradaic Efficiency of Nitrogen-Doped Porous Carbon Catalysts for Direct Electrochemical Hydrogen Peroxide Production. *ChemSusChem* **2018,** *11* (19), 3388-3395.

39. Han, L.; Sun, Y.; Li, S.; Cheng, C.; Halbig, C. E.; Feicht, P.; Hübner, J. L.; Strasser, P.; Eigler, S. In-Plane Carbon Lattice-Defect Regulating Electrochemical Oxygen Reduction to Hydrogen Peroxide Production over Nitrogen-Doped Graphene. *ACS Catalysis* **2019,** *9* (2), 1283-1288.

40. Jiang, K.; Back, S.; Akey, A. J.; Xia, C.; Hu, Y.; Liang, W.; Schaak, D.; Stavitski, E.; Nørskov, J. K.; Siahrostami, S.; Wang, H. Highly selective oxygen reduction to hydrogen peroxide on transition metal single atom coordination. *Nature Communications* **2019,** *10* (1), 3997.

41. Chaplin, B. P. The Prospect of Electrochemical Technologies Advancing Worldwide Water Treatment. *Accounts of Chemical Research* **2019,** *52* (3), 596-604.

42. Yin, F.; Liu, Y.; Wang, C.; Liu, H. Assessing the electron transfer and oxygen mass transfer of the oxygen reduction reaction using a new electrode kinetic equation. *Physical Chemistry Chemical Physics* **2018,** *20* (23), 16159-16166.

43. Bard, A. J.; Faulkner, L. R. *Electrochemical Methods: Fundamentals and Applications*. 2 ed.; Wiley Global Education: 2000.

44. Barazesh, J. M.; Hennebel, T.; Jasper, J. T.; Sedlak, D. L. Modular Advanced Oxidation Process Enabled by Cathodic Hydrogen Peroxide Production. *Environ Sci Technol* **2015,** *49* (12), 7391-7399.

45. Barros, W. R. P.; Ereno, T.; Tavares, A. C.; Lanza, M. R. V. In Situ Electrochemical Generation of Hydrogen Peroxide in Alkaline Aqueous Solution by using an Unmodified Gas Diffusion Electrode. *ChemElectroChem* **2015,** *2* (5), 714-719.

46. Xu, W.; Lu, Z.; Sun, X.; Jiang, L.; Duan, X. Superwetting Electrodes for Gas-Involving Electrocatalysis. *Accounts of Chemical Research* **2018,** *51* (7), 1590-1598.

47. Chen, Z.; Chen, S.; Siahrostami, S.; Chakthranont, P.; Hahn, C.; Nordlund, D.; Dimosthenis, S.; Nørskov, J. K.; Bao, Z.; Jaramillo, T. F. Development of a reactor with carbon catalysts for modular-scale, low-cost electrochemical generation of H2O2. *Reaction Chemistry & Engineering* **2017,** *2* (2), 239-245.

48. Xu, J.; Zheng, X.; Feng, Z.; Lu, Z.; Zhang, Z.; Huang, W.; Li, Y.; Vuckovic, D.; Li, Y.; Dai, S.; Chen, G.; Wang, K.; Wang, H.; Chen, J. K.; Mitch, W.; Cui, Y. Organic wastewater treatment by a single-atom catalyst and electrolytically produced H2O2. *Nature Sustainability* **2021,** *4* (3), 233-241.

49. An, J.; Li, N.; Wu, Y.; Wang, S.; Liao, C.; Zhao, Q.; Zhou, L.; Li, T.; Wang, X.; Feng, Y. Revealing Decay Mechanisms of H2O2-Based Electrochemical Advanced Oxidation Processes after Long-Term Operation for Phenol Degradation. *Environ Sci Technol* **2020,** *54* (17), 10916-10925.

50. Biń, A. K.; Sobera-Madej, S. Comparison of the Advanced Oxidation Processes (UV, UV/H2O2 and O3) for the Removal of Antibiotic Substances during Wastewater Treatment. *Ozone: Science & Engineering* **2012,** *34* (2), 136-139.

51. Ruzmanova, Y.; Ustundas, M.; Stoller, M.; Chianese, A. Photocatalytic treatment of olive mill wastewater by n-doped titanium dioxide nanoparticles under visible light. *Chemical Engineering Transactions* **2013,** *32*, 2233-2238.

52. Asghar, A.; Abdul Raman, A. A.; Wan Daud, W. M. A. Advanced oxidation processes for in-situ production of hydrogen peroxide/hydroxyl radical for textile wastewater treatment: a review. *Journal of Cleaner Production* **2015,** *87*, 826-838.

53. Özcan, A.; Oturan, M. A.; Oturan, N.; Şahin, Y. Removal of Acid Orange 7 from water by electrochemically generated Fenton's reagent. *Journal of Hazardous Materials* **2009,** *163* (2), 1213-1220.

54. Ruiz, E. J.; Arias, C.; Brillas, E.; Hernández-Ramírez, A.; Peralta-Hernández, J. M. Mineralization of Acid Yellow 36azo dye by electro-Fenton and solar photoelectro-Fenton processes with a boron-doped diamond anode. *Chemosphere* **2011,** *82* (4), 495-501.

55. Peralta-Hernández, J. M.; Meas-Vong, Y.; Rodríguez, F. J.; Chapman, T. W.; Maldonado, M. I.; Godínez, L. A. Comparison of hydrogen peroxide-based processes for treating dye-containing wastewater: Decolorization and destruction of Orange II azo dye in dilute solution. *Dyes and Pigments* **2008,** *76* (3), 656-662.

56. Hage, R.; Lienke, A. Applications of Transition-Metal Catalysts to Textile and Wood-Pulp Bleaching. *Angewandte Chemie International Edition* **2006,** *45* (2), 206-222.

57. Balci, B.; Oturan, N.; Cherrier, R.; Oturan, M. A. Degradation of atrazine in aqueous medium by electrocatalytically generated hydroxyl radicals. A kinetic and mechanistic study. *Water Research* **2009,** *43* (7), 1924-1934.

58. Oturan, N.; Trajkovska, S.; Oturan, M. A.; Couderchet, M.; Aaron, J.-J. Study of the toxicity of diuron and its metabolites formed in aqueous medium during application of the electrochemical advanced oxidation process "electro-Fenton". *Chemosphere* **2008,** *73* (9), 1550-1556.

59. Abdessalem, A. K.; Oturan, M. A.; Oturan, N.; Bellakhal, N.; Dachraoui, M. Treatment of an aqueous pesticides mixture solution by direct and indirect electrochemical advanced oxidation processes. *International Journal of Environmental Analytical Chemistry* **2010,** *90* (3-6), 468-477.

60. Nogueira, A. A.; Bassin, J. P.; Cerqueira, A. C.; Dezotti, M. Integration of biofiltration and advanced oxidation processes for tertiary treatment of an oil refinery wastewater aiming at water reuse. *Environmental Science and Pollution Research* **2016,** *23* (10), 9730-9741.

61. District., O. C. W. About GWRS: The world's largest advanced water pruification system for potable reuse.

62. United States Environmental Protection Agency. Emerging Technologies for Wastewater Treatment and In-Plant Wet Weather Management. **2013**.

63. Kanakaraju, D.; Glass, B. D.; Oelgemöller, M. Advanced oxidation process-mediated removal of pharmaceuticals from water: A review. *Journal of Environmental Management* **2018,** *219*, 189-207.

64. Azerrad, S. P.; Isaacs, M.; Dosoretz, C. G. Integrated treatment of reverse osmosis brines coupling electrocoagulation with advanced oxidation processes. *Chemical Engineering Journal* **2019,** *356*, 771-780.

65. Alshahri, A. H.; Fortunato, L.; Ghaffour, N.; Leiknes, T. Advanced coagulation using in-situ generated liquid ferrate, Fe (VI), for enhanced pretreatment in seawater RO desalination during algal blooms. *Science of The Total Environment* **2019,** *685*, 1193-1200.

66. Mishra N. S, R. R., Kuila A, Rani A, Mukherjee P, Nawaz A, Pichiah S. A Review on Advanced Oxidation Processes for Effective Water Treatment. *Curr World Environ* **2017,** *12* (3).

67. Sharma, S. R. J. P. P. M. L. A general review on Advanced Oxidation Processes for waste water treatment. In *International Conference On Current Trends In Technology*, Nuicone, 2011; Vol. 382 481, pp 08-10.

68. Moreira, F. C.; Boaventura, R. A. R.; Brillas, E.; Vilar, V. J. P. Electrochemical advanced oxidation processes: A review on their application to synthetic and real wastewaters. *Applied Catalysis B: Environmental* **2017,** *202*, 217-261.

Chapter 3: Research Objective

3.1 Research Objective

The overarching goal of the research is to <u>*develop the next-generation system using electrochemistry-based technology for water treatment applications*</u>. The fully-electrified, autonomous, and modular system will not require any chemical supply, and is composed of two major parts: an electrochemical cell that can synthesize H_2O_2 via the two-electron oxygen reduction reaction, and an electro-Fenton or catalytic-Fenton cell that can activate H_2O_2 for advanced oxidation process and can replace the less-energy-efficient UV processes. A conceptual figure illustrating the specific objectives of the research is shown in Figure 7.

The research seeks to systematically transfer anthraquinone's homogeneous chemistry to heterogeneous interfaces and utilize the selectivity for electrochemical hydrogen peroxide generation via oxygen reduction reaction. The catalyst will be made into gas diffusion electrode and incorporated into electrochemical hydrogen peroxide generation cell for continuous H_2O_2 production in advanced oxidation process. The H_2O_2 produced in-situ will be further activated to hydroxyl radicals for organic micropollutants degradation via electro-Fenton or catalytic-Fenton reactions.

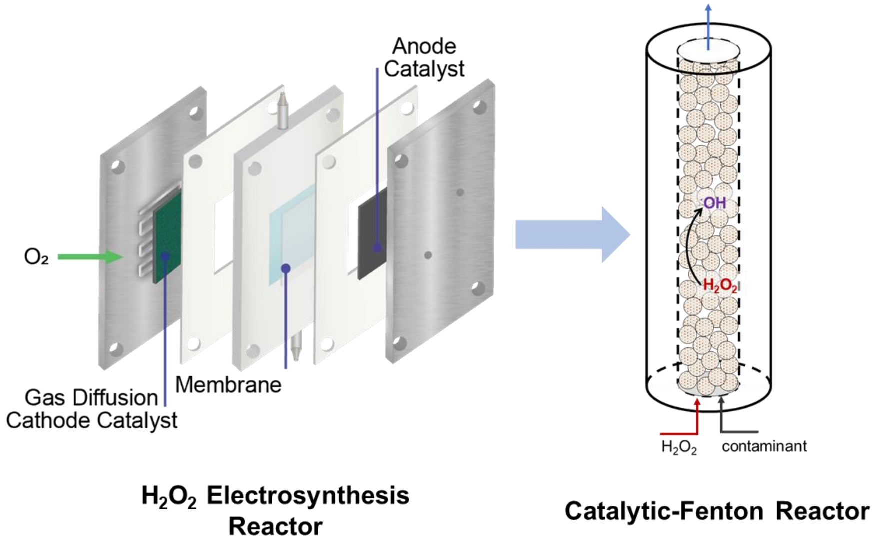

Figure 7. Schematic illustration of H_2O_2 generation cell incorporated with AOP treatment cell.

3.2 Research Hypothesis

The central hypothesis is that the anthraquinone chemistry can be driven electrochemically at a comparable rate to its homogeneous chemistry, and thus H_2O_2 could be produced efficiently by an electrochemical strategy. The generated H_2O_2 can then be activated in-situ in advanced oxidation process by iron oxychloride-based catalysts for a wide range of water treatment goals. In order to achieve the overarching goal and to fully verify the central postulation, the following hypotheses should be further verified:

Hypothesis 1. *Synthesized anthraquinone-modified electrocatalysts can utilize anthraquinone's high selectivity for efficient hydrogen peroxide production.* We hypothesize that we can convert AQ's homogeneous chemistry in organic phase to heterogenous interfaces in aqueous phase. AQ can perform both as a molecular mediator through the hydrogenation and as an efficient catalyst selecting two-electron H_2O_2-evolving reaction over four-electron O_2

redution-to-H_2O reaction. Though many non-metal electrocatalysts have been reported, most of their reactive sites are neither specified nor controlled. While in this electrocatalyst design, AQ is the most reactive functional site for two-electron oxygen reduction reaction, providing the opportunity to precisely control the reaction route and to limit competitive reactions. In-depth study needs to be performed on charge transfer from conductor to AQ redox levels, AQ mass loading, and catalytic activity and selectivity of electrocatalysts to establish fundamental understandings.

Hypothesis 2. *Anthraquinone derivatives can be attached to various conductive substrates for selective and efficient O_2 reduction to H_2O_2.* We can explore different conductive supports (polymeric carbon nitride, conductive polymers, etc.) and their capability to be linked to AQ and function as a stable and H_2O_2-friendly substrate, and use a suite of electrochemical characterizations to quantify and optimize electro-catalytic H_2O_2 production for their electrode assembly. Different porous conductive supports will be synthesized, and AQ will be covalently attached to the high surface area, gas-diffusing electrodes for high catalytic rates. With structural and AQ-density control, we are aiming to develop a series of AQ/substrate configurations for efficient and stable electrochemical hydrogen peroxide generation.

Hypothesis 3. *Gas diffusion electrode can improve the oxygen mass transfer to the electrode surface and thus enhance the electrocatalysis rate.* We will test the synthesized anthraquinone-based electrocatalysts in both immersed electrode setup, as well as gas diffusion electrode setup (and GDE-based flow cell) to compare their electrocatalytic activity, selectivity, and stability. Different gas compositions (pure nitrogen, pure oxygen, air, etc.) with different flow rates will be supplied to the system to systematically study the impacts of electrode architecture and the adaptability of the electrochemical system.

Hypothesis 4. *Iron oxychloride-based heterogenous packed bed catalysts and electrocatalysts can efficiently activate hydrogen peroxide to hydroxyl radicals for advanced oxidation process.* We will explore the possibilities of transferring the as-synthesized heterogeneous FeOCl catalysts to different catalytic reactors: packed bed reactor and electrochemical reactor. The H_2O_2 activation reaction (hydroxyl radical generation) kinetics, the model contaminant degradation capacity, as well as the system stability will be investigated and optimized for both systems to maximize the AOP activities. The energy and cost analysis will be performed to provide guidance of the better system for the purpose.

Chapter 4: Anthraquinone Modified Carbon Nitride

This Chapter is published (adapted):

Zhu, Q.; Pan, Z.; Hu, S.; Kim, J.-H. Cathodic Hydrogen Peroxide Electrosynthesis Using Anthraquinone Modified Carbon Nitride on Gas Diffusion Electrode. *ACS Applied Energy Materials* **2019**, *2* (11), 7972-7979.

Chu, C.; Zhu, Q.; Pan, Z.; Gupta, S.; Huang, D.; Du, Y.; Weon, S.; Wu, Y.; Muhich, C.; Stavitski, E.; Domen, K.; Kim, J.-H. Spatially separating redox centers on 2D carbon nitride with cobalt single atom for photocatalytic H_2O_2 production. *Proceedings of the National Academy of Sciences* **2020,** *117* (12), 6376.

4.1 Abstract

Electrochemical synthesis of hydrogen peroxide from oxygen and water can be a cost-effective and energy efficient alternative to the traditional approach which requires high energy input and expensive noble metal catalysts and has a large CO_2 footprint. The availability of selective electrocatalysts and performance validation of a device represent current research needs toward this goal. In this chapter, an efficient electrocatalytic system for hydrogen peroxide production is reported, which is based on anthraquinone molecular catalysts tethered onto carbon nitride (C_3N_4) conductive supports. Anthraquinone enables highly selective synthesis of hydrogen peroxide via two-electron oxygen reduction, and C_3N_4 support enables the precise control of destinations of the attached co-catalysts, as well as charge transfer of the composite

electrocatalysts. The optimal electrolyte pH was identified to both facilitate H_2O_2 electrochemical synthesis and minimize H_2O_2 decomposition. The optimal cathodic potential was identified to maximize oxygen reduction reaction rate while minimize other side reactions, especially hydrogen evolution reaction. The possibility of using anthraquinone as spatially-separated photocatalysts was explored.

4.2 Introduction

Hydrogen peroxide (H_2O_2) is an environmentally friendly and easy-to-handle oxidant. Since it generates only water and oxygen after its use, it is widely applied as an oxidant in chemical synthesis, a bleaching agent in pulp processing, or a precursor for advanced oxidation process in water and wastewater treatment.[1] It is increasingly been considered as an alternative liquid fuel and concentrated H_2O_2 has already been used as a propellent.[2-3] More recently, conversion of its chemical energy to electricity was demonstrated in a H_2O_2 fuel cell.[4-6] Global gross production is currently estimated at 3 million metric tons per year and has been steadily growing.[7]

The current industrial-scale H_2O_2 synthesis is mainly based on the anthraquinone (AQ) process (Figure 8a). Briefly, 2-alkylanthraquinone (R-AQ) reacts with hydrogen on a heterogeneous catalyst suspended in the organic solvent phase (hydrogenation step). The hydrogenated anthraquinone (H_2AQ) is subsequently oxidized by oxygen (typically by air) back to AQ with concomitant production of H_2O_2 (oxidation step).[7] This process requires expensive H_2 and noble metal catalysts, toxic organic solvents, and high energy input to maintain elevated temperature and separation of the produced H_2O_2 dissolved in solvents,[8-9] making H_2O_2 far from being carbon neutral and environmentally friendly within its life cycle. An alternative H_2O_2 synthesis method with both high energy efficiency and low environmental impact is highly desired, especially since it is one of the very few chemicals that are at the intersect of environmental and energy applications.

An electrochemical oxygen reduction reaction (ORR) by non-metal catalysts is considered a promising alternative to the industrial H_2O_2 synthesis process. Previously explored electrocatalytic materials include carbon,[10-13] modified graphite felt,[14-15] nitrogen-doped porous carbon,[16-18] boron nitride in carbon materials,[19] reduced graphene oxide,[20] etc. However, the catalytic sites of these materials mostly involve various nitrogen or oxygen-containing functional groups, sp^3-hybridized carbon, or defects of which electronic structures and energy levels are often poorly defined. It is therefore difficult to precisely control the structural motif or density of these active sites to selectively produce H_2O_2. Although some carbon-based materials show high Faradaic efficiencies (e.g., >90% in a rotating-disk setup) within short measurement timescale, the H_2O_2 accumulation in a cell or device construct has rarely been reported.

We here propose to exploit the exceptional selectivity of AQ chemistry for electrochemical H_2O_2 production by immobilizing AQ onto the well-defined heterogeneous surface of porous electrodes. Polymeric carbon nitride (C_3N_4), a stable n-type metal-free semiconductor, is employed as a support for AQ immobilization. C_3N_4 has been employed for photocatalytic H_2O_2 synthesis through oxygen reduction[21-22] and therefore proven for its inertness against H_2O_2 decomposition, but has not been used as electrode support. C_3N_4 is considered particularly instrumental in this application, since it provides abundant terminal amine (-NH and $-NH_2$) groups for covalent bonding with AQ derivatives; i.e., anthraquinone-2-

carboxylic acid (AQ-COOH). This AQ-modified C_3N_4 catalyst provides a model metal-free structure for tethering molecular catalysts onto the electrode. We present the performance of AQ-modified C_3N_4 in gas diffusion electrode form (Chapter 6) in electrolytes of varying pH values and overpotentials. We further discuss the H_2O_2 electrocatalytic selectivity and electron transfer process between C_3N_4 and AQ under device-relevant operational conditions. We also prove that the structure not only for an electrocatalytic system, but also for a photocatalytic system.

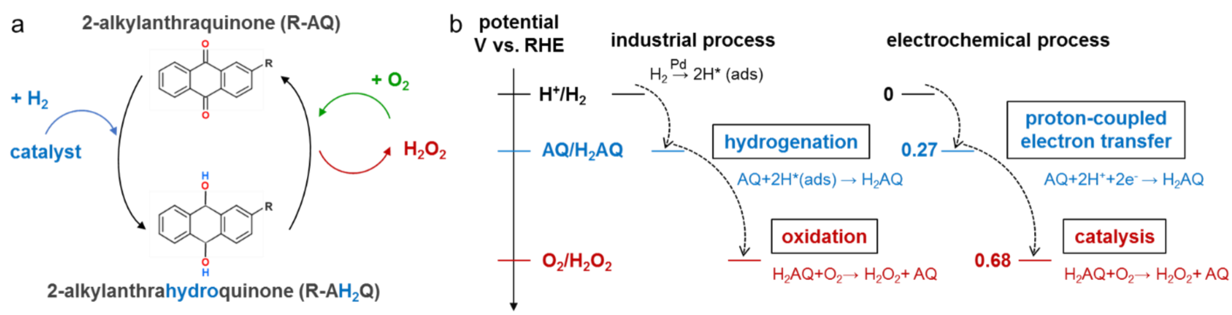

Figure 8. Schematic of anthraquinone process.(a) Schematic of the industrial, two-step anthraquinone (AQ) hydrogenation and anthrahydroquinone oxidation reactions for H_2O_2 production. (b) Energy level diagram and reaction schematics of the industrial two-step AQ process compared with the electrochemical pathway that utilizes the same AQ chemistry on the heterogeneous surfaces of AQ–C_3N_4 electrocatalysts.

4.3 Experimental Methods

4.3.1 C_3N_4 synthesis

Polymeric C_3N_4 was prepared by heating melamine in air at a ramp temperature rate of 5 °C min^{-1} to 550 °C and maintaining this temperature for 3 hours. After cooled to room temperature, the collected sample was ground with a mortar and pestle and washed with Milli-Q water (≥18.2 MΩ·cm, Millipore Water Purification System) for 5 times. The powder was dried at 80 °C in air for 15 hours and then suspended in water at a concentration of 10 mg mL^{-1} and probe sonicated for 8 hours in ice bath.[23] The suspension was then centrifuged at reactive centrifuge force (RCF) of 10640 for 15 minutes to collect these exfoliated C_3N_4 nanoparticles, which was dried at 80 °C in air for 15 hours before further AQ modification.

4.3.2 Anthraquinone modification

AQ-COOH was attached to the exfoliated C_3N_4 through either physical adsorption (termed AQ···C_3N_4) or chemical bonding (termed AQ–C_3N_4) (Figure S1). AQ···C_3N_4 was prepared by suspending 200 mg of exfoliated C_3N_4 and 60 mg of AQ-COOH in 20 mL dichloromethane (DCM) and stirring the suspension for 12 hours at 50 °C.[24] The suspension was then filtered and washed with 20 mL DCM for 10 times to remove the unbound AQ-COOH. To prepare AQ–C_3N_4, 400 mg exfoliated C_3N_4, 120 mg AQ-COOH, 114 mg *N*-(3-dimethylaminopropyl)-*N'*-ethylcarbodiimide hydrochloride, 80 mg 1-hydroxybenzotriazole hydrate, and 77 mg *N*,*N*-diisopropylethylamine were added to 50 mL DCM and stirred for 48 hours at room temperature.[25] The sample was filtered and washed with 50 mL DCM for 10 times to remove unreacted and unbound AQ-COOH and other chemicals. Both samples were dried at 80 °C in air for 15 hours.

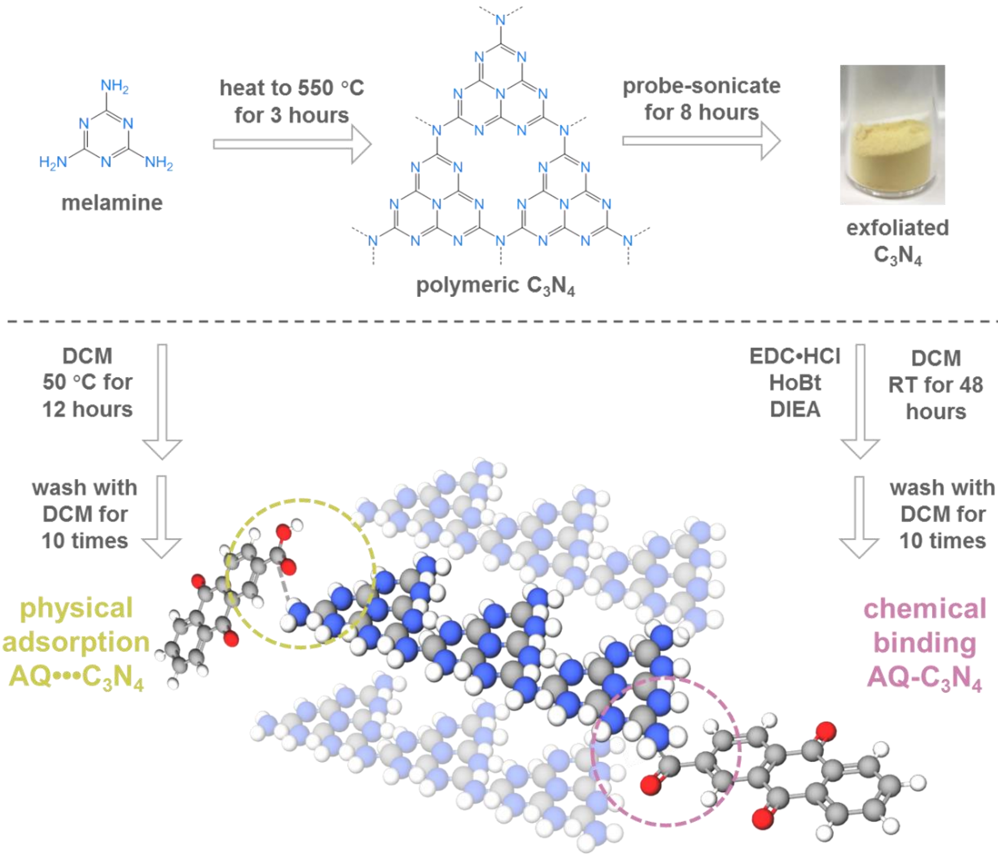

Figure 9. Schematic of material synthesis. Physical adsorption (AQ•••C_3N_4, left) and chemical binding (AQ–C_3N_4, right).

4.3.3 Synthesis of Co_1/AQ/C_3N_4

Bulk C_3N_4 was prepared following a thermal polymerization procedure by heating melamine powder in a ceramic crucible at a heating rate of 1 °C min^{-1} to 550 °C and annealing for 5 hours in a muffle furnace. As-prepared bulk C_3N_4 was grounded, exfoliated under probe-sonication for 8 hours, separated by centrifugation, washed with deionized water, and dried at 80 °C overnight. As-prepared ultrathin C_3N_4 (160 mg) was dispersed in 50 mL water under ultrasonication for 30 minutes, followed by addition of 1.5 mL $Co(NO_3)_2$ solution (2 g L^{-1}). The mixture was stirred and heated at 70 °C for 18 hours, separated by centrifugation, dried at 80 °C overnight, and annealed at 400 °C for 2 hours in a tube furnace under N_2 gas. The obtained powder was grounded, mixed with $NaPO_2 \cdot H_2O$ (twice the weight of obtained powder), and heated at 300 °C for 2 hours in a tube furnace under N_2 gas. As-prepared Co_1/C_3N_4 was washed with water and ethanol, and dried at 80 °C overnight. The Co loading amount was determined to be 0.13% (w/w) by inductively coupled plasma mass spectrometry (ICP-MS, PerkinElmer SCIEX Elan DRC-e) analysis after acid digestion. As-prepared Co_1/C_3N_4 (100 mg) was mixed with 10 mg anthraquinone-2-carboxylic acid, 7.7 mg diisopropylethylamine, 8.1 mg 1-hydroxybenzotriazole hydrate, and 11.5 mg *N*-(3-dimethylaminopropyl)-*N'*-ethylcarbodiimide hydrochloride. The mixture was dispersed in 50 mL dichloromethane under ultrasonication for 5 min and stirred for 48 hours. The $Co_1/AQ/C_3N_4$ product was separated by centrifugation, washed with dichloromethane and water, and dried at 80 °C overnight.

4.3.4 Material characterization

X-ray diffraction (XRD) patterns were obtained using a Rigaku SmartLab X-ray diffractometer equipped with a Cu-target X-ray tube (λ = 0.154nm) which was operated at 40 mA and 44 kV. Fourier transform infrared (FTIR) spectra were obtained with a Thermo Scientific Nicolet 6700 FTIR spectrometer equipped with an attenuated total reflectance (ATR) cell. X-ray photoelectron spectroscopy (XPS) measurements were performed with a PHI VersaProbe II Scanning XPS Microprobe which was equipped with a monochromated Al source. To minimize surface hydrocarbon contamination, all samples were dried in a vacuum oven at 80 °C for at least 3 days, and then immediately transferred to an ultrahigh vacuum chamber. Scanning electron microscopy (SEM) analysis was performed using a Hitachi SU8230 cold field-emission SEM microscope. HAADF-STEM images were taken using a Titan Themis Z STEM (ThermoFisher Scientific, USA) operated at 200 kV, coupled with a probe aberration-corrector to improve imaging spatial resolution to less than 1Å.

4.3.5 Electrochemical measurements

Two types of electrodes, immersed electrode (IE) and gas diffusion electrode (GDE) were tested in this chapter, and their differences will be discussed in more detail in Chapter 6. Electrochemical characterizations including cyclic voltammetry (CV) and chronoamperometry (CA) were performed using a Biologic SP-150 potentiostat/galvanostat. A carbon rod was used as the counter electrode. Either an Ag/AgCl reference electrode filled with saturated KCl solution (CHI111) or a calomel reference electrode (CHI150, both from CH Instruments) was used as the reference electrode. Unless specified, CV tests were performed at a scan rate of 20 mV s^{-1}. All electrochemical experiments were performed in 0.5 M phosphate buffer electrolytes of different pH values. The electrolyte pH was adjusted with phosphoric acid, sodium phosphate monobasic monohydrate, sodium phosphate dibasic, sodium phosphate, and sodium hydroxide (all from Sigma-Aldrich) to the desired values. To remove metal ion impurities (i.e., Fe^{2+}) in the buffer electrolytes, pre-electrolysis was performed before electrochemical characterizations: two carbon rods were set in a two-electrode system and a constant voltage of 3.5 V was applied for 12 hours. For the GDE setup, the electrolyte was first purged with N_2 or O_2 for 15 minutes. During select experiments, gas was constantly supplied to the electrode surface and the contacting electrolyte. For the IE setup, the electrolyte was purged with N_2 or O_2 for 15 minutes before tests and purged continuously throughout the experiment. Electrochemical impedance spectroscopy (EIS) was measured by a Biologic SP-150 potentiostat/galvanostat with a frequency range of 1 MHz to 1 Hz.

4.3.6 Hydrogen peroxide quantification

During electrolysis, a 50-μL sample aliquot was mixed with a 50-μL working solution (50 mM phosphate buffer at pH 7.4, 100 μM ampliflu red, and 0.05 U(unit)/mL horseradish peroxidase)[26] and the mixture was sit for 30 minutes to complete the reaction. For peroxidase, one unit is defined as the amount of enzyme that catalyzes the production of 1 mg purpurogallin in 20 seconds at 20°C and pH 6.0. H_2O_2 oxidizes ampliflu red to produce resorufin, which is catalyzed by horseradish peroxidase. The concentration of H_2O_2 was quantified by detecting the concentration of resorufin via an Agilent High-Performance Liquid Chromatography (HPLC) equipped with a C18 reverse phase column (80 Å, Agilent Technologies) and a photodiode array detector. The isocratic mobile phase consisting of 55% sodium citrate buffer (with 10% methanol, pH 7.4) and 45% methanol was eluted at a flow rate of 2 mL min^{-1}. To calibrate peak area to the H_2O_2 concentration, several H_2O_2 standard solutions were used with the area of each resorufin peak detected at 560 nm at retention time of 1.1 minutes. Faradaic efficiency (FE) was calculated by Equation 10, where V is volume of electrolyte (L), is H_2O_2 concentration in electrolyte (mol L^{-1}), n is the number of electrons transferred in oxygen reduction to hydrogen peroxide (n = 2), N_A is Avogadro's number, q is total charge passed (Coulomb), and the constant 6.24×10^{18} is the number of electrons in per Coulomb of charge (Coulomb^{-1}):[13]

$$\text{FE (\%)} = \frac{Experimentally\ produced\ H2O2}{Expected\ H2O2\ using\ 100\%\ charge\ passed} = \frac{VC_{H_2O_2}nN_A}{q\times 6.24\times 10^{18}} \times 100\% \qquad \text{(Equation 10)}$$

The same quantification method was used for all tests in other chapters as well.

4.3.7 Photocatalytic activity tests

Photocatalytic production of H_2O_2 was assessed by irradiation of photocatalyst suspension (12 mL, 0.5 g L^{-1}) using a Xenon lamp solar simulator (Model No. 10500; Abet Technologies, Inc.). The light intensity was adjusted to 100 mW/cm^2 (AM 1.5G; irradiation area = 1.77 cm^2). The suspension was purged with O_2 before (for 5 min) and during irradiation. At designated time points, small aliquots from suspensions were taken for analysis of H_2O_2 productions.

4.4 Results and Discussion

4.4.1 Material characterizations

Successful modification of C_3N_4 with AQ-COOH was first evidenced by XPS analysis (Figure 10). Pristine C_3N_4 (first row) exhibited a C-C peak (284.8 eV) from the adventitious carbon, a C=N-C peak (287.7 eV in carbon and 398.6 eV in nitrogen) from hybridized carbon with nitrogen, and a broad C=O peak (531.6 eV) from either the oxygen-containing functional groups introduced during exfoliation or from the oxygen contamination associated with adventitious carbon.[27-28] Comparatively, two distinctive features were noticed in AQ–C_3N_4 (third row in Figure 10): (1) the C-C peak was over 3 times more intense than that in C_3N_4 (both relative to C-N bond peaks, calculated in Figure 11) due to AQ's conjugated C-C bonds,[29] and (2) the oxygen atomic percentage (6.4 %) was markedly higher than that of C_3N_4 (3.4 %) due to the oxygen atoms in AQ. Both increases indicated AQ attachment at approximately 19 wt% (i.e., the average of 17.7 wt% based on carbon 1s core levels and 20.1 wt% based on oxygen 1s core levels). Similarly, AQ···C_3N_4 (second row in Figure 10) was estimated to contain about 4 wt% of

AQ (6.3 wt% based on carbon 1s core levels and 2.3 wt% based on oxygen 1s core levels). These observations suggested that chemical attachment afforded a much higher loading of AQ on C_3N_4 than physical adsorption.

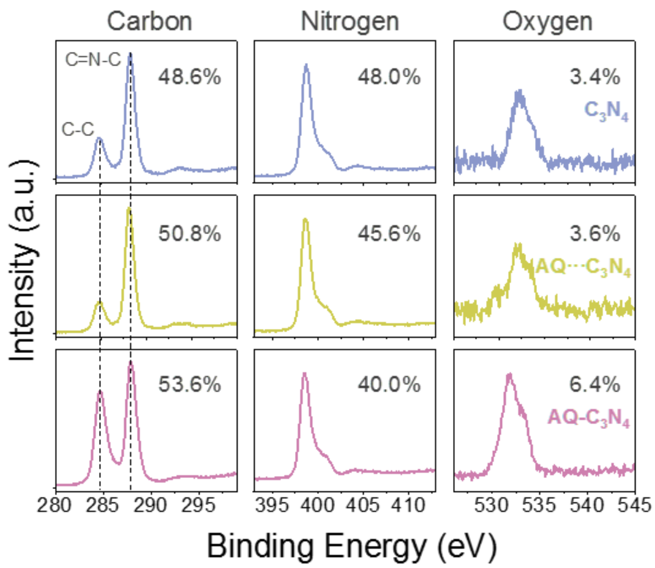

Figure 10. XPS of C_3N_4-based materials. Exfoliated C_3N_4 (blue), physically adsorbed AQ-COOH/C_3N_4 (termed AQ•••C_3N_4, green), and chemically functionalized AQ-COOH/C_3N_4 (AQ–C_3N_4, purple) samples showing their carbon 1s (first column), nitrogen 1s (second column), and oxygen 1s (third column) core levels. Numbers at the top right corner of each curve represent atomic percentage of the corresponding element in each material, calculated by integrating peak area. Peak intensities are normalized to the strongest peak.

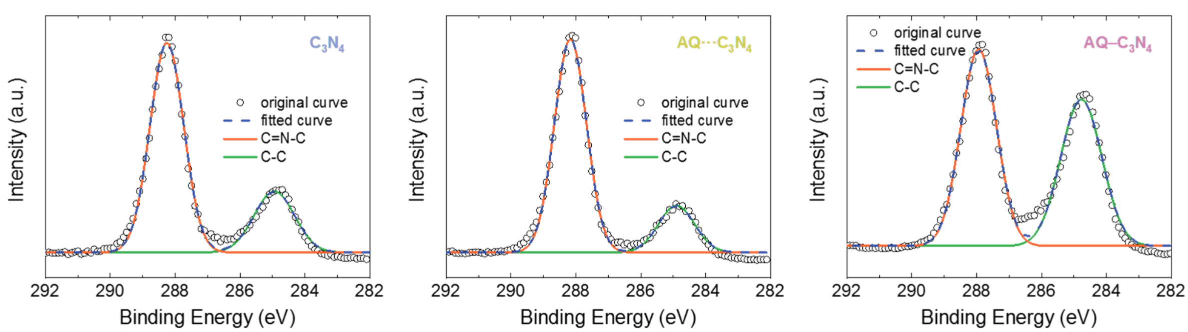

Figure 11. Deconvoluted C1s core-level spectra of C_3N_4-based materials. C1s core-level spectra of C_3N_4 (left), AQ•••C_3N_4 (middle), and AQ–C_3N_4 (right) were deconvoluted with two peaks: C-C at 284.8 eV and C=N-C at 287.7 eV. The integrated peak area ratios (C-C to C=N-C) are 0.28 (C_3N_4), 0.34 (AQ•••C_3N_4), and 0.91 (AQ–C_3N_4).

The FTIR spectra shown in Figure 2b further proved the successful covalent functionalization of AQ. Both AQ–C_3N_4 and AQ···C_3N_4 showed decreased transmittance at 1167 cm^{-1} (in-plane C-H bending), 1275 cm^{-1} (C-C stretching), and 1681 cm^{-1} (C=O stretching) (marked by grey dash lines), which corresponded to the characteristic peaks of AQ.[30-31] However, AQ–C_3N_4 showed a sharper peak at 1629 cm^{-1} compared with C_3N_4 and AQ···C_3N_4 as well as an additional peak at 1570 cm^{-1} (both marked by orange dotted lines). These two peaks could not be related to AQ molecules and were within IR range of amide bonds (1550-1640 cm^{-1}), which indicate that new peptide bonds were created in AQ–C_3N_4 from the reaction between the carboxylic acid groups from AQ–COOH and the amine groups from C_3N_4 edge sites.[32] Attachment of AQ onto C_3N_4, through either physical adsorption or chemical bonding, occurred only at the surface of C_3N_4 without disturbing the intrinsic crystalline structure of C_3N_4. As shown in Figure 2c, the (002) peaks at 27.4° remained the same before and after AQ modification. Theses peak indicate that interlayer stacking of C_3N_4 nanosheets[33] remained the same before and after AQ modification.

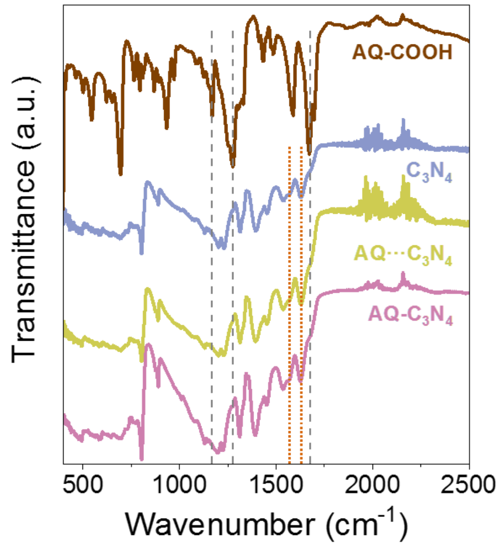

Figure 12. FTIR spectra of C_3N_4-based material. AQ-COOH (brown), exfoliated C_3N_4 (blue), AQ•••C_3N_4 (green), and AQ–C_3N_4 (purple).

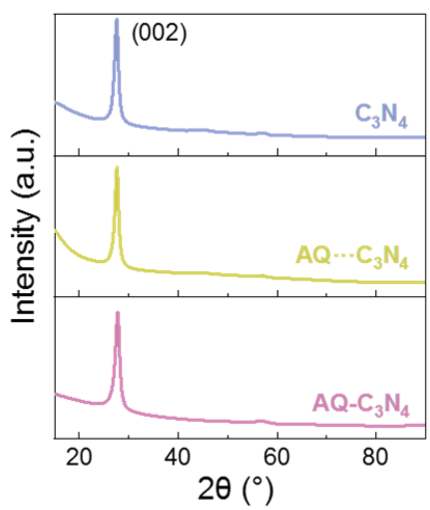

Figure 13. XRD spectra of C_3N_4-based material. Exfoliated C_3N_4 (blue), AQ•••C_3N_4 (green), and AQ–C_3N_4 (purple).

4.4.2 Electrochemical behavior of AQ modified C_3N_4

As-prepared catalysts, C_3N_4, AQ···C_3N_4, and AQ–C_3N_4, exhibited varying H_2O_2 generation rates when loaded onto conventional IEs. Under a potential bias, H_2O_2 is produced on the electrode surface through the following oxygen reduction reaction (ORR):[34]

$$O_2 + 2H^+ + 2e^- \rightarrow H_2O_2 \quad (0.68 \text{ V vs. RHE}) \qquad \text{(Equation 2)}$$

As shown in Figure 14(a), both AQ modified catalysts showed more positive ORR onset potentials at about 0.50 V vs. RHE than C_3N_4 at about 0.24 V vs. RHE. The increase in the current at lower reduction potential with AQ loading, for both AQ···C_3N_4 and AQ–C_3N_4, suggests the occurrence of two-step AQ-catalyzed electrochemical oxygen reduction reactions as follows:

$$AQ + 2\,H^+ + 2\,e^- \rightleftharpoons H_2AQ \quad (0.27 \text{ V vs. RHE}) \qquad \text{(Equation 11)}$$

$$O_2 + H_2AQ \rightarrow AQ + H_2O_2 \qquad \text{(Equation 12)}$$

This sequence of two-step reactions resembles the industrial H_2O_2 synthesis procedure (Figure 8). The first step is a reversible proton-coupled electron transfer; i.e., reduction of AQ by two electrons with two protons to form H_2AQ. The second step involves the reduction of oxygen to H_2O_2 and the oxidation of H_2AQ back to AQ.

The occurrence of AQ reduction (i.e., forward direction of Equation 11) was manifested in the CV of AQ–C_3N_4 by a strong reductive wave peaked at 0.27 V vs. RHE. The corresponding wave for H_2AQ oxidation back to AQ (i.e., reverse direction of Equation 11) was not observed. The absence indicates that H_2AQ reacted with oxygen preferentially at a sufficiently fast rate, and thus was not available for the reversible electrochemical oxidation. This process was further supported by the observation that, when the CV is performed with N_2 purging, both the reduction and oxidation peaks of AQ/H_2AQ redox pair emerged (Figure 14d). In the case of AQ···C_3N_4, similar electrochemical behavior was observed, but the AQ reduction peak was not explicit, most likely due to the small amount of AQ and inefficient charge transfer from C_3N_4 to AQ without covalent bonding.

As reduction potential was further reduced to < 0 V vs. RHE, the current continued to increase in the case of C_3N_4. This monotonic increase results not only from faster O_2 reduction but also from hydrogen evolution reaction (HER; $2H^+ + 2e^- \rightarrow H_2$) catalyzed by C_3N_4,[35-38] which competes with AQ reduction (Equation 11). At high reductive potentials, the four-electron oxygen reduction reaction (ORR; $O_2 + 4H^+ + 4e^- \rightarrow 2H_2O$) over the exfoliated C_3N_4 support or over-reduction of H_2O_2 to produce water is a potential side reaction.[39-40] Although the large density of defective carbon and nitrogen sites is known to catalyze these side reactions, the C_3N_4 crystallinity (Figure 13) and well-defined molecular AQ moiety make these side reactions unlikely,[41] because heterogeneous AQ-based electrocatalysts have proven their selectivity of $2e^-$ reduction H_2O_2 in many studies. [42-44] This trend of monotonic current increase did not change with AQ···C_3N_4 due to the aforementioned reason (i.e., minimal change in the structural and chemical properties of C_3N_4 by a small amount AQ loading). HER was found to be significantly suppressed when a large amount of AQ was chemically bound to C_3N_4 where most of HER active sites were covered on bare C_3N_4, because blocking of HER sites by AQ introduced a charge-tunneling distance between reactants and the original C_3N_4 catalytic sites. This observation also validated the selectivity of AQ–C_3N_4 in driving ORR over HER.

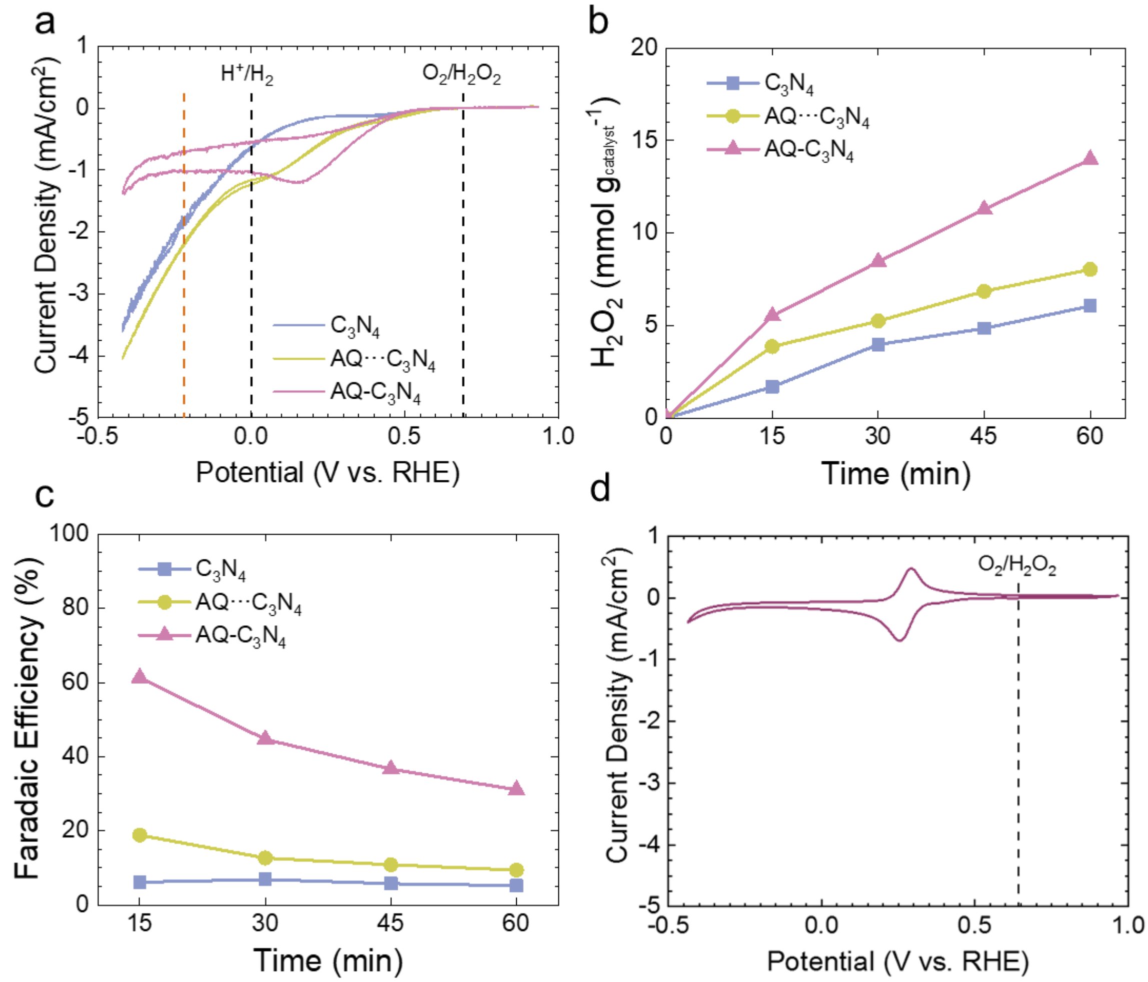

Figure 14. Electrochemical behavior of C_3N_4-based materials. (a) Cyclic voltammetry of C_3N_4 (blue), AQ•••C_3N_4 (green), and AQ–C_3N_4 (purple) IE electrodes in 0.5 M pH = 9 phosphate buffer purged with O_2. Vertical black dash lines represent the redox potentials of O_2/H_2O_2 (0.68 V vs. RHE) and H^+/H_2 (0 V vs. RHE) respectively; vertical orange dash line represents the 0.9 V overpotential for O_2 reduction to produce H_2O_2 (-0.22 V vs. RHE), which is the condition used in (b) and (c). (b) H_2O_2 generation, and (c) Faradaic efficiency for H_2O_2 generation of the three catalysts at -0.22 V vs. RHE. All the electrodes had the same area (1 cm^2) and the same catalyst loading (0.5 mg cm^{-2}). (d) Cyclic voltammetry of AQ–C_3N_4 IE electrodes in 0.5 M pH 9 phosphate buffer purged with N_2. Black dash lines represent redox potentials of O_2/H_2O_2 (0.68 V vs. RHE)

Both the amount of H_2O_2 produced (Figure 14b) and the Faradaic efficiency (Figure 14c) measured over time at a fixed potential of -0.22 V vs. RHE (corresponding to the orange dash line in Figure 14a) showed the same trend. The IE loaded with pristine C_3N_4 produced the smallest amount of H_2O_2 (6.1 mmol $g_{catalyst}^{-1}$) per hour, showing the lowest Faradaic efficiency of 5.2%. When AQ was physically adsorbed, both the H_2O_2 generation rate (8.0 mmol $g_{catalyst}^{-1}$) over a one-hour period and the FE (9.4%) increased but only by a small margin. AQ–C_3N_4 exhibited a much greater H_2O_2 generation rate in one hour (14.0 mmol $g_{catalyst}^{-1}$) and a higher FE (31.0%). Consistent with the above discussion, this improvement is likely to have resulted from the increased AQ coverage (4 wt% to 19 wt%). The electron transfer from C_3N_4 to AQ through covalent bonding AQ–C_3N_4 is also likely to be more efficient than through π-π stacking in AQ···C_3N_4 (Figure 15). Based on this observation, subsequent study was performed only using AQ–C_3N_4. It is noteworthy that the H_2O_2 generation curves for all three catalysts were not linear and the FE decreased over time. Decreasing generation rates under the constant electrochemical potential suggested that the O_2 reactants were depleted and became a limiting factor.

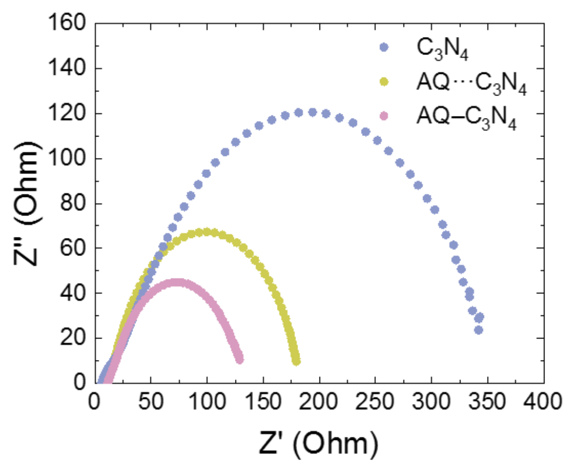

Figure 15. Electrochemical impedance spectroscopy of C_3N_4-based material. C_3N_4 (blue), AQ•••C_3N_4 (green), and AQ–C_3N_4 (purple) were tested at working condition (in 0.1M phosphate buffer of pH 9 with -0.22 V vs. RHE biased potential and purged with O_2).

4.4.3 pH-dependent hydrogen peroxide generation

When the electrolyte pH was increased from 1 to 9, the cathodic current density (Figure 16a), the H_2O_2 production rate (Figure 16b), and the Faradaic efficiency (Figure 16c) all increased monotonically. The formal potential for O_2/H_2O_2 redox couple increases by 59 mV per pH unit (at 25 °C) at a potential scale versus Ag/AgCl. The AQ/H_2AQ reduction potentials, which are the half-wave potentials ($E_{1/2}$) estimated by averaging the cathodic and anodic peak potentials, also increase by 59 mV per pH unit following the Nernstian law (Figure 17). Therefore, the potential difference between AQ/H_2AQ and O_2/H_2O_2 redox couples, i.e., the thermodynamic driving force of Equation 11, is pH independent. Figure 17a reports the current-potential relationship at the RHE scale because it is easier to compare performance (e.g., overpotentials) at different operational conditions (e.g., pH). Figure 17d replotted the same set of data at a potential scale versus Ag/AgCl. On one hand, electron transfer from C_3N_4 to AQ to form H_2AQ, i.e., the first step of AQ-catalyzed H_2O_2 production, followed the same current potential behavior at the Ag/AgCl scale, showing no dependence on local pH. On the other hand, the second step of AQ-catalyzed H_2O_2 production, i.e., Equation 11, exhibits a constant driving force. Two factors may have resulted the observed pH dependence: (1) the property of C_3N_4 supports controls the pH-independent electron-transfer rates to AQ/H_2AQ redox couples (Reaction 3); and (2) O_2 reduction by H_2AQ (Equation 11) may be a rate limiting step for the overall rate of H_2O_2 production.[45-46]

Electrochemical performance at pH > 9 deviated from this trend. While H_2O_2 generation rates remained comparable (i.e., 60.1, 61.0, and 60.9 mmol $g_{catalyst}^{-1}$ h^{-1} at pH, 9, 10, and 11, respectively), the Faradaic efficiency decreased from 39.8% at pH 9 to 35.2% at pH 10 and 32.5% at pH 11. This decrease is likely due to the deprotonation of H_2O_2 and decomposition of

HO_2^- (hydroperoxyl anion) (decomposition rates shown in Figure 18) through the following disproportionation reaction (Equation 13):[47-50]

$$HO_2^- + H_2O_2 \rightarrow H_2O + O_2\,(g) + HO^- \qquad \text{(Equation 13)}$$

Since proton is consumed at the electrode surface (Equation 2), local pH at the mass transfer boundary layer of GDEs is likely to be higher than in the bulk electrolyte.[51] This leads to H_2O_2 deprotonation and decrease in Faradaic efficiency at pH > 9 (i.e., measured at bulk) as the p*K*a of H_2O_2 is 11.6. Since H_2O_2 self-decomposition was shown negligible in electrolytes of pH < 9 in the electrochemical cell, other cell components including electrode materials, catalysts, the counter electrode, etc., should not cause H_2O_2 decomposition.

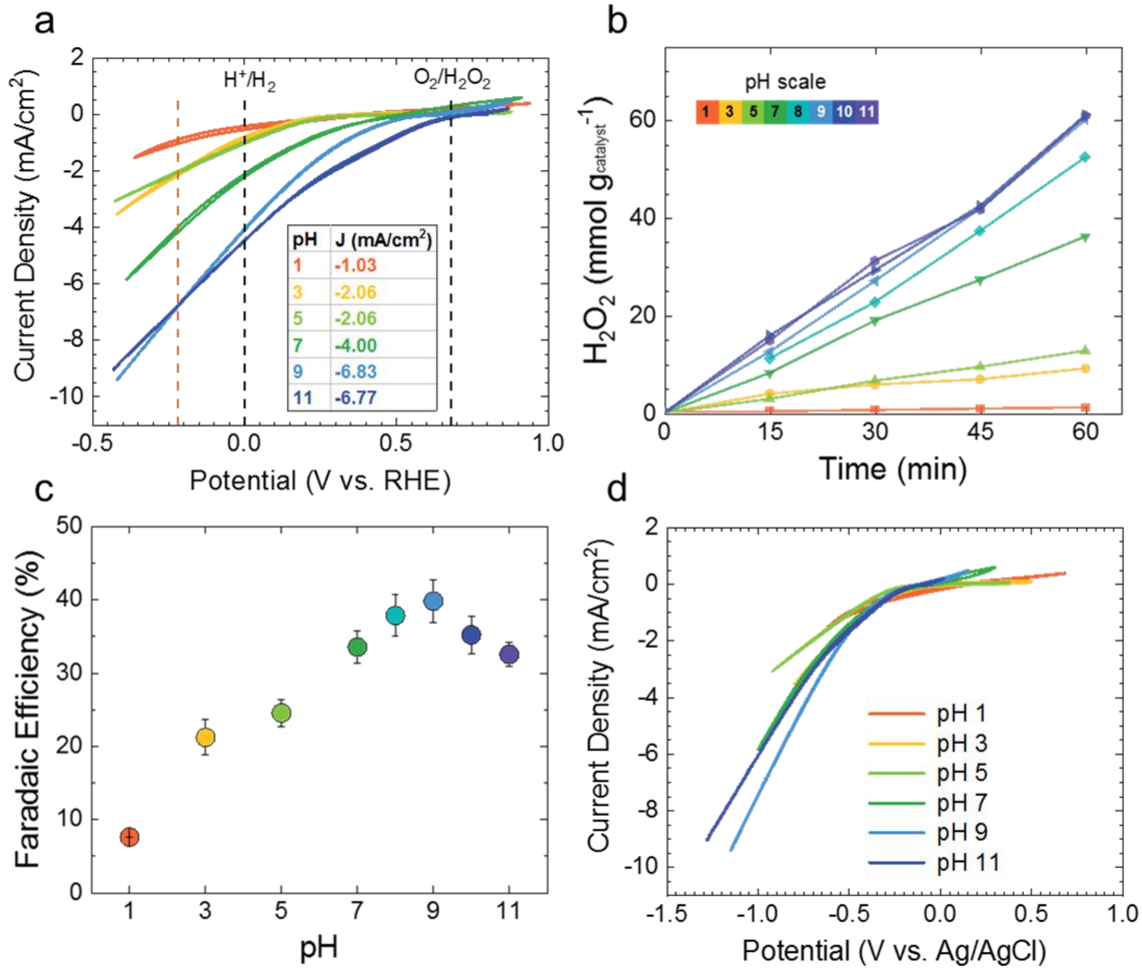

Figure 16. pH-dependent electrochemical behavior of AQ-C_3N_4. (a) Cyclic voltammetry of AQ–C_3N_4 in O_2-purged 0.5 M phosphate buffers of pH 1 to 11. Black dash lines represent redox potentials of O_2/H_2O_2 (0.68 V vs. RHE) and H^+/H_2 (0 V vs. RHE) respectively; orange dash line represents 0.9 V overpotential for O_2/H_2O_2 (-0.22 V vs. RHE). The inserted table shows current densities in different pH values at the applied potential of 0.68 V vs. RHE. (b) H_2O_2 generation with AQ–C_3N_4 on GDE in O_2-purged 0.5 M phosphate buffer at pH 1, 3, 5, 7, 8, 9, 10, and 11. (c) Faradaic efficiency for H_2O_2 generation at different pH values. (d) Replotted Figure 6(a) at a potential scale vs. Ag/AgCl.

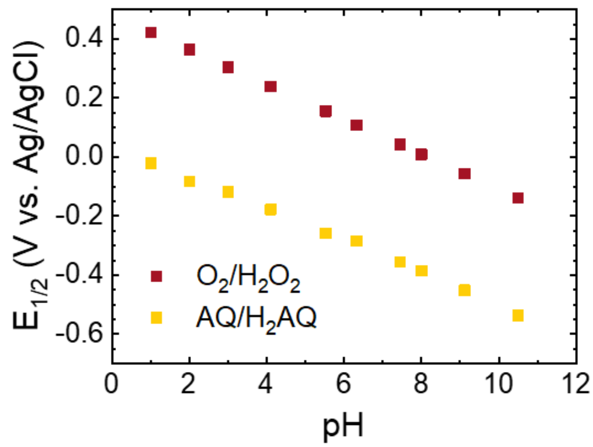

Figure 17. pH-dependent energy levels of AQ/H_2AQ and O_2/H_2O_2 redox couples. AQ/H_2AQ half-wave potential ($E_{1/2}$) was estimated by averaging the cathodic and anodic peak potentials as tested in AQ–C_3N_4 IE. O_2/H_2O_2 was calculated following the Nernstian Equation, where $E^0_{O2/H2O2}$ = 0.68 V vs. RHE and $E_{O2/H2O2}$ increases by 0.059 V per pH decade.

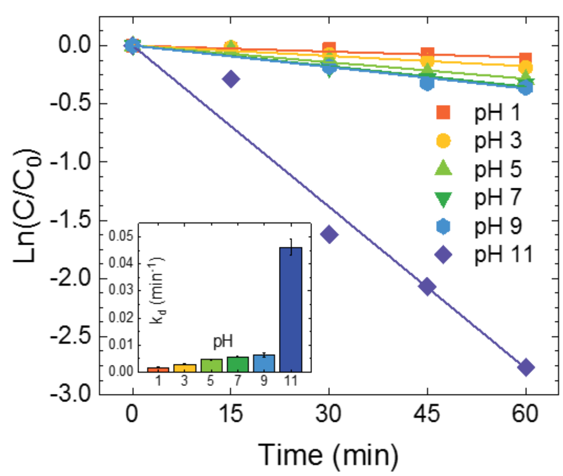

Figure 18. H_2O_2 decomposition rate with AQ–C_3N_4. Catalysts were tested with GDE in 0.5 M phosphate buffer of pH 1 to 11 added with 2 mM H_2O_2 at -0.22 V vs. RHE; the insert shows calculated decomposition rate constant.

4.4.4 Overpotential-dependent hydrogen peroxide generation

The electrochemical H_2O_2 generation rate by AQ–C_3N_4 GDE peaked at the overpotential of 0.9 V (-0.22 V vs. RHE, the potential used in H_2O_2 electrolysis) (Figure 19). Compared to other reported non-metal electrocatalysts (Table 1), the H_2O_2 electro-synthetic cell setup is likely the most promising for long-term H_2O_2 accumulation for two reasons: (1) the C_3N_4-based porous support has the potential to achieve higher surface area and electrical conductivity; and (2) as shown in Figure 18, decomposition rates of H_2O_2 on the C_3N_4-based porous support is as low as 0.0064 min^{-1} at pH = 9, necessary for the molar concentration level of H_2O_2 produced.

Compared to other reported non-metal electrocatalysts (Table 1), it appears that AQ–C_3N_4 needs to be operated at a relatively high overpotential, mostly due to conductivity loss from C_3N_4 supports and the overpotential loss associated with the second step of selective H_2O_2 catalysis (Equation 11).[51] More conductive support should reduce the conductivity loss, which will be further discussed in Chapter 5. The pH-independent intrinsic overpotential of the AQ/H_2AQ redox couple relative to O_2/H_2O_2 is 0.39 V, which provides the driving force for selective H_2O_2 production but is fixed and non-negligible in this catalytic system. When the applied overpotential is above 0.9 V, both H_2O_2 generation and Faradaic efficiency decreased dramatically, because the potential applied is close to the onset potential for H_2 evolution on C_3N_4 (-0.25 to -0.45 V vs. RHE),[35-37] and an increasing portion of electrochemical currents would contribute to undesired H_2 evolution reactions. Therefore, a more porous and conductive C_3N_4 support is expected to achieve comparable H_2O_2-catalytic currents at lower potentials, thus improving the FE for H_2O_2 production.

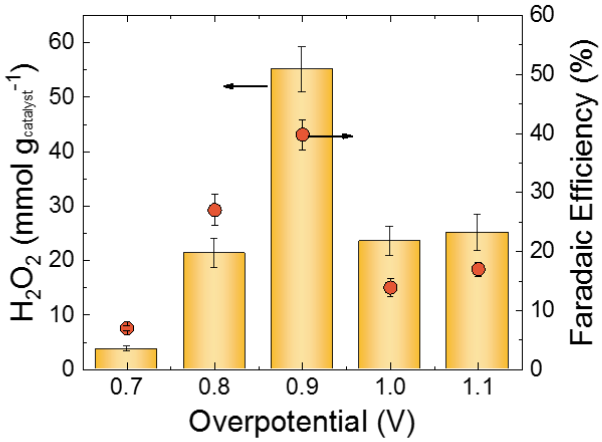

Figure 19. Overpotential-dependent hydrogen peroxide generation of AQ-C_3N_4. Figure 7. H_2O_2 generation (left y-axis) and Faradaic efficiency (right y-axis) with AQ–C_3N_4 on GDE in O_2-purged 0.5 M pH 9 phosphate buffer at different overpotentials after one hour of electrolysis.

Table 1. Comparison of non-metal electrocatalysts

Catalyst/Electrode	[H_2O_2] (mmol $g_{catalyst}^{-1}$ h^{-1})	Efficiency (%)	Experimental condition			Active sites	Ref
			Gas	Electrolyte	Potential (V vs. RHE)		
hierarchically porous carbon from MOF carbonization	395.70	81.8	O_2	0.05 M H_2SO_4 + Na_2SO_4 (pH 1)	-0.2	sp^3-C bonds and defects	11
carbon nanotube	158.76	31.0	O_2	0.01 M Na_2SO_4 (pH 6)	0.0	-	12
graphene/carbon black (GDE)	0.04	-	O_2	0.5 M Na_2SO4 (pH 6.5)	0.3	carbon black	52
mesoporous N-doped carbon	547.07		O_2	0.1 M K_2SO_4 (pH 7)	0.2	-	16
mesoporous N-doped carbon (pyrolysis of carbon and polyethyleneimine)	570.10	65.0	O_2	0.1 M K_2SO_4 (pH 7)	0.2	graphitic-N	17
mesoporous N-doped carbon (ionic liquid -derived)	120.62	65.2	O_2	0.1 M $HClO_4$ (pH 1)	0.1	quaternary nitrogen; conjugated π system	18

riboflavinyl-anthraquinone carboxylate ester/carbon black	8.40	70.0	O_2	0.5 M H_2SO_4 (pH 0.3)	0.1	riboflavin	[53]
tert-butyl-anthraquinone/carbon black (MGDE)	294.98	26.3	O_2	0.1 M H_2SO_4 + K_2SO_4 (pH 0.7)	-0.7	*tert*-butyl-anthraquinone	[54]
AQ–C_3N_4	60.08	42.2	O_2	0.5 M phosphate buffer (pH = 9)	-0.2	anthraquinone	this work
oxidized carbon nanotube	2.90*	~90	O_2	1M KOH (pH 14)	0.4	oxygen functional groups	[13]
Anthraquinonemono-sulphonate /polypyrrole modified graphite	0.22*	70.0	O_2	0.5 M H_2SO_4 + 0.3 M NaH_2PO_4 (pH 4.3)	0.1	-	[55]
modified graphite felt	0.34*	80.8	O_2	0.05 M Na_2SO_4 (pH 7)	0.0	N/O-containing groups	[14]
activated graphite felt	0.42*	68.0	O_2	0.05 M H_2SO_4 + Na_2SO_4 (pH 1)	-0.4	sp^3-C bonds, defects; O-containing groups	[15]

4.5 AQ modified C_3N_4 as photocatalyst

Based on the successful attachment of anthraquinone molecules onto the edge sites of carbon nitride substrate as an electrocatalyst for oxygen reduction reaction, we later explored the possibility of turning AQ–C_3N_4 into a photocatalyst with oxidation centers spatially separated from the reduction centers. We are interested in developing efficient photocatalysts because harvesting solar photon energy to drive redox reactions involving water and oxygen is the most espoused strategy for the green synthesis of alternative fuels such as H_2 and H_2O_2.[56-59] Yet, solar-to-energy conversion efficiencies achieved using current semiconductor photocatalysts remain relatively low,[60-61] due to the inherent limitations in material properties such as prevalent charge recombination in low bandgap materials and the insufficient selectivity toward fuel synthesis reaction.[62] One promising material engineering strategy is to decorate the semiconductor surface with co-catalysts,[56, 63] ideally both reductive and oxidative co-catalysts within a single photocatalytic material. Nevertheless, randomly loading two co-catalysts often results in direct contact between oxidation and reduction centers, worsening charge recombination that is detrimental to photosynthetic reactions.[64]

Placing two co-catalysts without direct contact requires sophisticated material architecture and synthesis strategy. One co-catalyst, typically oxidative, can be loaded on a substrate in trace amounts to minimize such contact but only at the expense of the available catalytic sites and thus the overall efficiency.[65-66] A more promising strategy is to design the substrate photocatalysts to provide physically separated sites for co-catalyst hosting. The existing strategies to prepare spatially-separated co-catalysts, however, exclusively rely on the three-dimensional nature of the substrate structure and cannot be readily extended to 2D materials such as graphitic carbon nitride (C_3N_4). C_3N_4 has often been used as the semiconductor material of choice for the photocatalytic synthesis of H_2O_2,[58, 67-68] an emerging substitute for compressed H_2 due to recent advances in H_2O_2 fuel cell technology.[69] C_3N_4 exhibits valence band (VB) and conduction band (CB) potentials that span those of H_2O/O_2 and O_2/H_2O_2 redox pairs and is capable of harnessing broad spectrum of sunlight due to its low bandgap energy. However, solar-to-fuel conversion efficiencies remain, in general, relatively low due to limitations that are commonly found in other materials: (i) ineffective hole scavenging via water oxidation and the resulting charge recombination,[58, 67] which often necessitates the addition of organic electron donors,[21, 70-71] and (ii) low selectivity towards H_2O_2 synthesis via two-electron reduction of O_2 as compared to four-electron reduction of O_2 or H_2 evolution.[58, 67]

Based on the experience we learned from developing AQ–C_3N_4 electrocatalyst as elaborated previously, we introduce an innovative strategy to load two co-catalysts onto 2D C_3N_4, with controlled physical separation in atomistic scale (Figure 20). Here cobalt and anthraquinone (AQ) were used as co-catalysts that are crucial for efficient photocatalytic synthesis of H_2O_2. Co is loaded into the void center of the C_3N_4 plane as a single atom (Co_1) and serves to facilitate the water oxidation.[72-76] At the same time, AQ is loaded onto the amine anchors that are present only on the edge of C_3N_4, ensuring that it is not in direct contact with the Co catalyst. The AQ enhances the selectivity of O_2 reduction to H_2O_2, following the mechanism widely exploited in current industrial H_2O_2 production process.[77] The new composite catalyst, $Co_1/AQ/C_3N_4$ is demonstrated to photocatalytically produce H_2O_2 at high efficiency under simulated solar irradiation without supply of a sacrificial agent.

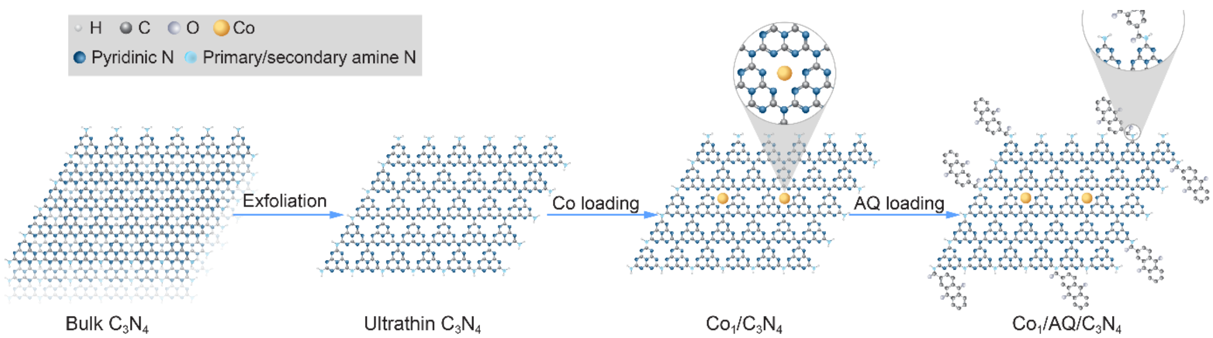

Figure 20. Synthesis of $Co_1/AQ/C_3N_4$. Spatial separation of Co single atom (as oxidation center) and anthraquinone (AQ; as reduction center) co-catalysts by anchoring them in the center (i.e., pyridinic N) and on the edge (i.e., primary/secondary amine N) of 2D ultrathin C_3N_4, respectively.

We first prepared ultrathin C_3N_4 nanosheets by exfoliating bulk C_3N_4 under probe-sonication.[78] The C_3N_4 nanosheets appeared to be only a few-layer-thick according to high-resolution transmission electron microscopy (HRTEM) images (Figure 21a). We then loaded Co onto ultrathin C_3N_4 using a two-step synthesis: attachment of Co precursors to anchor sites followed by pyrolysis.[79] As suggested by the lowest relative energy,[80] Co ions are embedded in the void center of C_3N_4 nanosheets through forming stable coordination with pyridinic N atoms in surrounding heptazine units of C_3N_4 (Figure 20).[81] After pyrolysis under N_2 atmosphere, Co ions were further phosphodized under PH_3 atmosphere to enhance their activity for water oxidation.[72, 79, 82] Consistent with the absence of Co metallic clusters in HAADF-STEM images, the coordination with P is further supported by the occurrence of a prominent Co-P peak at 129.6 eV in the X-ray photoelectron spectroscopy (XPS) spectrum (Figure 22). A P-N peak at 133.6 eV also suggests that P atoms coordinate with N atoms in heptazine rings of C_3N_4.

Secondly, we loaded AQ co-catalyst onto Co_1/C_3N_4 by forming amide bonds between carboxylic groups in anthraquinone-2-carboxylic acid and primary/secondary amine groups on the edge of C_3N_4 (Figure 20).[63, 81] Successful loading of AQ was confirmed by XPS in which $Co_1/AQ/C_3N_4$ exhibits strong peak corresponding to C-C fragments (284.7 eV) that mostly originate from AQ molecules (Figure 22). The AQ molecules remained bound to C_3N_4 after intensive solvent washing, suggesting that they are chemically attached rather than physically adsorbed. The successful loading of AQ was also confirmed by Fourier-transform infrared spectroscopy (FT-IR) spectroscopy. As shown in Figure 21f, the intensities of the FT-IR peaks corresponding to the amide functionalities, including the C=O stretching vibration peak at 1627 cm^{-1} and the N-H stretching vibration peak at 3076 cm^{-1}, increased dramatically with AQ loading. The quantitative analysis of XPS spectra indicates that AQ was loaded at 16% (w/w).

To provide a visual confirmation of the site-selective loading of AQ, we photoreductively deposited noble metals by reducing metal precursors (i.e., H_2AuCl_4 or H_2PtCl_6) on AQ as seed sites ($M^{n+} + ne^- \rightarrow M^0$).[83] TEM images clearly showed that the Au and Pt nanoparticles were selectively deposited on the edge of C_3N_4 nanosheets (Figure 21g), which were in stark contrast to random deposition of Au and Pt nanoparticles on pristine C_3N_4 surface without AQ functionality.[84] These results confirm that AQ co-catalysts were selectively loaded on the edge of C_3N_4 nanosheets and serve as reduction center.

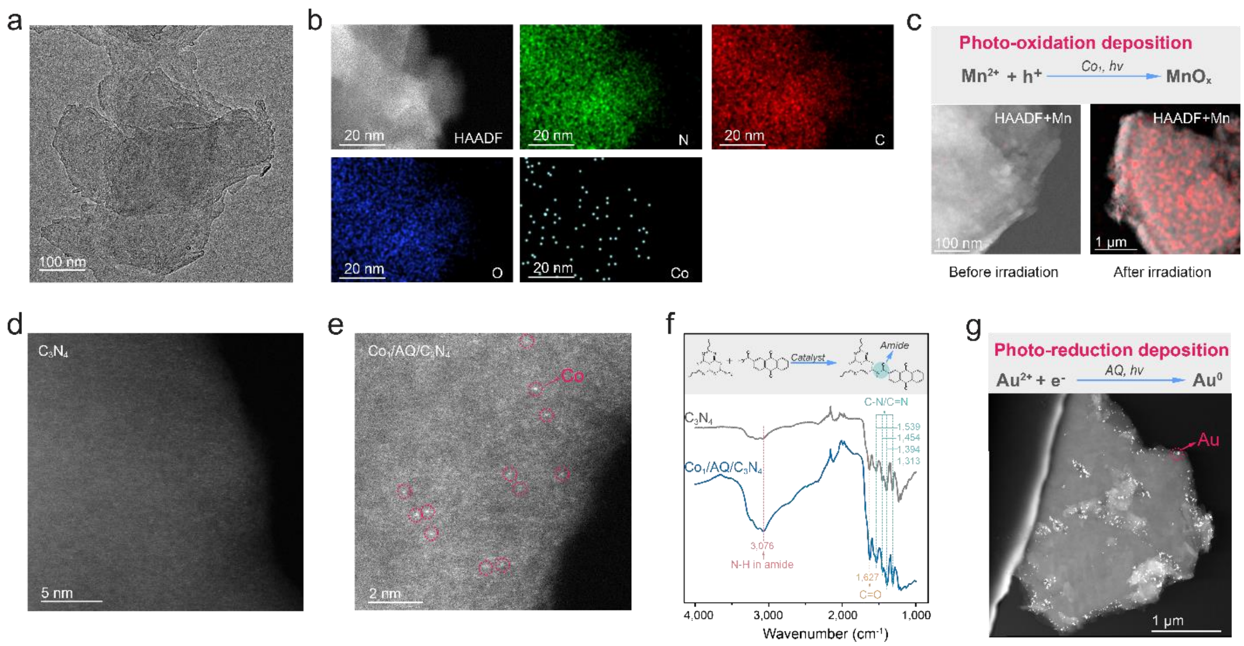

Figure 21. Material characterization of $Co_1/AQ/C_3N_4$. (a)-(b) HRTEM and EDS images of $Co_1/AQ/C_3N_4$. (c) Photooxidative deposition of Mn on Co_1/C_3N_4. (d)-(e) HAADF-STEM image of C_3N_4 and $Co_1/AQ/C_3N_4$. (f) FT-IR spectra of C_3N_4 and $Co_1/AQ/C_3N_4$. (g) Photoreductive deposition of Au on AQ/C_3N_4.

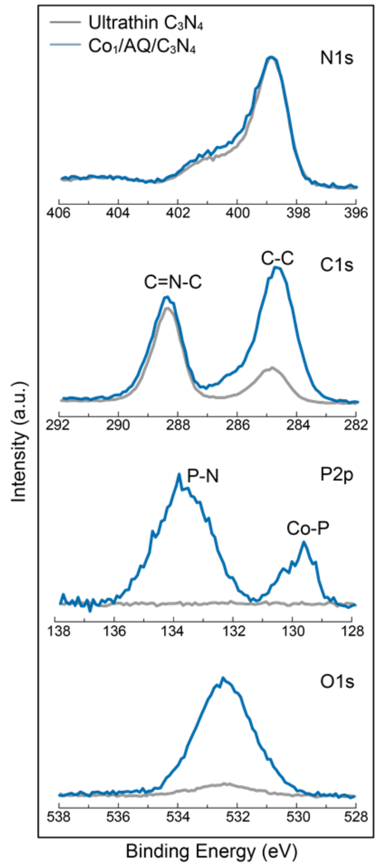

Figure 22. XPS spectrum of C_3N_4 and $Co_1/AQ/C_3N_4$.

Loading Co single atom largely enhanced the capability of C_3N_4 for water oxidation ($2H_2O \rightarrow O_2 + 4H^+ + 4e^-$), as indicated by 8.4-fold enhancement on 4-h O_2 production (Figure 23a). Loading AQ co-catalyst onto C_3N_4 had a significant impact on enhancing the selectivity of H_2O_2 synthesis from ~30% by pristine C_3N_4 to over 60% (Figure 23b; H_2O_2 production selectivity is defined as the ratio of electrons utilized for H_2O_2 synthesis to the total number of electrons consumed[21]). In contrast, C_3N_4 exfoliation or Co loading had limited impact on H_2O_2 production selectivity (Figure 23b). The enhanced H_2O_2 production selectivity is attributed to the two-step reaction catalyzed by AQ: (1) reductive hydrogenation of AQ to hydroxyanthraquinone (AQH_2) utilizing 2 e^- from photoexcited C_3N_4 followed by (2) H_2O_2 formation from concurrent oxygen reduction and dehydrogenation of AQH_2 back to AQ. Simultaneous loading of Co SAC and AQ co-catalyst significantly enhanced H_2O_2 production by a factor of 7.3 (Figure 23d).

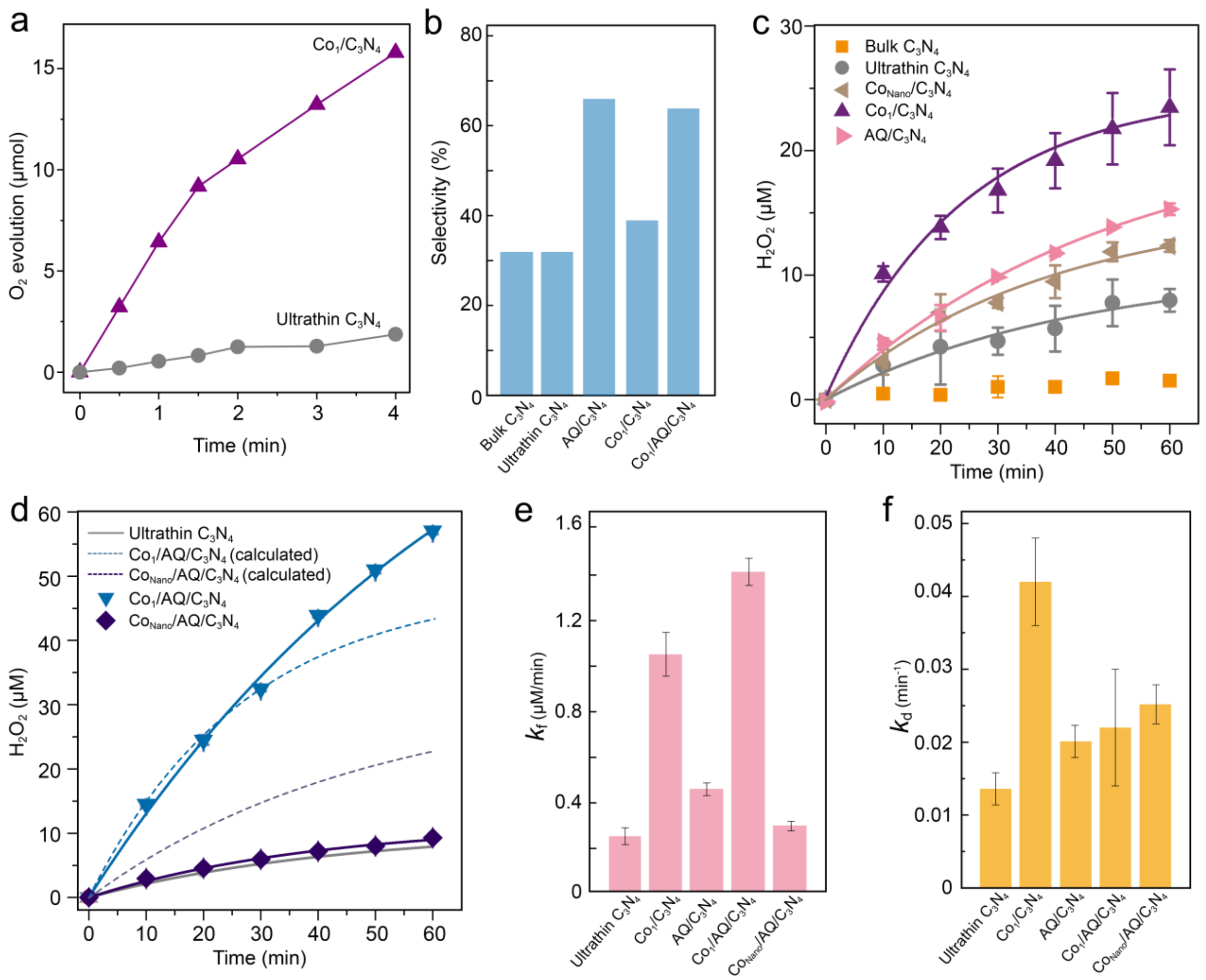

Figure 23. Photocatalytic H_2O_2 generation of $Co_1/AQ/C_3N_4$. (a) Time course of O_2 evolution measured under 0.6 kPa Ar pressure and 300 W Xenon lamp irradiation with 0.5 g/L of catalyst, 1 g/L La_2O_3, and 20 mM $AgNO_3$ in 100 mL water. (b) Selectivity of H_2O_2 production. (c)-(d) Time course of H_2O_2 production measured under simulated sunlight irradiation (Xenon lamp solar simulator, 100 mW/cm^2, AM 1.5G) with 0.5 g/L of catalyst under O_2-saturated condition. Solid lines are the fitting result of the kinetic model. Dotted lines are H_2O_2 productions estimated assuming additive enhancement of each co-catalyst. (e)-(f) H_2O_2 formation and decomposition rate constants. Error bars represent the standard deviations of triplicates.

We further analyze the H_2O_2 production by evaluating the rate of H_2O_2 formation (k_f) separately from the rate of H_2O_2 decomposition (k_d). The results show that H_2O_2 formation rate constant increased upon individual loading of Co single atom, Co nanoparticle, or AQ. While simultaneous loading of Co single atom and AQ lead to additive enhancement on k_f, simultaneous loading of Co nanoparticle and AQ had an antagonistic effect on k_f (Figure 23e), once again highlighting the importance of controlled physical separation between Co and AQ. It is also noteworthy that Co may negatively impact H_2O_2 synthesis performance by enhancing the oxidative decomposition of H_2O_2 (Figure 23f). This catalyzed H_2O_2 decomposition was minimized by separating H_2O_2 production centers (i.e., AQ) from Co decomposition sites, as indicated by much lower k_d in $Co_1/AQ/C_3N_4$ system as compared to Co_1/C_3N_4 system.

Results of this study suggest a new facile strategy to anchor two spatially-separated co-catalysts on a 2D photocatalyst. Such spatial separation ensures that the functions of both co-catalysts (i.e., Co_1 for enhanced water oxidation activity and AQ for improved H_2O_2 production selectivity) are fully utilized, resulting in additive enhancement in H_2O_2 photosynthesis. This center/edge strategy for loading two spatially-separated co-catalysts may be also applicable on other 2D photocatalysts for achieving efficient charge separation while maintaining the effectiveness of both co-catalysts.

4.6 Conclusion

The improved performance of AQ–C_3N_4 over bare C_3N_4 marks a significant improvement over previous electrocatalysts that utilize AQ as active catalytic centers[53-55, 85] which previously suffered from either a low yield (<10 mmol/$g_{catalyst}$ per hour)[53] and efficiency (<30 %)[54] or an excessively high overpotential requirement (1.4 V).[54] We attribute the observed improvement to the use of C_3N_4 as a conductive support enabled a very high loading of AQ, up to 20 weight percent (wt%) via chemical anchoring. The covalent bonding improves not only the catalyst stability but also the change transfer rate to AQ catalytic centers. The AQ–C_3N_4 loaded GDEs and other cell components showed negligible effect on H_2O_2 decomposition.

However, compared with other non-metal electrocatalysts (Table 1), AQ–C_3N_4 electrocatalyst showed lower apparent Faradaic efficiency than the state-of-the-art due to hydrogen evolution side reactions. The current AQ modification method cannot cover all the reaction sites of C_3N_4. Therefore, it is likely that a portion of electron-transfer events are responsible for H_2 evolution (0 V vs. RHE). Despite negligible H_2O_2 decomposition under open circuits, it is possible that anodic oxidation (Equation 14) or self-decomposition (Equation 15) of H_2O_2 may occur on the counter electrode under operation.[47]

$$H_2O_2 + 2\,H^+ + 2e^- \rightarrow 2\,H_2O \qquad \text{(Equation 14)}$$

$$2\,H_2O_2 \rightarrow 2\,H_2O + O_2\,(g) \qquad \text{(Equation 15)}$$

This electrochemical H_2O_2 cell, therefore, could be further improved by developing a more selective O_2-reduction electrocatalyst which lowers overpotential and impedes O_2 reduction into H_2O, by employing a flow cell design to minimize counter-electrode decomposition reactions, and by developing a selective water-oxidation counter electrode to produce H_2O_2 rather than to consume H_2O_2.

Moreover, spatial separation of oxidative and reductive co-catalysts was achieved, for the first time on a 2D photocatalyst, by coordinating cobalt single atom at the void center of C_3N_4 and anchoring anthraquinone at the edges of C_3N_4 nanosheets. This center/edge strategy for spatial separation of co-catalysts may be applied on other 2D photocatalysts that are increasingly studied in photosynthetic reactions.

4.7 References

1. Kosaka, K.; Yamada, H.; Shishida, K.; Echigo, S.; Minear, R. A.; Tsuno, H.; Matsui, S. Evaluation of the Treatment Performance of a Multistage Ozone/Hydrogen Peroxide Process by Decomposition By-Products. *Water Research* **2001,** *35* (15), 3587-3594.

2. The History of Hydrogen Peroxide Propulsion. http://www.peroxidepropulsion.com/article/2.

3. Michaelson, K. The Rocketman Checks In: One of a Kind List of Rocket Cars. **2011**.

4. Sanli, A. E.; Aytaç, A. Response to Disselkamp: Direct Peroxide/Peroxide Fuel Cell as a Novel Type Fuel Cell. *International Journal of Hydrogen Energy* **2011,** *36* (1), 869-875.

5. Yamazaki, S.-i.; Siroma, Z.; Senoh, H.; Ioroi, T.; Fujiwara, N.; Yasuda, K. A Fuel Cell with Selective Electrocatalysts Using Hydrogen Peroxide as Both an Electron Acceptor and a Fuel. *Journal of Power Sources* **2008,** *178* (1), 20-25.

6. Yamada, Y.; Yoneda, M.; Fukuzumi, S. High and Robust Performance of H_2O_2 Fuel Cells in the Presence of Scandium Ion. *Energy & Environmental Science* **2015,** *8* (6), 1698-1701.

7. Campos-Martin, J. M.; Blanco-Brieva, G.; Fierro, J. L. G. Hydrogen Peroxide Synthesis: An Outlook beyond the Anthraquinone Process. *Angewandte Chemie International Edition* **2006,** *45* (42), 6962-6984.

8. Hâncu, D.; Green, J.; Beckman, E. J. H_2O_2 in CO_2/H_2O Biphasic Systems: Green Synthesis and Epoxidation Reactions. *Industrial & Engineering Chemistry Research* **2002,** *41* (18), 4466-4474.

9. Kang, Q.; Liu, S.; Yang, L.; Cai, Q.; Grimes, C. A. Fabrication of PbS Nanoparticle-Sensitized TiO2 Nanotube Arrays and Their Photoelectrochemical Properties. *ACS Applied Materials & Interfaces* **2011,** *3* (3), 746-749.

10. Čolić, V.; Yang, S.; Révay, Z.; Stephens, I. E. L.; Chorkendorff, I. Carbon catalysts for electrochemical hydrogen peroxide production in acidic media. *Electrochimica Acta* **2018,** *272*, 192-202.

11. Liu, Y.; Quan, X.; Fan, X.; Wang, H.; Chen, S. High-Yield Electrosynthesis of Hydrogen Peroxide from Oxygen Reduction by Hierarchically Porous Carbon. *Angewandte Chemie* **2015,** *127* (23), 6941-6945.

12. Gao, G.; Zhang, Q.; Hao, Z.; Vecitis, C. D. Carbon Nanotube Membrane Stack for Flow-through Sequential Regenerative Electro-Fenton. *Environ Sci Technol* **2015,** *49* (4), 2375-2383.

13. Lu, Z.; Chen, G.; Siahrostami, S.; Chen, Z.; Liu, K.; Xie, J.; Liao, L.; Wu, T.; Lin, D.; Liu, Y.; Jaramillo, T. F.; Nørskov, J. K.; Cui, Y. High-efficiency oxygen reduction to hydrogen peroxide catalysed by oxidized carbon materials. *Nature Catalysis* **2018,** *1* (2), 156-162.

14. Zhou, L.; Zhou, M.; Hu, Z.; Bi, Z.; Serrano, K. G. Chemically modified graphite felt as an efficient cathode in electro-Fenton for p-nitrophenol degradation. *Electrochimica Acta* **2014,** *140*, 376-383.

15. Pan, Z.; Wang, K.; Wang, Y.; Tsiakaras, P.; Song, S. In-situ electrosynthesis of hydrogen peroxide and wastewater treatment application: A novel strategy for graphite felt activation. *Applied Catalysis B: Environmental* **2018,** *237*, 392-400.

16. Sun, Y.; Sinev, I.; Ju, W.; Bergmann, A.; Dresp, S.; Kühl, S.; Spöri, C.; Schmies, H.; Wang, H.; Bernsmeier, D.; Paul, B.; Schmack, R.; Kraehnert, R.; Roldan Cuenya, B.; Strasser, P. Efficient Electrochemical Hydrogen Peroxide Production from Molecular Oxygen on Nitrogen-Doped Mesoporous Carbon Catalysts. *ACS Catalysis* **2018,** *8* (4), 2844-2856.

17. Sun, Y.; Li, S.; Jovanov, Z. P.; Bernsmeier, D.; Wang, H.; Paul, B.; Wang, X.; Kühl, S.; Strasser, P. Structure, Activity, and Faradaic Efficiency of Nitrogen-Doped Porous Carbon Catalysts for Direct Electrochemical Hydrogen Peroxide Production. *ChemSusChem* **2018,** *11* (19), 3388-3395.

18. Fellinger, T.-P.; Hasché, F.; Strasser, P.; Antonietti, M. Mesoporous Nitrogen-Doped Carbon for the Electrocatalytic Synthesis of Hydrogen Peroxide. *Journal of the American Chemical Society* **2012,** *134* (9), 4072-4075.

19. Chen, S.; Chen, Z.; Siahrostami, S.; Higgins, D.; Nordlund, D.; Sokaras, D.; Kim, T. R.; Liu, Y.; Yan, X.; Nilsson, E.; Sinclair, R.; Nørskov, J. K.; Jaramillo, T. F.; Bao, Z. Designing Boron Nitride Islands in Carbon Materials for Efficient Electrochemical Synthesis of Hydrogen Peroxide. *Journal of the American Chemical Society* **2018,** *140* (25), 7851-7859.

20. Kim, H. W.; Ross, M. B.; Kornienko, N.; Zhang, L.; Guo, J.; Yang, P.; McCloskey, B. D. Efficient hydrogen peroxide generation using reduced graphene oxide-based oxygen reduction electrocatalysts. *Nature Catalysis* **2018,** *1* (4), 282-290.

21. Shiraishi, Y.; Kanazawa, S.; Sugano, Y.; Tsukamoto, D.; Sakamoto, H.; Ichikawa, S.; Hirai, T. Highly Selective Production of Hydrogen Peroxide on Graphitic Carbon Nitride (g-C3N4) Photocatalyst Activated by Visible Light. *ACS Catalysis* **2014,** *4* (3), 774-780.

22. Wei, Z.; Liu, M.; Zhang, Z.; Yao, W.; Tan, H.; Zhu, Y. Efficient visible-light-driven selective oxygen reduction to hydrogen peroxide by oxygen-enriched graphitic carbon nitride polymers. *Energy & Environmental Science* **2018,** *11* (9), 2581-2589.

23. Zhang, X.; Xie, X.; Wang, H.; Zhang, J.; Pan, B.; Xie, Y. Enhanced Photoresponsive Ultrathin Graphitic-Phase C_3N_4 Nanosheets for Bioimaging. *Journal of the American Chemical Society* **2013,** *135* (1), 18-21.

24. Kim, H. I., Choi, Y., Hu, S., Choi, W., & Kim, J. H. . Photocatalytic hydrogen peroxide production by anthraquinone-augmented polymeric carbon nitride. *Applied Catalysis B: Environmental* **2018,** *229*, 121-129.

25. Valeur, E.; Bradley, M. Amide Bond Formation: Beyond the Myth of Coupling Reagents. *Chemical Society Reviews* **2009,** *38* (2), 606-631.

26. Chu, C.; Erickson, P. R.; Lundeen, R. A.; Stamatelatos, D.; Alaimo, P. J.; Latch, D. E.; McNeill, K. Photochemical and Nonphotochemical Transformations of Cysteine with Dissolved Organic Matter. *Environ Sci Technol* **2016,** *50* (12), 6363-6373.

27. Yan, J.; Han, X.; Qian, J.; Liu, J.; Dong, X.; Xi, F. Preparation of 2D Graphitic Carbon Nitride Nanosheets By a Green Exfoliation Approach and the Enhanced Photocatalytic Performance. *Journal of Materials Science* **2017,** *52* (22), 13091-13102.

28. Payne, B. P.; Biesinger, M. C.; McIntyre, N. S. X-ray Photoelectron Spectroscopy Studies of Reactions on Chromium Metal and Chromium Oxide Surfaces. *Journal of Electron Spectroscopy and Related Phenomena* **2011,** *184* (1), 29-37.

29. Li, D.; Jia, S.; Fodjo, E. K.; Xu, H.; Wang, Y.; Deng, W. In situ SERS and X-ray Photoelectron Spectroscopy Studies on the pH-Dependant Adsorption of Anthraquinone-2-Carboxylic Acid on Silver Electrode. *Applied Surface Science* **2016,** *367*, 153-159.

30. Higo, M.; Miake, T.; Mitsushio, M.; Yoshidome, T.; Ozono, Y. Adsorption State and Morphology of Anthraquinone-2-carboxylic Acid Deposited from Solution onto the Atomically-Smooth Native Oxide Surface of Al(111) Films Studied by Infrared Reflection Absorption Spectroscopy, X-ray Photoelectron Spectroscopy, and Atomic Force Microscopy. *Analytical Sciences* **2008,** *24* (3), 313-320.

31. Han, S. W.; Ha, T. H.; Kim, C. H.; Kim, K. Self-Assembly of Anthraquinone-2-carboxylic Acid on Silver: Fourier Transform Infrared Spectroscopy, Ellipsometry, Quartz Crystal Microbalance, and Atomic Force Microscopy Study. *Langmuir* **1998,** *14* (21), 6113-6120.

32. Barth, A. Infrared spectroscopy of proteins. *Biochimica et Biophysica Acta (BBA) - Bioenergetics* **2007,** *1767* (9), 1073-1101.

33. Fina, F.; Callear, S. K.; Carins, G. M.; Irvine, J. T. S. Structural Investigation of Graphitic Carbon Nitride via XRD and Neutron Diffraction. *Chemistry of Materials* **2015,** *27* (7), 2612-2618.

34. Viswanathan, V.; Hansen, H. A.; Rossmeisl, J.; Nørskov, J. K. Unifying the $2e^-$ and $4e^-$ Reduction of Oxygen on Metal Surfaces. *The Journal of Physical Chemistry Letters* **2012,** *3* (20), 2948-2951.

35. Hwang, B.-J.; Chen, H.-C.; Mai, F.-D.; Tsai, H.-Y.; Yang, C.-P.; Rick, J.; Liu, Y.-C. Innovative Strategy on Hydrogen Evolution Reaction Utilizing Activated Liquid Water. *Scientific Reports* **2015,** *5*, 16263.

36. Pei, Z.; Zhao, J.; Huang, Y.; Huang, Y.; Zhu, M.; Wang, Z.; Chen, Z.; Zhi, C. Toward Enhanced Activity of a Graphitic Carbon Nitride-Based Electrocatalyst in Oxygen Reduction and Hydrogen Evolution Reactions via Atomic Sulfur Doping. *Journal of Materials Chemistry A* **2016,** *4* (31), 12205-12211.

37. Shinde, S. S.; Sami, A.; Lee, J.-H. Electrocatalytic Hydrogen Evolution Using Graphitic Carbon Nitride Coupled with Nanoporous Graphene Co-Doped by S and Se. *Journal of Materials Chemistry A* **2015,** *3* (24), 12810-12819.

38. Wang, X.; Maeda, K.; Thomas, A.; Takanabe, K.; Xin, G.; Carlsson, J. M.; Domen, K.; Antonietti, M. A Metal-Free Polymeric Photocatalyst for Hydrogen Production from Water under Visible Light. *Nature Materials* **2008,** *8*, 76.

39. Jiang, K.; Back, S.; Akey, A. J.; Xia, C.; Hu, Y.; Liang, W.; Schaak, D.; Stavitski, E.; Nørskov, J. K.; Siahrostami, S.; Wang, H. Highly selective oxygen reduction to hydrogen peroxide on transition metal single atom coordination. *Nature Communications* **2019,** *10* (1), 3997.

40. Kulkarni, A.; Siahrostami, S.; Patel, A.; Nørskov, J. K. Understanding Catalytic Activity Trends in the Oxygen Reduction Reaction. *Chemical Reviews* **2018,** *118* (5), 2302-2312.

41. Kofuji, Y.; Isobe, Y.; Shiraishi, Y.; Sakamoto, H.; Ichikawa, S.; Tanaka, S.; Hirai, T. Hydrogen Peroxide Production on a Carbon Nitride–Boron Nitride-Reduced Graphene Oxide Hybrid Photocatalyst under Visible Light. *ChemCatChem* **2018,** *10* (9), 2070-2077.

42. Zhang, G.; Yang, F. Direct electrochemisty and electrocatalysis of anthraquinone-monosulfonate/polyaniline hybrid film synthesized by a novel electrochemical doping-dedoping-redoping method on pre-activated spectroscopically pure graphite surface. *Physical Chemistry Chemical Physics* **2011,** *13* (8), 3291-3302.

43. Vaik, K.; Mäeorg, U.; Maschion, F. C.; Maia, G.; Schiffrin, D. J.; Tammeveski, K. Electrocatalytic oxygen reduction on glassy carbon grafted with anthraquinone by anodic oxidation of a carboxylate substituent. *Electrochimica Acta* **2005,** *50* (25), 5126-5131.

44. Murray, A. T.; Voskian, S.; Schreier, M.; Hatton, T. A.; Surendranath, Y. Electrosynthesis of Hydrogen Peroxide by Phase-Transfer Catalysis. *Joule*.

45. Salimi, A.; Eshghi, H.; Sharghi, H.; Golabi, S. M.; Shamsipur, M. Electrocatalytic Reduction of Dioxygen at the Surface of Glassy Carbon Electrodes Modified by Some Anthraquinone Substituted Podands. *Electroanalysis* **1999,** *11* (2), 114-119.

46. Tammeveski, K.; Kontturi, K.; Nichols, R. J.; Potter, R. J.; Schiffrin, D. J. Surface Redox Catalysis for O_2 Reduction On Quinone-Modified Glassy Carbon Electrodes. *Journal of Electroanalytical Chemistry* **2001,** *515* (1), 101-112.

47. Barros, W. R. P.; Ereno, T.; Tavares, A. C.; Lanza, M. R. V. In Situ Electrochemical Generation of Hydrogen Peroxide in Alkaline Aqueous Solution by using an Unmodified Gas Diffusion Electrode. *ChemElectroChem* **2015,** *2* (5), 714-719.

48. Qiang, Z.; Chang, J.-H.; Huang, C.-P. Electrochemical Generation of Hydrogen Peroxide from Dissolved Oxygen In Acidic Solutions. *Water Res* **2002,** *36* (1), 85-94.

49. Vander Griend, D. A.; Golden, J. S.; Arrington, C. A. Kinetics and Mechanism of Chromate Reduction with Hydrogen Peroxide in Base. *Inorganic Chemistry* **2002,** *41* (26), 7042-7048.

50. Loeffler, M. J.; Teolis, B. D.; Baragiola, R. A. Decomposition of Solid Amorphous Hydrogen Peroxide By Ion Irradiation. *The Journal of Chemical Physics* **2006,** *124* (10), 104702.

51. Popat, S. C.; Ki, D.; Rittmann, B. E.; Torres, C. I. Importance of OH^{-} Transport from Cathodes in Microbial Fuel Cells. *ChemSusChem* **2012,** *5* (6), 1071-1079.

52. Dong, H.; Zhang, X.; Yu, H.; Yu, H. Graphene-Doped Carbon Black Gas Diffusion Electrode for Nonmetallic Electrochemical Advanced Oxidation Process Under Mild Conditions. *Environmental Technology* **2018,** *39* (22), 2959-2966.

53. Wang, A.; Bonakdarpour, A.; Wilkinson, D. P.; Gyenge, E. Novel organic redox catalyst for the electroreduction of oxygen to hydrogen peroxide. *Electrochimica Acta* **2012,** *66*, 222-229.

54. Valim, R. B.; Reis, R. M.; Castro, P. S.; Lima, A. S.; Rocha, R. S.; Bertotti, M.; Lanza, M. R. V. Electrogeneration of hydrogen peroxide in gas diffusion electrodes modified with tert-butyl-anthraquinone on carbon black support. *Carbon* **2013,** *61*, 236-244.

55. Zhang, G.; Wang, S.; Zhao, S.; Fu, L.; Chen, G.; Yang, F. Oxidative degradation of azo dye by hydrogen peroxide electrogenerated in situ on anthraquinonemonosulphonate/polypyrrole composite cathode with heterogeneous $CuO/\gamma\text{-}Al_2O_3$ catalyst. *Applied Catalysis B: Environmental* **2011,** *106* (3), 370-378.

56. Hisatomi, T.; Kubota, J.; Domen, K. Recent advances in semiconductors for photocatalytic and photoelectrochemical water splitting. *Chemical Society Reviews* **2014,** *43* (22), 7520-7535.

57. Chu, C.; Huang, D.; Zhu, Q.; Stavitski, E.; Spies, J. A.; Pan, Z.; Mao, J.; Xin, H. L.; Schmuttenmaer, C. A.; Hu, S.; Kim, J.-H. Electronic Tuning of Metal Nanoparticles for Highly Efficient Photocatalytic Hydrogen Peroxide Production. *ACS Catalysis* **2019**, 626-631.

58. Kofuji, Y.; Isobe, Y.; Shiraishi, Y.; Sakamoto, H.; Tanaka, S.; Ichikawa, S.; Hirai, T. Carbon nitride-aromatic diimide-graphene nanohybrids: metal-free photocatalysts for solar-to-hydrogen peroxide energy conversion with 0.2% efficiency. *Journal of the American Chemical Society* **2016,** *138* (31), 10019-10025.

59. Shiraishi, Y.; Takii, T.; Hagi, T.; Mori, S.; Kofuji, Y.; Kitagawa, Y.; Tanaka, S.; Ichikawa, S.; Hirai, T. Resorcinol–formaldehyde resins as metal-free semiconductor photocatalysts for solar-to-hydrogen peroxide energy conversion. *Nature Materials* **2019**.

60. Liu, J.; Liu, Y.; Liu, N. Y.; Han, Y. Z.; Zhang, X.; Huang, H.; Lifshitz, Y.; Lee, S. T.; Zhong, J.; Kang, Z. H. Metal-free efficient photocatalyst for stable visible water splitting via a two-electron pathway. *Science* **2015,** *347* (6225), 970-974.

61. Goto, Y.; Hisatomi, T.; Wang, Q.; Higashi, T.; Ishikiriyama, K.; Maeda, T.; Sakata, Y.; Okunaka, S.; Tokudome, H.; Katayama, M.; Akiyama, S.; Nishiyama, H.; Inoue, Y.; Takewaki, T.; Setoyama, T.; Minegishi, T.; Takata, T.; Yamada, T.; Domen, K. A Particulate Photocatalyst Water-Splitting Panel for Large-Scale Solar Hydrogen Generation. *Joule* **2018,** *2* (3), 509-520.

62. Chen, X.; Shen, S.; Guo, L.; Mao, S. S. Semiconductor-based photocatalytic hydrogen generation. *Chem Rev* **2010,** *110* (11), 6503-70.

63. Ong, W. J.; Tan, L. L.; Ng, Y. H.; Yong, S. T.; Chai, S. P. Graphitic Carbon Nitride (g-C3N4)-Based Photocatalysts for Artificial Photosynthesis and Environmental Remediation: Are We a Step Closer To Achieving Sustainability? *Chemical Reviews* **2016,** *116* (12), 7159-329.

64. Wang, D.; Hisatomi, T.; Takata, T.; Pan, C.; Katayama, M.; Kubota, J.; Domen, K. Core/Shell photocatalyst with spatially separated co-catalysts for efficient reduction and oxidation of water. *Angew Chem Int Ed Engl* **2013,** *52* (43), 11252-6.

65. Maeda, K.; Xiong, A.; Yoshinaga, T.; Ikeda, T.; Sakamoto, N.; Hisatomi, T.; Takashima, M.; Lu, D.; Kanehara, M.; Setoyama, T.; Teranishi, T.; Domen, K. Photocatalytic overall water splitting promoted by two different cocatalysts for hydrogen and oxygen evolution under visible light. *Angew Chem Int Ed Engl* **2010,** *49* (24), 4096-9.

66. Ma, S. S. K.; Maeda, K.; Abe, R.; Domen, K. Visible-light-driven nonsacrificial water oxidation over tungsten trioxide powder modified with two different cocatalysts. *Energy & Environmental Science* **2012,** *5* (8), 8390-8397.

67. Shiraishi, Y.; Kanazawa, S.; Kofuji, Y.; Sakamoto, H.; Ichikawa, S.; Tanaka, S.; Hirai, T. Sunlight-driven hydrogen peroxide production from water and molecular oxygen by metal-free photocatalysts. *Angew Chem Int Edit* **2014,** *53* (49), 13454-13459.

68. Kofuji, Y.; Ohkita, S.; Shiraishi, Y.; Sakamoto, H.; Tanaka, S.; Ichikawa, S.; Hirai, T. Graphitic carbon nitride doped with biphenyl diimide: efficient photocatalyst for hydrogen peroxide production from water and molecular oxygen by sunlight. *Acs Catalysis* **2016,** *6* (10), 7021-7029.

69. Mase, K.; Yoneda, M.; Yamada, Y.; Fukuzumi, S. Seawater usable for production and consumption of hydrogen peroxide as a solar fuel. *Nat. Commun.* **2016,** *7*, 11470.

70. Shiraishi, Y.; Kofuji, Y.; Sakamoto, H.; Tanaka, S.; Ichikawa, S.; Hirai, T. Effects of surface defects on photocatalytic H2O2 production by mesoporous graphitic carbon nitride under visible light irradiation. *Acs Catalysis* **2015,** *5* (5), 3058-3066.

71. Moon, G.-h.; Fujitsuka, M.; Kim, S.; Majima, T.; Wang, X.; Choi, W. Eco-Friendly Photochemical Production of H2O2 through O2 Reduction over Carbon Nitride Frameworks Incorporated with Multiple Heteroelements. *ACS Catalysis* **2017,** *7* (4), 2886-2895.

72. Zhong, D. K.; Gamelin, D. R. Photoelectrochemical Water Oxidation by Cobalt Catalyst ("Co-Pi")/alpha-Fe2O3 Composite Photoanodes: Oxygen Evolution and Resolution of a Kinetic Bottleneck. *Journal of the American Chemical Society* **2010,** *132* (12), 4202-4207.

73. Barroso, M.; Cowan, A. J.; Pendlebury, S. R.; Gratzel, M.; Klug, D. R.; Durrant, J. R. The role of cobalt phosphate in enhancing the photocatalytic activity of alpha-Fe2O3 toward water oxidation. *J Am Chem Soc* **2011,** *133* (38), 14868-71.

74. Khnayzer, R. S.; Mara, M. W.; Huang, J.; Shelby, M. L.; Chen, L. X.; Castellano, F. N. Structure and Activity of Photochemically Deposited "CoPi" Oxygen Evolving Catalyst on Titania. *Acs Catalysis* **2012,** *2* (10), 2150-2160.

75. Moon, G. H.; Kim, W.; Bokare, A. D.; Sung, N. E.; Choi, W. Solar production of H2O2 on reduced graphene oxide-TiO2 hybrid photocatalysts consisting of earth-abundant elements only. *Energy & Environmental Science* **2014,** *7* (12), 4023-4028.

76. Kanan, M. W.; Surendranath, Y.; Nocera, D. G. Cobalt-phosphate oxygen-evolving compound. *Chemical Society Reviews* **2009,** *38* (1), 109-114.

77. Campos-Martin, J. M.; Blanco-Brieva, G.; Fierro, J. L. G. Hydrogen peroxide synthesis: An outlook beyond the anthraquinone process. *Angew. Chem. Int. Ed.* **2006,** *45* (42), 6962-6984.

78. Zhang, X.; Xie, X.; Wang, H.; Zhang, J.; Pan, B.; Xie, Y. Enhanced photoresponsive ultrathin graphitic-phase C3N4 nanosheets for bioimaging. *J. Am. Chem. Soc.* **2013,** *135* (1), 18-21.

79. Liu, W.; Cao, L.; Cheng, W.; Cao, Y.; Liu, X.; Zhang, W.; Mou, X.; Jin, L.; Zheng, X.; Che, W.; Liu, Q.; Yao, T.; Wei, S. Single-Site Active Cobalt-Based Photocatalyst with a Long Carrier Lifetime for Spontaneous Overall Water Splitting. *Angew Chem Int Ed Engl* **2017,** *56* (32), 9312-9317.

80. Zheng, Y.; Jiao, Y.; Zhu, Y. H.; Cai, Q. R.; Vasileff, A.; Li, L. H.; Han, Y.; Chen, Y.; Qiao, S. Z. Molecule-Level g-C3N4 Coordinated Transition Metals as a New Class of Electrocatalysts for Oxygen Electrode Reactions. *Journal of the American Chemical Society* **2017,** *139* (9), 3336-3339.

81. Kessler, F. K.; Zheng, Y.; Schwarz, D.; Merschjann, C.; Schnick, W.; Wang, X. C.; Bojdys, M. J. Functional carbon nitride materials design strategies for electrochemical devices. *Nat Rev Mater* **2017,** *2* (6).

82. Kanan, M. W.; Nocera, D. G. In situ formation of an oxygen-evolving catalyst in neutral water containing phosphate and Co2+. *Science* **2008,** *321* (5892), 1072-5.

83. Li, R. G.; Zhang, F. X.; Wang, D. G.; Yang, J. X.; Li, M. R.; Zhu, J.; Zhou, X.; Han, H. X.; Li, C. Spatial separation of photogenerated electrons and holes among {010} and {110} crystal facets of BiVO4. *Nature Communications* **2013,** *4*.

84. Xue, J.; Ma, S.; Zhou, Y.; Zhang, Z.; He, M. Facile Photochemical Synthesis of Au/Pt/g-C3N4 with Plasmon-Enhanced Photocatalytic Activity for Antibiotic Degradation. *ACS Applied Materials & Interfaces* **2015,** *7* (18), 9630-9637.

85. Zhao, S.; Zhang, G.; Fu, L.; Liu, L.; Fang, X.; Yang, F. Enhanced Electrocatalytic Performance of Anthraquinonemonosulfonate-Doped Polypyrrole Composite: Electroanalysis for the Specific Roles of Anthraquinone Derivative and Polypyrrole Layer on Oxygen Reduction Reaction. *Electroanalysis* **2010,** *23* (2), 355-363.

Chapter 5: Anthraquinone Modified Polyaniline

This Chapter is published (adapted):

Zhu, Q.; Hinkle, M.; Kim, D. J.; Kim, J.-H. Modular Hydrogen Peroxide Electrosynthesis Cell with Anthraquinone-Modified Polyaniline Electrocatalyst. *ACS ES&T Engineering* **2021,** *1* (3), 446-455.

5.1 Abstract

Advanced oxidation processes (AOPs) target the chemical destruction of a wide range of non-biodegradable, toxic, and recalcitrant organic pollutants instead of removal via physical separation, which produces contaminant-laden concentrates or solids. Hydrogen peroxide (H_2O_2) is the most widely used precursor that produces highly reactive and nonselective hydroxyl radical at the site of AOP through the activation by UV irradiation. The potential for AOPs to meet the growing demand of transforming centralized treatment and distribution practice into modular, small-scale, and decentralized treatment paradigm can be maximized by innovative technologies that can synthesize precursor chemicals also at the site of water treatment, eliminating the need for continuous chemical supply. We achieve high electrochemical H2O2 production efficiency by synthesizing an anthraquinone-modified polyaniline composite that enables efficient two-electron oxygen reduction reaction. Polyaniline functions as a conductive support with abundant attachment sites, and anthraquinone ensures the selective H_2O_2 generation. Polyanilines were synthesized via different polymerization pathways to achieve different morphologies for co-catalysts' covalent attachment. The electrochemical behaviors of

these polyaniline substrates and their anthraquinone-modified composites were examined and compared to propose the most suitable polyaniline substrate for H2O2 electrosynthesis.

5.2 Introduction

There has been a growing need to accomplish water treatment goals in decentralized systems in regions where centralized treatment and distribution via pipe network are no longer an appealing option. Such decentralized systems tend to be small in size, exhibit relatively low carbon footprint, and can be readily adaptable to various treatment scenarios ranging from potable water production in developing world and sparsely populated region to on-site treatment and recycling in various industry sectors.[1-4] Advanced oxidation process (AOP) is a particularly appealing treatment option in these scenarios, since it aims to destroy pollutants and convert them to benign end products rather than concentrate them for residuals disposal and additional treatment. Removal of non-biodegradable, recalcitrant, and toxic organic micropollutants is a prerequisite for potable water production and high purity water production for various industrial uses.[5-6]

One notable concern of AOP for decentralized, distributed application is its requirement to continuously supply precursor chemicals such as H_2O_2. In AOP, H_2O_2 is activated on site to produce $^{\bullet}OH$ via various activation strategies, with photolysis by ultraviolet (UV) irradiation as the benchmark method; *i.e.*, UV/H_2O_2 process. Currently H_2O_2 is manufactured at industrial scale via anthraquinone (AQ) process, which is both waste-intensive and energy-demanding, and therefore less environmentally friendly.[7] Electrochemically generating H_2O_2 generation via 2-electron oxygen reduction reaction (2 e^- ORR) with water, oxygen, and electricity as the only inputs is a promising alternative not only for less carbon footprint and energy requirement[8] but also for eliminating the need for H_2O_2 delivery and storage. Yet, H_2O_2 production electrocatalytic cell requires overcoming several technical challenges including the development of more efficient and selective electrocatalysts tailored for H_2O_2 synthesis in environmentally relevant conditions as well as scalable cell design, fabrication, and demonstration.

Given AQ's high activity and selectivity toward O_2 reduction to H_2O_2 that are well established in homogeneous-phase industrial-scale reactions, attempts have been made to exploit AQ in heterogeneous electrocatalysts for $2e^-$ ORR. Although a few materials have been previously reported as feasible electrocatalytic substrates for AQ and its derivatives, such as glassy carbon,[9] indium tin oxide,[10] graphene oxide,[11] and carbon nanotube (Table S1),[12] the AQ coverage density on the surface is relatively low (0.04 – 0.43 nmol cm^{-2}) due to the limited amount of anchoring sites in these materials for AQ attachment. The recently reported carbon nitride (C_3N_4), covalently decorated with AQ, greatly improved the coverage density with its amine groups at edge sites of its nanosheet,[13] while the low conductivities of C_3N_4 substrate restricted the overall performance of the composite material. Therefore, a conductive substrate with plentiful end groups is preferred as a supporting matrix.

We here explore polyaniline (PANI), a conductive polymer, as a substrate to anchor AQ catalysts to enable electrochemical H_2O_2 synthesis. PANI has been widely used for a variety of electrochemical applications, including energy storage and conversion such as supercapacitors, rechargeable batteries, and fuel cells.[14-16] Due to its intrinsic conductivity,[17] low-cost monomer, simple synthesis,[18] and environmental stability,[19] PANI stands out among other conducting polymers (polypyrrole, polyacetylene, polythiophene, etc.) as a promising non-metal conductive substrate and catalyst. We postulate that nitrogen heteroatoms groups present in the PANI backbone (*i.e.*, between repeating phenyl rings) can provide abundant sites to anchor a large amount of AQ molecules. We prepared different PANI and AQ-loaded PANI electrocatalysts and tested their activity and selectivity for $2e^-$ ORR.

5.3 Experimental Methods

5.3.1 Material synthesis

All chemicals were used as-received, and all masses were measured by an analytical balance (New Classic MF MS204S, Mettler Toledo). As-received PANI (PANI(AR)) was purchased in emeraldine base form with average molecular weight of 15,000 from Alfa Aesar. Another PANI sample was synthesized using homogeneous nucleation method.[20] Briefly, 0.6 mL aniline (≥ 99.5%) and 360 mg ammonium persulfate (APS) were dissolved in 20 mL of 1 M hydrochloric acid (HCl) solution separately.[20] We also employed 2 mg of carbon black (VULCAN XC72, Cabot, Figure 24a) or multi-walled carbon nanotube (Cheap Tubes, Figure 24b) to prepare composite PANI substrates. These carbon seeds were dispersed in 20 mL 1 M HCl solution with 0.6 mL aniline via 30 minutes of sonication, and 360 mg APS was also dissolved in 20 mL 1M HCl solution.[21] Aniline solution or aniline with carbon seeds suspension were mixed rapidly with APS solution by vigorous shaking for 30 seconds and let still for 2 hours.[20-21] The samples were then centrifuged and washed with 1 M HCl for one time and Milli-Q water (≥18.2 MΩ·cm, Millipore Water Purification System) for three times. Final products were freeze-dried under vacuum for 24 hours. For PANI with carbon black and carbon nanotube, the weights of final products were ~80 mg, and carbon seeding contents were 2.5 wt% in these samples.

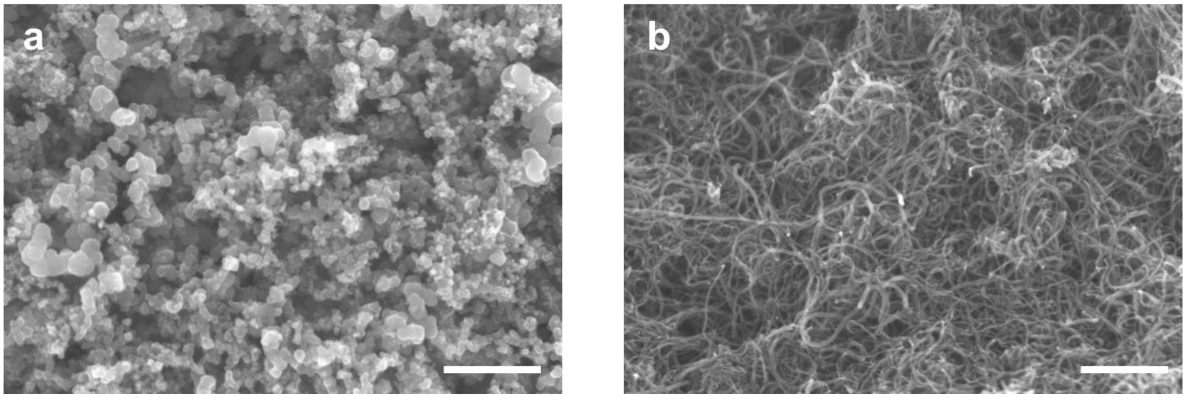

Figure 24. SEM pictures of carbon black and carbon nanotube. The white bars at bottom right corner represent the scales of 500 nm. CB (left) had particle sizes of 50-120 nm; CNT (right) had fiber lengths of 300-500 nm and widths of 10-20 nm.

For AQ modification, 100 mg PANI substrate was first dispersed in 20 mL dichloromethane (DCM) via 30 minutes of sonication, and 30 mg anthraquinone-2-carboxylic acid (AQ-COOH), 28.5 mg *N*-(3-dimethylaminopropyl)-*N'*-ethylcarbodiimide hydrochloride (EDC·HCl, carboxyl activating agent), 20 mg 1-hydroxybenzotriazole hydrate (HOBt, racemization inhibitor), and 20 mg *N*,*N*-diisopropylethylamine (DIEA, hindered base) were added to the suspension and stirred for 48 hours at room temperature.[22] The samples were centrifuged and washed with DCM for three times and with Milli-Q water for one time to remove unreacted and unbound AQ-COOH and other chemicals, and finally freeze-dried in vacuum for 24 hours. All the chemicals were purchased from Sigma-Aldrich and used without further purification.

For electropolymerization, a piece of carbon paper (Toray 120, Fisher) was first dried in an oven at 80 °C for 15 hours. After cooled to room temperature, it was immersed in a pre-mixed 0.5 M sulfuric acid + 0.1 M aniline aqueous solution with constant N_2 purging and stirring, where the immersed area was 1 cm^2 (1 cm×1 cm). Two programs of cyclic voltammetry (CV) were applied to the carbon paper: 1) during the first cycle, the electrode was scanned between -

0.255 and 0.845 V (vs. Ag/AgCl) at 2 mV s^{-1}; 2) during the following 200 cycles, the electrode was scanned between -0.255 and 0.735 V (vs. Ag/Ag/Cl) at 100 mV s^{-1}.[23] The electrode was then rinsed with DI water and dried in an oven at 80 °C for 15 hours and was named PANI(EP). The as-prepared PANI(EP) was then suspended in a beaker with 13.85 mg AQ-COOH, 15.78 mg EDC·HCl, 11.14 mg HOBt, and 10.65 mg DIEA dissolved in 20 mL DCM. The mixture solution was stirred at 500 rpm at room temperature for 48 hours over the electrode surface. The electrode, named AQ-PANI(EP), was then washed with DCM and DI water and dried in an oven at 80 °C for 15 hours.

5.3.2 Material characterization

Scanning electron microscopy (SEM) analysis was performed using a Hitachi SU8230 cold field emission SEM microscope (accelerating voltage = 1 kV) and a Hitachi SU-70 analytical field emission SEM microscope (accelerating voltage = 5 kV). Attenuated total reflectance-Fourier transform infrared (ATR-FTIR) spectra were performed with a Thermo Scientific Nicolet 6700 FTIR spectrometer equipped with an attenuated total reflectance cell. X-ray photoelectron spectroscopy (XPS) measurements were obtained with a PHI VersaProbe II Scanning XPS Microprobe equipped with a monochromated Al source. To minimize contamination by surface hydrocarbon (adventitious carbon), all samples were dried in a vacuum oven for 3 days, and then immediately transferred to an ultrahigh vacuum chamber for XPS analyses.

5.3.3 Electrochemical measurements

Electrochemical characterizations including cyclic voltammetry (CV), chronoamperometry (CA), chronopotentiometry (CP), and electrochemical impedance spectroscopy (EIS) were performed using a Bio-logic VSP potentiostat/galvanostat. To prepare the working electrodes, catalysts were dispersed in 75% (v/v) ethanol/water mixture by 30 minutes of sonication, and the suspensions were drop-casted onto carbon paper (Toray 120 for immersed electrode setup, Sigracet 39 BB for flow cell setup). The catalyst loadings were kept at 0.25 mg cm^{-2}. Electrodes were then dried in 80 °C oven for 16 hours.

For immersed electrode setup, a carbon rod (VWR) was used as the counter electrode, and an Ag/AgCl electrode filled with saturated KCl solution (CHI111, CH Instruments) was used as the reference electrode. Unless specified, CV tests were performed at a scan rate of 20 mV s^{-1}. CV, CA, and EIS were performed in 0.1 M phosphate buffer electrolytes of pH 8.8, containing sodium phosphate monobasic monohydrate and sodium phosphate dibasic. To remove metal ion impurities (i.e., Fe^{2+}) in the buffer electrolytes that would catalyze H_2O_2 degradation, pre-electrolysis was performed before electrochemical characterizations, where two carbon rods were set in a two-electrode system and a constant voltage of 3.5 V was applied for 24 hours. The electrolyte was purged with O_2 (Airgas, 99.996%) for 15 minutes before tests and purged continuously throughout the experiment. For double-layer capacitance (C_{DL}) measurements, both CV and EIS methods were used.[24] Electrodes in three-electrode system were tested with CV scans of 0.005, 0.01, 0.025, 0.05, 0,1, 0.2, 0.4, and 0.8 V s^{-1} from 0 V to 0.2 V vs. Ag/AgCl because all currents in this non-Faradaic potential region were assumed to be double-layer charging currents. The charging currents were plotted as a function of scan rates and the calculated slopes were double-layer capacitances. Electrodes were then measured with EIS from 200 kHz to 100 mHz at 0.1 V vs. Ag/AgCl, and modeled by a modified Randles circuit with solution resistance (R_s, Ω), constant-phase element (CPE), and charge transfer resistance (R_{ct}, Ω).

Double layer capacitance was calculated by Equation 16, where Q_0 (F s^{a-1}) and a are constants from the model fittings:

$$C_{DL} = [Q_0 \left(\frac{1}{Rs} + \frac{1}{Rct}\right)^{(a-1)}]^{1/a} \quad \text{(Equation 16)}$$

5.4 Results and Discussion

5.4.1 Material synthesis

PANI can be polymerized from aniline monomer following different synthetic procedures, including chemical (*e.g.*, heterophane, interfacial, seeding, metathesis, self-assembling, and sonochemical polymerizations) and electrochemical methods.[18, 25-26] Different synthesis methods and conditions result in different PANIs with distinct characteristics including chain length, morphology, oxidation state, and electrical conductivity.[17] Among the range of PANIs reported to date, emeraldine salt is known to be the most conductive form of PANI and has been demonstrated to exhibit great performance as an electrocatalyst.[17, 27-28] We therefore synthesized emeraldine salts using homogeneous nucleation (HN)[20] and nanofiber seeding (NS)[21] methods (Figure 25). These two facile and rapid synthesis methods are known to reproducibly produce PANI nanoparticles with well-controlled sizes and shapes. Two carbon materials, CB and CNT, were chosen as templates considering their intrinsic conductivity, low cost, and well-defined nanostructure. Such composite structure could also provide large surface areas to maximize anchoring sites for co-catalyst connection.[20-21]

5.4.2 Material characterizations

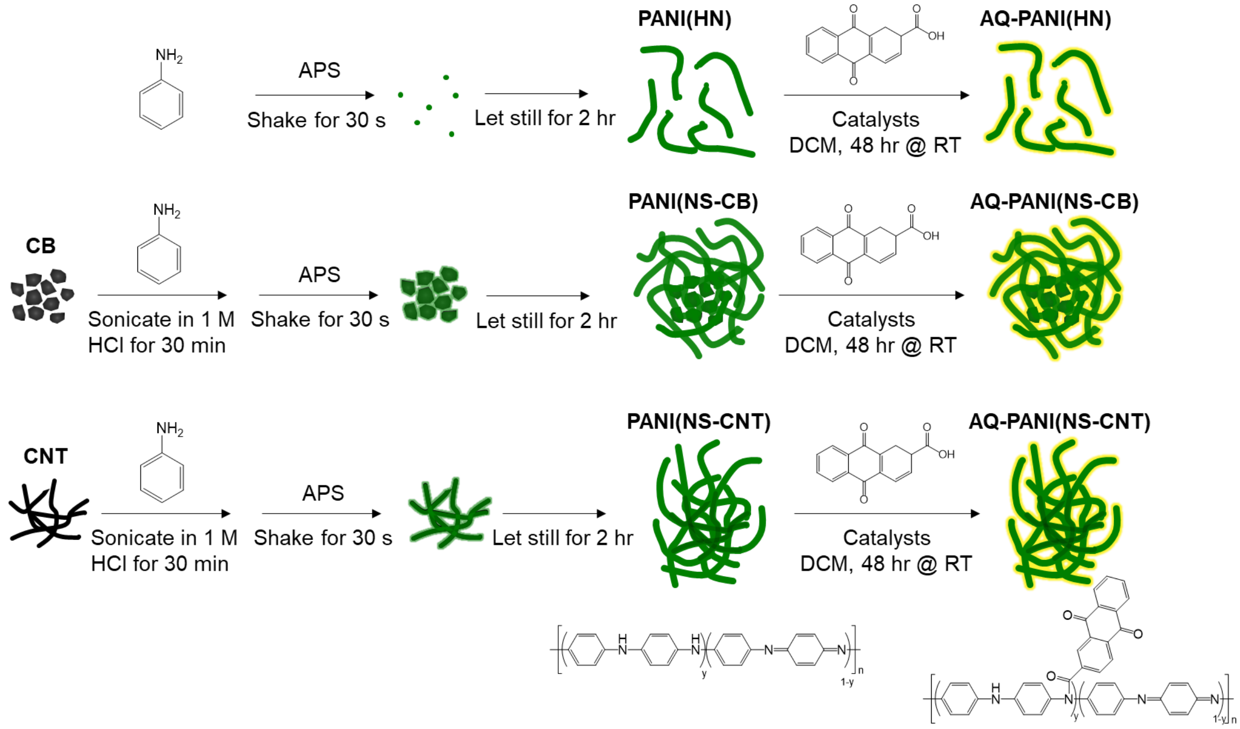

Figure 25. Proposed reaction mechanisms and chemical structures of PANI substrates and PANI-AQ composites.

SEM images in Figure 26 show the morphologies of PANI and PANI composites with carbon templates. The commercial control sample, PANI(AR), appeared as agglomerated coral-like granules of 3-5 µm in size (Figure 26a). This morphology reflected colloidal coagulation of polymers that occurred during extensive mechanical agitation employed in conventional precipitation polymerization process.[20, 29] In contrast, PANI synthesized by homogeneous nucleation (PANI(HN), Figure 26c) were mostly comprised of dispersed, smooth nanofibers with lengths of 100-300 nm and widths of 30-80 nm. Similarly, PANI synthesized via CB and CNT seeding (PANI(NS-CB), Figure 26e; PANI(NS-CNT), Figure 26g) showed fibrillar morphology of nanofibers with lengths of 400-1000 nm and widths of 50-100 nm. The CB and CNT functioned as nanoscale templates, minimizing aggregation and facilitating the directional growth of the polymer.[21] Although AQ modification did not induce any morphological change for PANI(AR) (Figure 26b), AQ-PANI(HN) and AQ-PANI(NS-CB) exhibited aggregate morphology compared with their substrates (Figure 26d,f) likely due to the poor dispersion of PANI in organic solvent (i.e., dichloromethane used during AQ anchoring). This phenomenon was not prominent in AQ-PANI(NS-CNT), potentially because CNT provided more stretched and rigid 1D scaffold, on which polyaniline nanofibers could more easily maintain their dispersity. The higher dispersity in composite materials in turn leads to better electrochemical performance than their counterparts.[30-31]

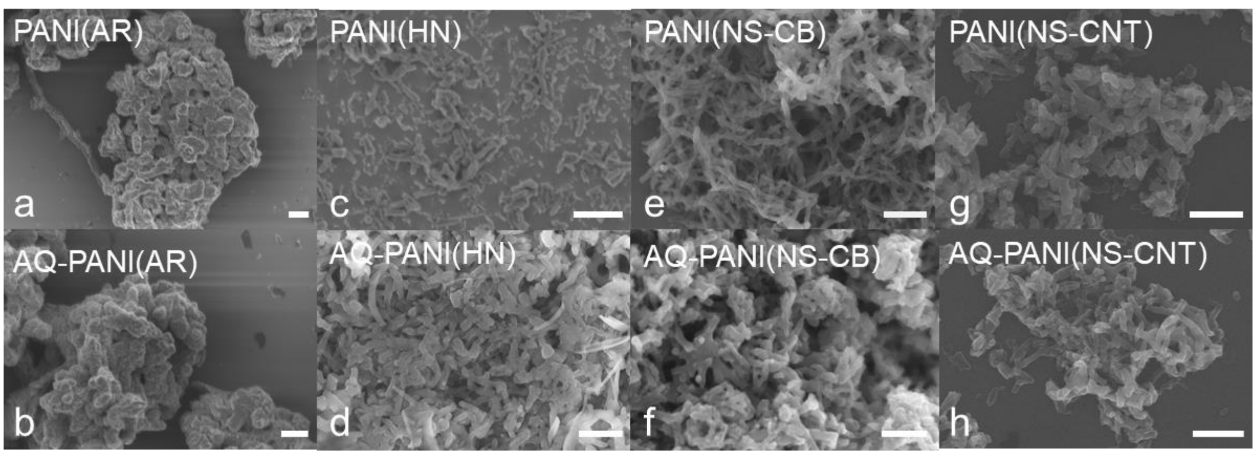

Figure 26. SEM images with polyaniline and AQ-modified polyaniline composites.The white bars at bottom right corner represent the scales of 500 nm.

The successful syntheses of PANI and AQ-modified PANI were verified by FTIR spectra shown in Figure 27. Here we use PANI(NS-CNT) as an example for further discussions (Figure 27a). Transmittance bands at 1552 cm^{-1} (aromatic ring stretching), 1457 cm^{-1} (C=C stretching), 1285 and 1224 cm^{-1} (C-N stretching), were observed for the PANI samples, in agreement with previous reports (black arrows).[32] Comparably, AQ-PANI(NS-CNT) showed increased absorbance (brown arrows) at 1172, 792, and 696 cm^{-1} (C-H bending), which corresponded to

AQ's characteristic peaks.[33] The peak at 1671 cm^{-1} (red arrow), corresponding to peptide bond, further proved the bond formation between amine groups of PANI and carboxylic acid groups of AQ-COOH.[34] The small amount of carbon seeding materials (2.5 wt%) had negligible impacts on FTIR spectra. The attachment of AQ and bond formation onto PANI substrate could be proven for all other materials using the similar analyses as marked in Figure 27b-d.

As only carbon and oxygen atoms were introduced to AQ-PANI composite after attachment of AQ-COOH, elemental analysis of XPS spectra could be used to calculate AQ coverage density in PANI matrices (Figure 28). The chemical formula of green emeraldine salt is written as $(C_6H_7N)_x$, and AQ-2-COOH is $C_{15}H_8O_4$. After amide bond is formed, one hydrogen atom in PANI backbone and one -OH group in AQ-COOH are lost. As PANI contains C, N, O, and H, while AQ only contains C, O, and H, the calculation will be based on the nitrogen balance. We also assume that AQ coverage on PANI surfaces is uniform over the XPS measurement area. Using PANI(RM) as an example, we can first assume AQ-PANI(RM) contains (1-x) mol of PANI and x mol of AQ. According to XPS elemental analysis (Figure 19b), the nitrogen balance can be written as $0.124\times(1-x) = 0.104$, so $x = 0.1613$. The mass coverage of AQ in AQ-PANI(RM) is $0.1613\times(252-17)/((0.1613\times(252-17)+(1-0.1613)\times93-0.1613) = 0.3275$. Therefore, the mol fraction of AQ is 16.13% and mass fraction is 32.75%. Similar calculations can be applied to other samples and the results are summarized in Table 2. All samples contained over 15 mol% and over 30 wt% of molecular AQ co-catalysts, which is the highest AQ loading per unit catalyst mass reported so far (Table 3). This high AQ loading was attributed to both PANI's abundant anchoring sites and PANI's nanostructure with large exposed surface area.

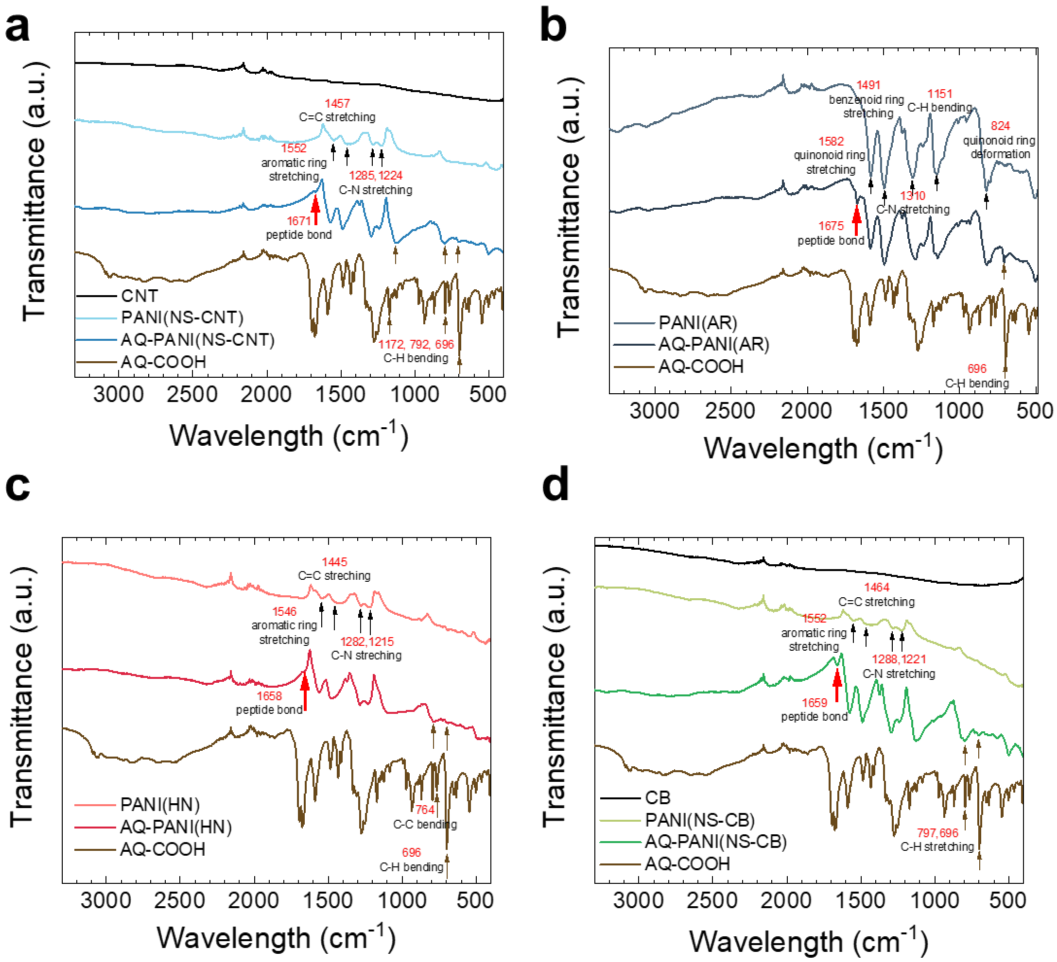

Figure 27. ATR-FTIR spectra of PANI-based material.(a) CNT (black), PANI(NS-CNT) (light blue), AQ-PANI(NS-CNT) (dark blue), AQ-COOH (brown). (b) PANI(AR) (blue), AQ-PANI(AR) (dark blue), AQ-COOH (brown). (c) PANI(HN) (light red), AQ-PANI(HN) (red), AQ-COOH (brown). (d) carbon black (CB) (black), PANI(NS-CB) (light green), AQ-PANI(NS-CB), and AQ-COOH (brown).

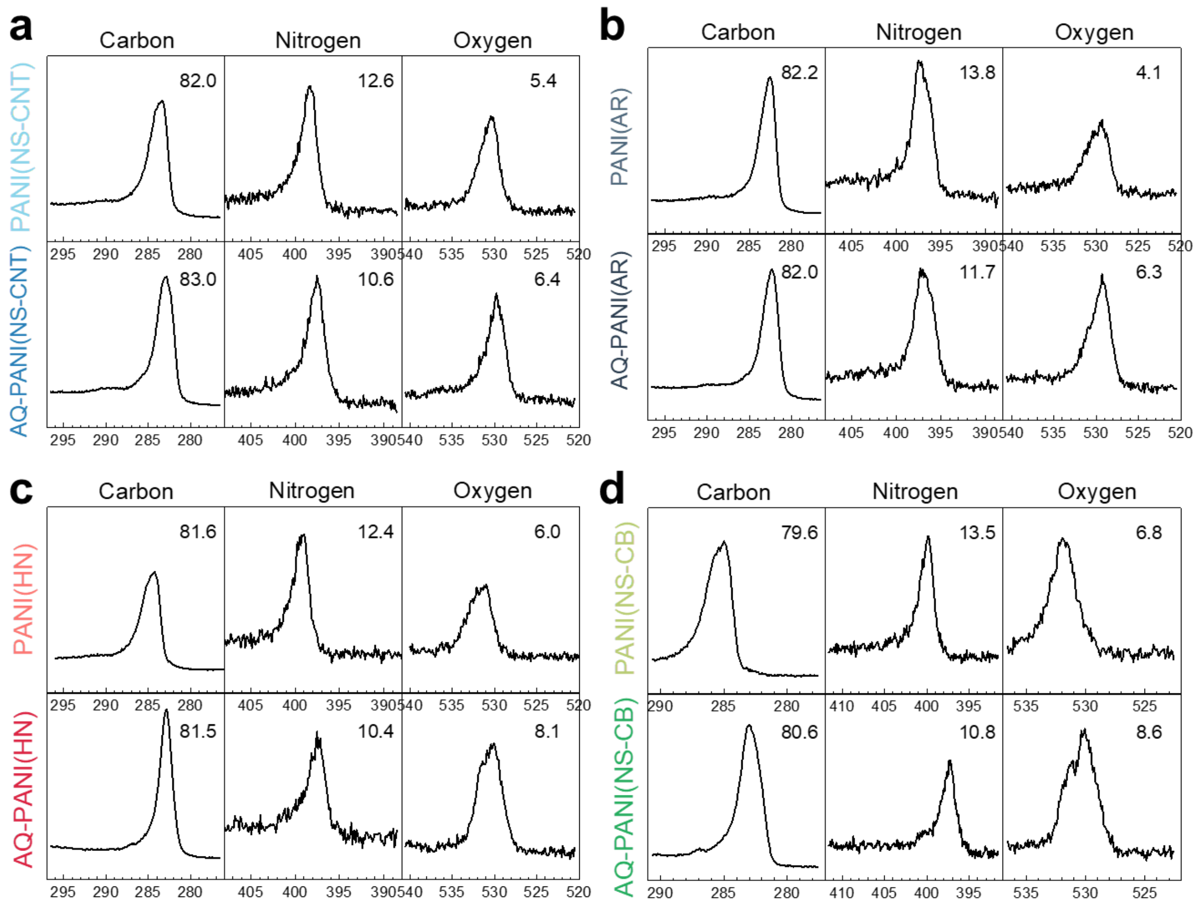

Figure 28. XPS spectra of PANI-based material. For each graph, PANI substrate was presented at the top row and the AQ composite material was presented at the bottom row. Their carbon 1s (first column), nitrogen 1s (second column), and oxygen 1s (third column) core levels were shown respectively. Numbers at the top right corner of each curve represent the atomic percentage of the corresponding element in each material, calculated by integrating peak area. Peak intensities are normalized to the strongest peak.

Table 2. Other properties of PANI-based material. AQ coverage densities represented by molar fraction (2nd column) and weight percentage (3rd column) and double-layer capacitances calculated by CV (4th column) and EIS (5th column) of all samples. All electrodes used in double-layer capacitance measurements had the same loading (0.25 mg cm^{-2}) and geometric area (1 cm^2).

	Molar fraction (%)	Weight percentage (%)	Double-layer capacitance (mF cm^{-2})		
			CV	EIS	average
PANI(AR)	15.22	31.24	0.0064	0.0056	0.0060
AQ-PANI(AR)			0.0189	0.0178	0.0184
PANI(HN)	16.13	32.75	0.0193	0.0176	0.0184

AQ-PANI(HN)			0.0134	0.0140	0.0137
PANI(NS-CB)	20.00	38.78	0.0253	0.0258	0.0255
AQ-PANI(NS-CB)			0.0156	0.0136	0.0146
PANI(NS-CNT)	15.87	32.33	0.0251	0.0265	0.0258
AQ-PANI(NS-CNT)			0.0444	0.0477	0.0461

Table 3. Comparison of 2e- ORR electrocatalysts with anthraquinone or its derivatives

Substrate	H_2O_2 generation rate	Faradaic efficiency (%)	H_2O_2 generation condition		Redox potential ($E_{1/2}$, Vvs. RHE)	AQ coverage density	Binding strategy
			electrolyte	Potential (V. vs. RHE)			
Glassy carbon[9]	N/A	95-100	0.1 M KOH	-0.7 – -1.25	0.17	0.052 – 0.43 nmol cm^{-2}	Covalent attachment of AQ by reducing the AQ diazonium salt
Indium tin oxide[10]	N/A	N/A	N/A	N/A	0.14	40-80 pmol cm^{-2}	π-π interaction between pyrene-bound ITO and pyrene-appended anthraquinone
Graphene oxide[11]	N/A	~80	0.1 M KOH	N/A	0.17	N/A	Covalent attachment of AQ by potentiodynamic electro-reduction of Fast Red Al Salt
Carbon nanotube[12]	0.02 mmol hr^{-1} cm^{-2}	~100	1 M KOH	1.0	0.10	N/A	Drop-cast AQ-2-COOH solution onto carbon paper substrates
Gold disk electrode[35]	N/A	N/A	N/A	N/A	0.20	0.32 nmol cm^{-2}	Self-assembled 1-hydroxy anthraquinone disulfide monolayer on gold disk electrode via incubation
Carbon black[36]	0.52 mmol hr^{-1} cm^{-2}	89.6	0.1 M H_2SO_4 + 0.1 M K_2SO_4	-0.7	0.07	1.0 wt% (up to 3.0 wt%)	Tert-butyl-anthraquinone in suspended solution with carbon black deposited onto disk electrode of RRDE
Polymeric carbon nitride[13]	60.08 mmol $g_{catalyst}^{-1}$ hr^{-1}	42.2	0.5 M phosphate buffer (pH 9)	-0.2	0.27	20 wt%, 377 nmol cm^{-2} (0.5 mg cm^{-2} catalyst)	Chemical bond between C_3N_4 (-NH_2/-NH) and AQ-COOH (-COOH)
Poly-aniline (this work)	1.8 mol $g_{catalyst}^{-1}$ hr^{-1}	95.8	0.1 M phosphate buffer (pH 8.8)	-0.02	0.05	32.33 wt%, 320.5 nmol cm^{-2} (0.25 mg cm^{-2} catalyst)	Chemical bond between polyaniline (-NH) and AQ-COOH (-COOH)

The above morphological differences influenced the double-layer capacitance (C_{DL}) of the electrodes prepared with different PANI samples. The electrocatalytic performance of electrode materials correlates with the amount of active sites that are exposed to the electrolyte.[37-38] Electrochemical surface area (ECSA),[24, 39] defined as the ratio of C_{DL} over specific capacitance (C_S, the capacitance of an atomically smooth planar surface of the material per unit area under identical electrolyte conditions) is a commonly used measure.[24] As disparate values of C_S for PANI were reported in the literature (*e.g.*, due to difficulty of preparing atomically smooth surface made of PANI), we used C_{DL} values, determined using both CV and EIS techniques, to indicate and compare PANI and AQ-PANI matrices. As shown in Table 2, each sample's C_{DL} values measured by CV scans (Figure 29) and EIS showed comparable results as expected. PANI of nanofiber morphologies in general exhibited higher C_{DL} compared with granular PANI due to the larger surface area. The attachment of AQ as pendant groups to polymer chains led to C_{DL} increase for PANI(AR) and PANI(NS-CNT). In contrast, particle aggregations played dominating roles and caused the decrease of C_{DL} for PANI(HN) and PANI(NS-CB). Among all, AQ-PANI(NS-CNT) coated electrode exhibited the largest C_{DL} (0.0461 mF), suggesting the highest electrochemical surface area available for electrocatalytic reactions.

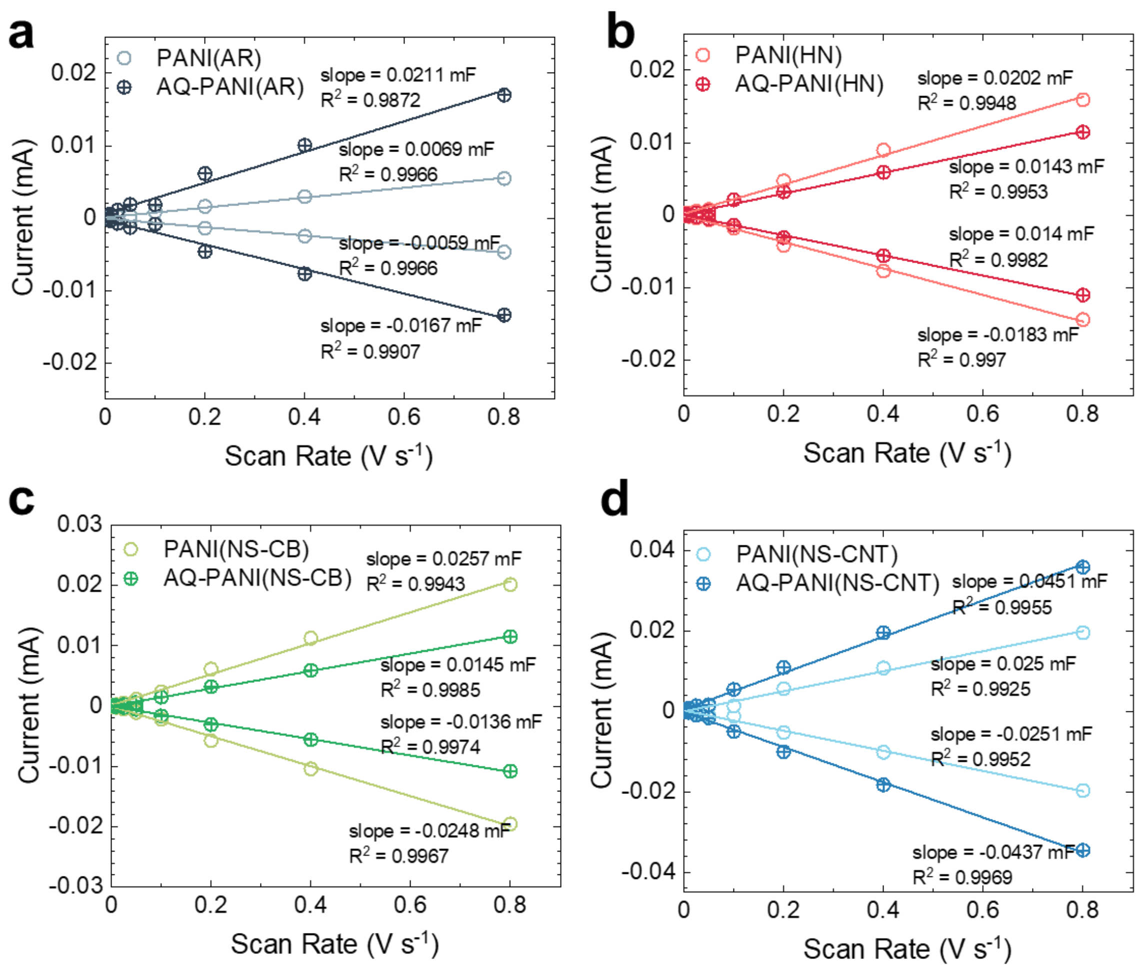

Figure 29. C_{DL} measurements of PANI-based material.The cathodic and anodic charging currents measured at 0 to 0.2 V vs. Ag/AgCl plotted as a function of scan rate for various PANI and AQ-PANI electrodes in 0.1 M phosphate buffer of pH 8.8.

5.4.3 Electrochemical performance in immersed electrode setup

Results in Figure 30 show the capability of PANI and AQ-PANI materials to produce H_2O_2 when deposited onto the cathode and tested in immersed electrochemical cell. Though all of the eight materials had similar Faradaic efficiency of 2 e^- ORR (60.25±8.99%), AQ modification dramatically boosted the overall generation rate: hourly H_2O_2 production increased by 13.56, 1.74, 5.57, 3.49 times for PANI(AR), PANI(HN), PANI(NS-CB), and PANI(NS-CNT) respectively.

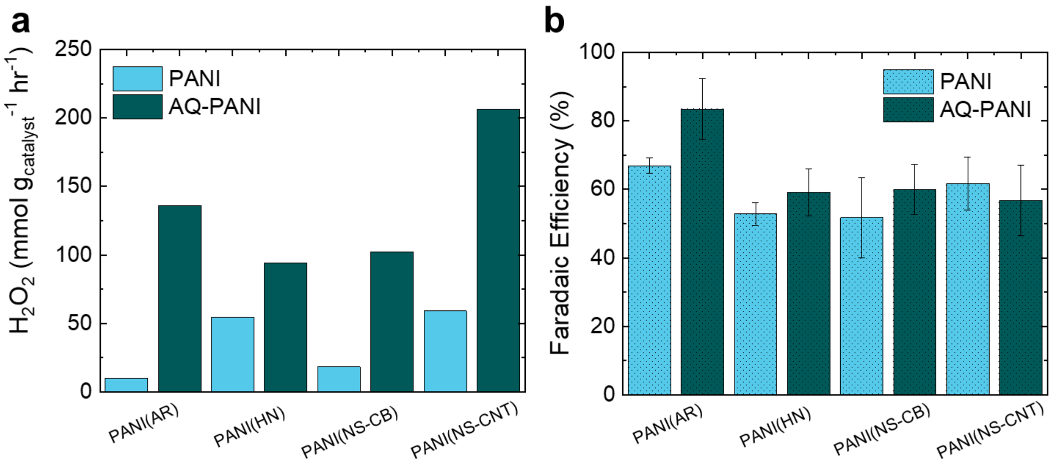

Figure 30. Electrochemical performance of PANI-based material.(a) H_2O_2 generation, and (b) Faradaic efficiency of polyanilines (light blue) and anthraquinone-modified polyanilines (dark green) electrodes at -0.02 V vs. RHE (overpotential = 0.7 V) in 0.1 M phosphate buffer at pH = 8.8. All the electrodes had the same geometric area (1 cm^2) and the same catalyst loading (0.25 mg cm^{-2}). The data points in (a) each represent the mean of two independent measurements. Error bars in (b) were calculated based on two sets of four data points taken during one-hour electrolysis at 15 minutes interval.

Note that PANI produces H_2O_2 even without AQ anchoring, since PANI can catalyze the following sequence of reactions:[40]

$$(PANI)_{ox} + 2nH^+ + 2ne^- \rightarrow (PANI)_{red} \qquad \text{(Equation 17)}$$

$$(PANI)_{red} + nO_2 \rightarrow (PANI)_{ox} + nH_2O_2 \qquad \text{(Equation 18)}$$

As PANI transitions from the reduced to the oxidized form, adsorbed oxygen is reduced via the 2 e^- ORR pathway to form H_2O_2 preferentially instead of the 4 e^- pathway to form water.[41-42] This electron transfer occurs through binding of O_2 to electron-rich aromatic carbons adjacent to nitrogen.[16, 43] AQ produces H_2O_2 via the similar 2 e^- ORR pathway, but with much higher selectivity than PANI (Table 3):

$$AQ + 2H^+ + 2e^- \rightarrow H_2AQ \qquad \text{(Equation 11)}$$

$$H_2AQ + O_2 \rightarrow H_2O_2 + AQ \qquad \text{(Equation 12)}$$

The bond formation between AQ and PANI therefore likely shifted the reaction centers from PANI aromatic carbon to anthraquinone. As evidenced by CV results in Figure 31, though both PANI and AQ showed selectivity toward 2 e- ORR, AQ-modified PANIs were kinetically more favored considering the elevated current densities within Faradaic potential window. The redox peaks at -0.1 V to -0.2 V vs. RHE corresponds to the redox activity of AQ molecules in the composite materials. Similar to the experimental observations in Chapter 4.4.2, the reduction peaks of AQ-PANI composites are more obvious than the oxidation peaks, and in many cases the oxidation peaks are not expressed due to the fast chemical reaction between O_2 and H_2AQ.

Notably, AQ-PANI(NS-CNT) showed the highest H_2O_2 generation rate (206.4 mmol $g_{catalyst}^{-1}$ hr^{-1}) and comparable selectivity (56.75±10.39%) probably due to its largest electrochemical surface area. Therefore, AQ-PANI(NS-CNT) will be further tested in gas diffusion electrode cell as discussed in Chapter 6.

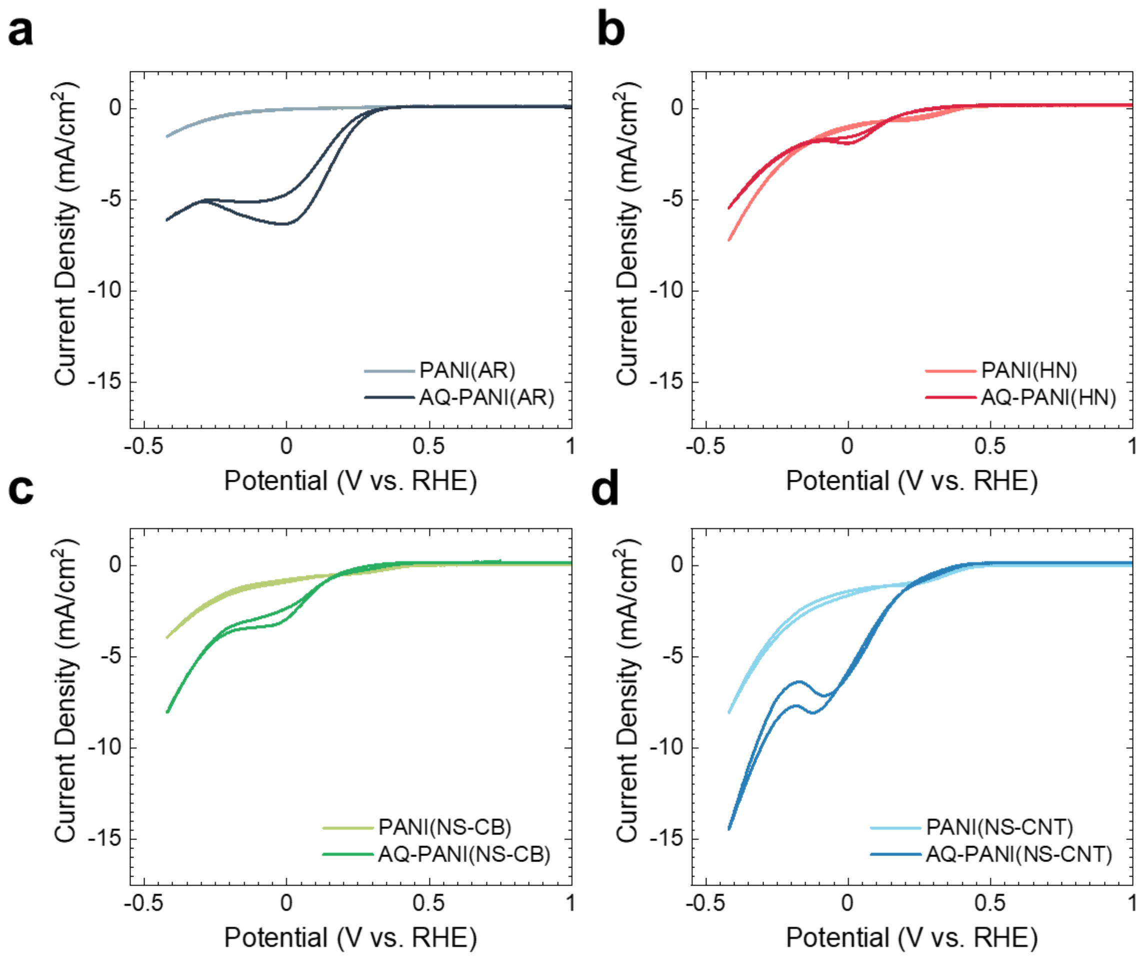

Figure 31. Cyclic voltammetry graphs of PANI-based material. PANI and AQ-PANI electrodes were tested at immersed electrode setup in 0.1 M pH = 9 phosphate buffer purged with O_2. All the electrodes had the same geometric area (1 cm^2) and the same catalyst loading (0.25 mg cm^{-2}).

5.4.4 Polyaniline synthesized via electropolymerization

In addition to the previously discussed polyaniline synthesis methods, electro-polymerization was also explored as a potential pathway to manufacture an electrocatalytic PANI substrate. As carbon paper, the current collector, was soaked in a solution with the monomer aniline, we expected that the carbon fibers would function as nucleation cores and the polymer growth will mimic the morphology of the carbon paper. As described in Chapter 5.3.1, the initial cycle activated a large number of aniline cation radicals on electrode surface, necessary to initiate the oligomeric formation and polymer growth.[23] We supposed that instead of loosely attaching to carbon paper via weak molecular interactions such as Van der Waals forces, catalyst synthesized via electropolymerization would be chemically bond with the substrate and have larger electrochemical surface area, and thus have faster electron transfer and oxygen reduction reaction rate.[44]

However, the electrochemical performance of electro-polymerized PANI (PANI(EP)) and the anthraquinone-modified composite (AQ-PANI(EP)) is not quite as expected. Similar to those discussed in Chapter 5.4.3, AQ modification to PANI(EP) could be manifested by the reduction peak at around 0 V vs. RHE (Figure 32c) and it did improve the H_2O_2 generation rate per unit mass of catalyst (15.4 to 28.4 mmol $g_{catalyst}^{-1}$ hr^{-1}, Figure 32a) and the Faradaic efficiency (49.9% to 65.5%, Figure 32b) over the one-hour period, while the overall generation rate are much slower (i.e., AQ-PANI(EP)'s H_2O_2 generation rate (28.4 mmol $g_{catalyst}^{-1}$ hr^{-1}) is only 14% of AQ-PANI(NS-CNT)'s H_2O_2 generation rate (206.4 mmol $g_{catalyst}^{-1}$ hr^{-1})). This frustrating observation could be due to the following two reasons: 1) the possible measurement error of the catalyst mass, 2) the ineffective exposure of polymer.

Contrary to the electrode made by drop-casting, where catalyst mass can be easily calculated based on the catalyst concentration in the suspension and the volume of suspension drop-casted onto the electrode surface, electrode made by electropolymerization was measured before and after the polymer growth process to calculate the mass increase. The latter method, although seemed rather simple and straightforward, was greatly limited by the precision of the balance. In Figure 32, the measured catalyst mass of PANI(EP) was 1.1 mg, and the mass of AQ-PANI(EP) was 2.2 mg; both numbers are quite close to the balance's accuracy of 4 decimal places. The mass loss or gain related to drying process and moisture adsorption to electrode surface could make this problem even more complicated. The minor errors introduced by the measurement could lead to significant deviations in the generation rate per unit mass, and make the comparison between different synthesis methods impossible. What's more, the previous material characterization method used to quantify the AQ coverage density (based on XPS elemental analysis) would be no longer applicable to the PANI synthesized directly on electrode surface due to the extensive impact from the carbon substrate: PANI's carbon 1s core level spectra would be largely interfered by the carbon atoms in both the carbon fiber and the Polytetrafluoroethylene (PTFE) coating and it was quite challenging for deconvolution. A more sophisticated method of quantifying anthraquinone molecules on the surface became crucial for identifying the optimized synthesis as well as the electrochemical performance.

Another likely explanation is that the electrode was inundated with the polymer chains and thus not all the probable active sites were fully exposed to be electrochemically active. To better understand the reasons behind the rather poor performance of electro-polymerized PANI-based electrocatalysts, the cross-sectional SEM images would be necessary to examine the morphology and structure from the diffusion layer to the catalyst layer and if the PANI layer grew too thick to block each other . The relationship between the number of CV cycles, catalyst layer thickness, electrochemically active surface area, and H_2O_2 generation rate needed to be more carefully investigated to maximize the production capability per unit mass of catalyst. The potential windows of both the initial and the following CV programs could be adjusted based on the oxidation and reduction state of PANIs and their electrochemical performance. A more precise way of measuring the catalyst mass, such as a balance with higher precision and a quartz crystal microbalance, would be preferred as well.

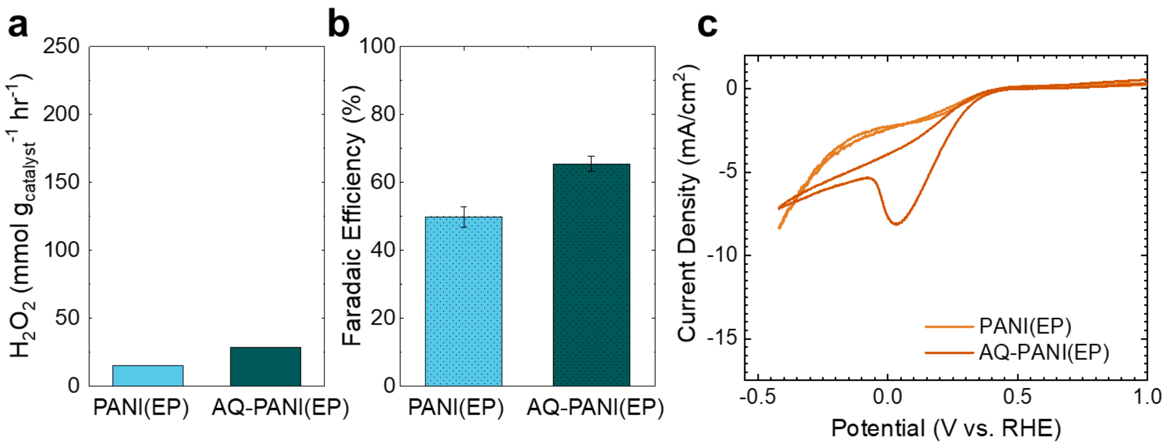

Figure 32. Electrochemical performance of electro-polymerized PANI-based material. (a) H_2O_2 generation, and (b) Faradaic efficiency of PANI(EP) (light blue) and AQ-PANI(EP) (dark green) electrodes at -0.02 V vs. RHE (overpotential = 0.7 V) in 0.1 M phosphate buffer at pH = 8.8. All the electrodes had the same geometric area (1 cm^2) and the same catalyst loading (0.25 mg cm^{-2}). The data points in (a) each represent the mean of two independent measurements. Error bars in (b) were calculated based on two sets of four data points taken during one-hour electrolysis at 15 minutes interval. (c) Cyclic voltammetry graphs of PANI(EP) (light orange) and AQ-PANI(EP) (dark orange) electrodes at immersed electrode setup in 0.1 M pH = 9 phosphate buffer purged with O_2.

5.5 Conclusion

In this chapter, a series of anthraquinone-polyaniline composite electrocatalysts were synthesized and examine for their electrochemical behavior. The high activity and efficiency were achieved because polyaniline substrate provided abundant anchoring sites in its backbone for co-catalyst anthraquinone's attachment. FTIR-ATR spectra proved the successful peptide formation between the co-catalyst and the catalytic substrate and thus the successful covalent attachment, and XPS spectra proved the similar AQ coverage density (of over 30 wt%) regardless of the synthesis pathways and morphologies of the substrates. While double layer capacitances calculated from EIS and CV data showed how significantly the poor dispersion of solids during synthesis could affect the electrochemical active surface areas of the electrocatalysts.

Although PANI substrates can reduce oxygen to produce H_2O_2 with some selectivity (50%-60%), AQ attachment can dramatically improve the overall H_2O_2 electrochemical generation rate regardless of the type of the PANI substrate, as oxygen reduction reaction over AQ-PANIs are kinetically more favored. For future research, a PANI substrate with even larger electrochemical active surface area and better dispersity in organic solvents necessary for AQ attachment will be preferred.

The attempts to synthesize PANI via electropolymerization faced a few challenges, possibly due to inaccurate measure of the catalyst mass and over-growth of the polymer. A few potential solutions were proposed to improve the overall electrocatalytic performance, including cross-sectional SEM examination, experimental condition optimization, and precise measurement utilization.

5.6 References

1. Tepong-Tsindé, R.; Crane, R.; Noubactep, C.; Nassi, A.; Ruppert, H. Testing Metallic Iron Filtration Systems for Decentralized Water Treatment at Pilot Scale. *Water* **2015,** *7* (3).

2. Garrido-Baserba, M.; Vinardell, S.; Molinos-Senante, M.; Rosso, D.; Poch, M. The Economics of Wastewater Treatment Decentralization: A Techno-economic Evaluation. *Environ Sci Technol* **2018,** *52* (15), 8965-8976.

3. Massoud, M. A.; Tarhini, A.; Nasr, J. A. Decentralized approaches to wastewater treatment and management: Applicability in developing countries. *Journal of Environmental Management* **2009,** *90* (1), 652-659.

4. Peter-Varbanets, M.; Gujer, W.; Pronk, W. Intermittent operation of ultra-low pressure ultrafiltration for decentralized drinking water treatment. *Water Res* **2012,** *46* (10), 3272-3282.

5. Oturan, M. A.; Aaron, J.-J. Advanced Oxidation Processes in Water/Wastewater Treatment: Principles and Applications. A Review. *Critical Reviews in Environmental Science and Technology* **2014,** *44* (23), 2577-2641.

6. Hodges, B. C.; Cates, E. L.; Kim, J.-H. Challenges and prospects of advanced oxidation water treatment processes using catalytic nanomaterials. *Nature Nanotechnology* **2018,** *13* (8), 642-650.

7. Hâncu, D.; Green, J.; Beckman, E. J. H_2O_2 in CO_2/H_2O Biphasic Systems: Green Synthesis and Epoxidation Reactions. *Industrial & Engineering Chemistry Research* **2002,** *41* (18), 4466-4474.

8. Xia, C.; Xia, Y.; Zhu, P.; Fan, L.; Wang, H. Direct electrosynthesis of pure aqueous H_2O_2 solutions up to 20% by weight using a solid electrolyte. *Science* **2019,** *366* (6462), 226.

9. Sarapuu, A.; Vaik, K.; Schiffrin, D. J.; Tammeveski, K. Electrochemical reduction of oxygen on anthraquinone-modified glassy carbon electrodes in alkaline solution. *Journal of Electroanalytical Chemistry* **2003,** *541*, 23-29.

10. Hanna, C. M.; Luu, A.; Yang, J. Y. Proton-Coupled Electron Transfer at Anthraquinone Modified Indium Tin Oxide Electrodes. *ACS Applied Energy Materials* **2019,** *2* (1), 59-65.

11. Zhang, G. Q.; Zhou, Y. F.; Chen, J.; Yang, F. L. Potentiostatic-Potentiodynamic Reduction Synthesis of Anthraquinone Functionalized Graphene for Oxygen Reduction in Alkaline Medium. *International Journal of Electrochemical Science* **2012,** *7* (11), 11323-11337.

12. Jeon, T. H.; Kim, H.; Kim, H.-i.; Choi, W. Highly durable photoelectrochemical H_2O_2 production via dual photoanode and cathode processes under solar simulating and external bias-free conditions. *Energy & Environmental Science* **2020,** *13* (6), 1730-1742.

13. Zhu, Q.; Pan, Z.; Hu, S.; Kim, J.-H. Cathodic Hydrogen Peroxide Electrosynthesis Using Anthraquinone Modified Carbon Nitride on Gas Diffusion Electrode. *ACS Applied Energy Materials* **2019,** *2* (11), 7972-7979.

14. Fusalba, F.; Gouérec, P.; Villers, D.; Bélanger, D. Electrochemical characterization of polyaniline in nonaqueous electrolyte and its evaluation as electrode material for electrochemical supercapacitors. *Journal of the Electrochemical Society* **2001,** *148* (1), A1.

15. Meng, Q.; Cai, K.; Chen, Y.; Chen, L. Research progress on conducting polymer based supercapacitor electrode materials. *Nano Energy* **2017,** *36*, 268-285.

16. Wang, H.; Lin, J.; Shen, Z. X. Polyaniline (PANi) based electrode materials for energy storage and conversion. *Journal of Science: Advanced Materials and Devices* **2016,** *1* (3), 225-255.

17. Boeva, Z. A.; Sergeyev, V. G. Polyaniline: Synthesis, properties, and application. *Polymer Science Series C* **2014,** *56* (1), 144-153.

18. Bhadra, S.; Khastgir, D.; Singha, N. K.; Lee, J. H. Progress in preparation, processing and applications of polyaniline. *Progress in Polymer Science* **2009,** *34* (8), 783-810.

19. Kang, E. T.; Neoh, K. G.; Tan, T. C.; Khor, S. H.; Tan, K. L. Structural studies of poly (p-phenyleneamine) and its oxidation. *Macromolecules* **1990,** *23* (11), 2918-2926.

20. Li, D.; Kaner, R. B. Shape and Aggregation Control of Nanoparticles: Not Shaken, Not Stirred. *Journal of the American Chemical Society* **2006,** *128* (3), 968-975.

21. Zhang, X.; Goux, W. J.; Manohar, S. K. Synthesis of Polyaniline Nanofibers by "Nanofiber Seeding". *Journal of the American Chemical Society* **2004,** *126* (14), 4502-4503.

22. Valeur, E.; Bradley, M. Amide Bond Formation: Beyond the Myth of Coupling Reagents. *Chemical Society Reviews* **2009,** *38* (2), 606-631.

23. Dalmolin, C.; Canobre, S. C.; Biaggio, S. R.; Rocha-Filho, R. C.; Bocchi, N. Electropolymerization of polyaniline on high surface area carbon substrates. *Journal of Electroanalytical Chemistry* **2005,** *578* (1), 9-15.

24. McCrory, C. C. L.; Jung, S.; Peters, J. C.; Jaramillo, T. F. Benchmarking Heterogeneous Electrocatalysts for the Oxygen Evolution Reaction. *Journal of the American Chemical Society* **2013,** *135* (45), 16977-16987.

25. Hatchett, D. W.; Josowicz, M.; Janata, J. Comparison of Chemically and Electrochemically Synthesized Polyaniline Films. *Journal of the Electrochemical Society* **1999,** *146* (12), 4535-4538.

26. Huang, J.; Kaner, R. B. A General Chemical Route to Polyaniline Nanofibers. *Journal of the American Chemical Society* **2004,** *126* (3), 851-855.

27. Masters, J. G.; Sun, Y.; MacDiarmid, A. G.; Epstein, A. J. Polyaniline: Allowed oxidation states. *Synthetic Metals* **1991,** *41* (1), 715-718.

28. Silva, C. H. B.; Galiote, N. A.; Huguenin, F.; Teixeira-Neto, É.; Constantino, V. R. L.; Temperini, M. L. A. Spectroscopic, morphological and electrochromic characterization of layer-by-layer hybrid films of polyaniline and hexaniobate nanoscrolls. *Journal of Materials Chemistry* **2012,** *22* (28), 14052-14060.

29. Kolla, H. S.; Surwade, S. P.; Zhang, X.; MacDiarmid, A. G.; Manohar, S. K. Absolute Molecular Weight of Polyaniline. *Journal of the American Chemical Society* **2005,** *127* (48), 16770-16771.

30. Zhang, H.; Cao, G.; Wang, W.; Yuan, K.; Xu, B.; Zhang, W.; Cheng, J.; Yang, Y. Influence of microstructure on the capacitive performance of polyaniline/carbon nanotube array composite electrodes. *Electrochimica Acta* **2009,** *54* (4), 1153-1159.

31. Kim, K.-S.; Park, S.-J. Influence of multi-walled carbon nanotubes on the electrochemical performance of graphene nanocomposites for supercapacitor electrodes. *Electrochimica Acta* **2011,** *56* (3), 1629-1635.

32. Miroslava, T.; Jaroslav, S. Polyaniline: The infrared spectroscopy of conducting polymer nanotubes (IUPAC Technical Report). *Pure and Applied Chemistry* **2011,** *83* (10), 1803-1817.

33. Higo, M.; Miake, T.; Mitsushio, M.; Yoshidome, T.; Ozono, Y. Adsorption State and Morphology of Anthraquinone-2-carboxylic Acid Deposited from Solution onto the Atomically-Smooth Native Oxide Surface of Al(111) Films Studied by Infrared Reflection Absorption Spectroscopy, X-ray Photoelectron Spectroscopy, and Atomic Force Microscopy. *Analytical Sciences* **2008,** *24* (3), 313-320.

34. Barth, A. Infrared spectroscopy of proteins. *Biochimica et Biophysica Acta (BBA) - Bioenergetics* **2007,** *1767* (9), 1073-1101.

35. Abhayawardhana, A. D.; Sutherland, T. C. Heterogeneous proton-coupled electron transfer of a hydroxy-anthraquinone self-assembled monolayer. *Journal of Electroanalytical Chemistry* **2011,** *653* (1), 50-55.

36. Valim, R. B.; Reis, R. M.; Castro, P. S.; Lima, A. S.; Rocha, R. S.; Bertotti, M.; Lanza, M. R. V. Electrogeneration of hydrogen peroxide in gas diffusion electrodes modified with tert-butyl-anthraquinone on carbon black support. *Carbon* **2013,** *61*, 236-244.

37. Luo, X.; Li, Z.; Luo, M.; Guo, C.; Sun, L.; Lan, S.; Luo, R.; Huang, L.; Qin, Y.; Luo, Z. Boosting the primary Zn–air battery oxygen reduction performance with mesopore-dominated semi-tubular doped-carbon nanostructures. *Journal of Materials Chemistry A* **2020,** *8* (19), 9832-9842.

38. Jadhav, H. S.; Roy, A.; Desalegan, B. Z.; Seo, J. G. An advanced and highly efficient Ce assisted NiFe-LDH electrocatalyst for overall water splitting. *Sustainable Energy & Fuels* **2020,** *4* (1), 312-323.

39. Paula, C.; Jona, S.; Bernhard, K.; Wolfram, J. The Determination of Electrochemical Active Surface Area and Specific Capacity Revisited for the System MnOx as an Oxygen Evolution Catalyst. *Zeitschrift für Physikalische Chemie* **2020,** *234* (5), 979-994.

40. El Hourch, A.; Belcadi, S.; Moisy, P.; Crouigneau, P.; Léger, J. M.; Lamy, C. Electrocatalytic reduction of oxygen at iron phthalocyanine modified polymer electrodes. *Journal of Electroanalytical Chemistry* **1992,** *339* (1), 1-12.

41. Doubova, L.; Mengoli, G.; Musiani, M. M.; Valcher, S. Polyaniline as a cathode for O2 reduction—Kinetics of the reaction with H2O2 and use of the polymer in a model H2O2 fuel cell. *Electrochimica Acta* **1989,** *34* (3), 337-343.

42. Mengoli, G.; Musiani, M. M.; Zotti, G.; Valcher, S. Potentiometric investigation of the kinetics of the polyaniline—oxygen reaction. *Journal of Electroanalytical Chemistry and Interfacial Electrochemistry* **1986,** *202* (1), 217-230.

43. Khomenko, V.; Barsukov, V.; Katashinskii, A. The catalytic activity of conducting polymers toward oxygen reduction. *Electrochimica Acta* **2005,** *50* (7-8), 1675-1683.

44. Song, F.; Li, W.; Han, G.; Sun, Y. Electropolymerization of Aniline on Nickel-Based Electrocatalysts Substantially Enhances Their Performance for Hydrogen Evolution. *ACS Applied Energy Materials* **2018,** *1* (1), 3-8.

Chapter 6: Gas Diffusion Electrode Cell with Anthraquinone-Based Electrocatalysts

This Chapter is published (adapted):

Zhu, Q.; Pan, Z.; Hu, S.; Kim, J.-H. Cathodic Hydrogen Peroxide Electrosynthesis Using Anthraquinone Modified Carbon Nitride on Gas Diffusion Electrode. *ACS Applied Energy Materials* **2019**, *2* (11), 7972-7979.

Zhu, Q.; Hinkle, M.; Kim, D. J.; Kim, J.-H. Modular Hydrogen Peroxide Electrosynthesis Cell with Anthraquinone-Modified Polyaniline Electrocatalyst. *ACS ES&T Engineering* **2021,** *1* (3), 446-455.

6.1 Abstract

As Chapter 4 and 5 discussed in detail of the heterogeneous electrocatalysts based on anthraquinone chemistry, this chapter will focus on the next step towards application: making electrocatalysts into more efficient electrodes with more efficient reactor designs. In this chapter, both materials, AQ-C_3N_4 and AQ-PANI, were made into gas diffusion electrodes and tested with two generations of gas diffusion electrode cells, where mass transport of oxygen reactants will be enhanced, as well as the H_2O_2 generation rate and Faradaic efficiency. AQ–C_3N_4 were tested in a batch reactor setup, and its GDE counterpart produced 4.3 times H_2O_2 (60.1 mmol $g_{catalyst}^{-1}$) at higher Faradaic efficiency (42.2 ±1.3%) than the AQ–C_3N_4 IE (14.0 mmol $g_{catalyst}^{-1}$ and 31.0% FE). In a flow cell equipped with AQ-PANI gas diffusion cathode, H_2O_2 can be produced at a rate of 1.80 mol $g_{catalyst}^{-1}$ at 100 mA with Faradaic efficiency of 95.83%. The calculation proved

that H_2O_2 generation cell consumes only 0.2 to 20% of the total electricity consumption of AOPs in various AOP application scenarios employing UV activation. We also examined the H_2O_2 production capability of the device with simulated drinking water and wastewater as feed electrolytes to demonstrate its potential for real-world operation scenarios.

6.2 Introduction

An effective and applicable hydrogen peroxide electrosynthesis cell requires more than the design and synthesis of electrocatalyst; an effective electrode architecture and the respective electrochemical cell design to overcome the challenges, especially those associated with oxygen-transport limitation. As described by Equation 2, three reactants are required in the electrosynthesis process: oxygen, proton, and electron.

$$O_2 + 2H^+ + 2e^- \rightarrow H_2O_2 \text{ (0.68 V vs. RHE)} \qquad \text{(Equation 2)}$$

As protons are abundant in an aqueous system and conveniently generated via self-ionization of water, and electrons supplied by an potential bias toward the electrode surface, dioxygen molecules become the limiting reactant in the process due to its low solubility and slow transport kinetics in water. At 25 °C and 1 atm, the dissolved oxygen concentration in freshwater is 8-9 mg/L,[1] and oxygen's diffusion coefficient in water is 2.42×10^{-5} cm^2 s^{-1},[2] which is about 10^4 times smaller than its diffusion coefficient in air.[3] Although rapidly stirring the electrolyte could significantly improve the oxygen mass transport via convection, a concentration gradient over the electrode surface is unavoidable with the diffusion layer formation.[4]

To minimize the overpotential build-up and thus cell performance impairment, we employ a gas diffusion electrode (GDE) for sustained H_2O_2 production rates without oxygen-transport limitation at the electrode surface.[5-7] Instead of a traditional immersed electrode (IE) where the electrode is fully immersed in gas-bubbled electrolyte, the gas diffusion electrode is generally made of PTFE-coated carbon fibers and is composed of two layers: one hydrophobic layer facing the gas phase and one more hydrophilic layer, coated with catalyst, facing the liquid phase. The electrochemical reaction will then involve three phases: gas phase (oxygen), liquid phase (water), and solid phase (catalyst), and therefore this thin layer will be described by "triple-phase boundary layer".[8] In GDE, oxygen gas molecules no longer transports in aqueous phase; instead, they can transport through the hydrophobic layer directly toward the solid/liquid/gas interface at the electrode surface. This process significantly improves the surface oxygen concentration and thus oxygen reduction reaction rate and H_2O_2 generation rate.

We further fabricated two generations of prototype H_2O_2 production cells with gas diffusion architecture and evaluated their performance. The first generation cell incorporating C_3N_4-based material as electrocatalysts was a batch reactor, while the second generation cell incorporating PANI-based material as electrocatalysts could be operated as a flow cell. The second cell was also tested in various water matrices (phosphate buffer electrolyte, simulated wastewater, simulated drinking water) and gas systems (ultrapure O_2, air) to illustrate its applicability in realistic conditions. We further discussed the proportion of energy consumption for H_2O_2 generation in the overall AOP energy requirement and presented strategies to integrate this cell to AOP application.

6.3 Experimental Methods

6.3.1 Electrode preparation

Electrocatalysts were prepared as described in Chapter 4 and 5. Two types of electrodes (IEs and GDEs) were prepared following the procedure outlined in Figure 33. Briefly, for IE and "GDE batch", the electrode used in first generation batch reactor, a suspension of catalysts (1 mg mL^{-1}) in 50/50 (v/v) water/isopropanol mixture was slowly and uniformly drop-casted onto carbon paper (Toray Paper 120, Fisher) to achieve a porous nanocrystalline film with the catalyst loading of 0.5 mg cm^{-2}. The electrode was then dried at room temperature in air for 2 hours and annealed at 80 °C in air for 15 hours. To make GDEs, a strip of copper tape (i.e., highly conductive copper electrical tape with conductive adhesive, McMaster-Carr) was attached to the end of carbon paper. To make IEs, a piece of tin-plated Cu wire was first coiled at one end, attached to the edge of carbon paper, and glued with silver conductive paste (503, Electron Microscopy Sciences), while the other end of Cu wire was threaded through a glass tube. The electrode was capsulated and sealed with epoxy adhesive (Hysol 9460F, Loctite) to prevent copper electro-corrosion and to ensure that only loaded catalysts and carbon paper contact electrolytes. Both IE and "GDE batch", the exposed geometric areas of the electrodes are 1 cm^2. For "GDE flow", 500 mL of catalyst suspension with concentration of 2 mg mL^{-1} in 25/75 (v/v) water/isopropanol mixture was slowly and uniformly drop-casted onto a piece of carbon paper (Sigracet 39 BB, SGL Carbon, 2.5 cm×2.5 cm). The exposed geometric area of the electrode was 4 cm^2 (2 cm×2 cm) and the catalyst loading was 0.25 mg cm^{-2}.

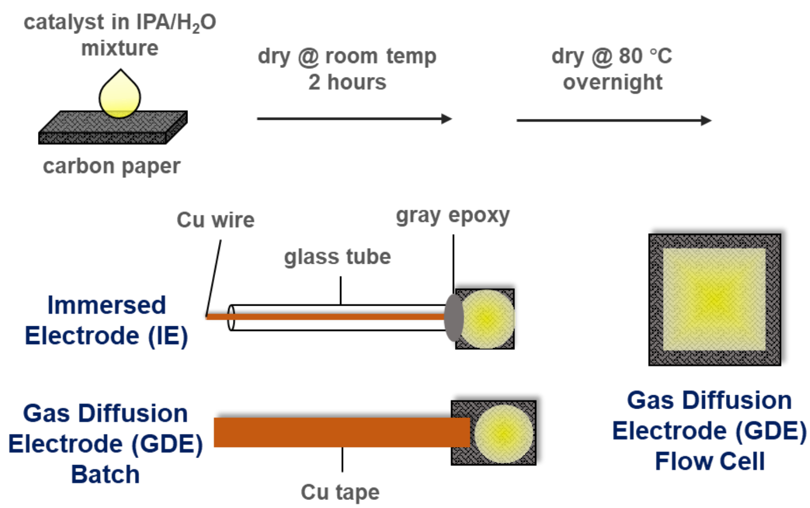

Figure 33. Schematic of electrode preparations for immersed electrode and gas diffusion electrodes.

6.3.2 Electrochemical cell

For both immersed electrode setup and the first generation batch reactor setup, a carbon rod (VWR) was used as the counter electrode, and an Ag/AgCl electrode filled with saturated KCl solution (CHI111, CH Instruments) was used as the reference electrode. For the second generation flow cell setup, a titanium mesh (Goodfellow) coated with iridium oxide was used as the counter electrode and the cell was operated in a two-electrode system. Both working and counter electrodes have sizes of 4 cm^2 (2 cm × 2 cm); water channel has size of 4 cm^2 and depth of 1.5 mm. A miniature peristaltic pump (Instech P625) was used to control the liquid flow rate (0.25–2 mL min^{-1}), and a mass flow controller (Alicat) was used to control the gas flow rate (10 sccm (standard cubic centimeter per minute) for O_2, 50 sccm for air). Air was supplied by an air generator (747-30, Aadco Instruments). Water conductivities were measured by a conductivity meter (CON 2700, Oakton). Other conditions are the same as Chapter 4.3.4 and Chapter 5.3.3.

6.3.3 Surface hydrophobicity measurement

The surface hydrophobicity of electrodes was evaluated by measuring the contact angle of a water droplet using the sessile drop method. A 1 μL droplet was placed on the air-dried electrode surface and photographed with a digital camera. The contact angles of the left and right sides of the droplet were determined using a computer program (VCA, Optima XE, AST Products, Billerica, MA). To account for variations in the measurements, 30 measurements were taken.

6.4 Results and Discussion

6.4.1 AQ-C_3N_4 electrocatalysts: IE vs. GDE

Low solubility of O_2 in water and slow diffusive mass transport across the boundary layer are known to cause gradual O_2 depletion on the electrode surface, thus limiting ORR reactions.[9-10] In order to overcome this prevalent challenge of traditional IE design, an alternative GDE setup was explored (Figure 34 left panel,) and tested with AQ-C_3N_4 electrocatalysts. In this GDE configuration, a side of carbon fiber paper is exposed to the ambient air and kept dry, as the carbon fibers are coated with wet-proofing Teflon layer at 1% wt (Figure 36).[11] This GDE-gas interfacial region, so called the gas diffusion layer, provides a conduit for gas-phase O_2 supply. The opposite side of the carbon fiber paper hosts AQ–C_3N_4 and is in contact with the electrolyte. Due to the hydrophilicity of the coated catalysts, this region becomes partially wet and forms a catalyst/electrolyte/gas triple-phase boundary layer enriched with O_2 (red box in Figure 34 middle).[12-13] During the operation, H_2AQ is formed at the catalyst/electrolyte interface by receiving electrons from conductive C_3N_4 network deposited on carbon paper and by reacting with protons from electrolytes, as indicated in Reaction 3 and illustrated by Figure 34 (right top, charge transfer). H_2AQ then reduces O_2 (Equation 12) to produce H_2O_2 at the gas/catalyst interface (Figure 34 right middle, catalysis). Finally, the produced H_2O_2 diffuses to the bulk electrolyte (Figure 34 right bottom, H_2O_2 diffusion).

$$AQ + 2\,H^+ + 2\,e^- \rightleftharpoons H_2AQ \text{ (0.27 V vs. RHE)} \qquad \text{(Equation 11)}$$

$$O_2 + H_2AQ \rightarrow AQ + H_2O_2 \qquad \text{(Equation 12)}$$

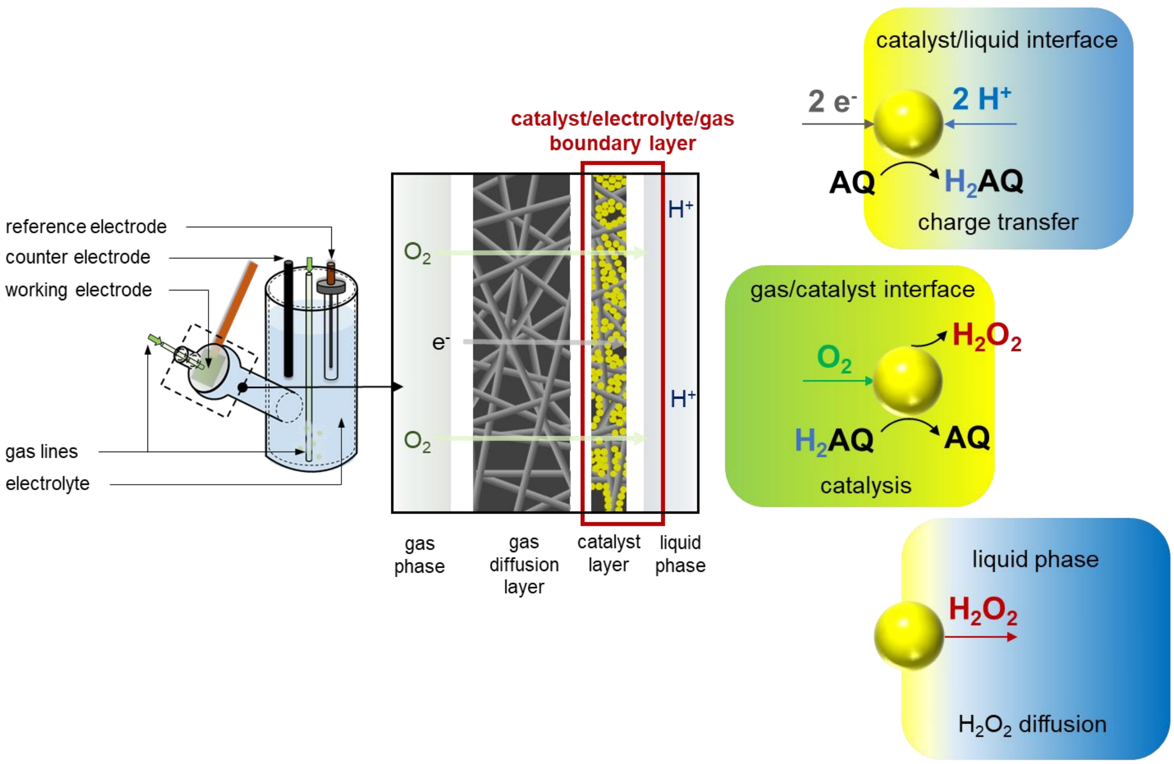

Figure 34. Schematics of a gas diffusion electrode loaded with C_3N_4-supported catalysts for oxygen reduction to hydrogen peroxide Left: GDE reactor. Middle: enlarged components of the triple-phase boundary layer. Right: three steps (charge transfer, catalysis, H_2O_2 diffusion) at different interfaces and phases during the reaction process.

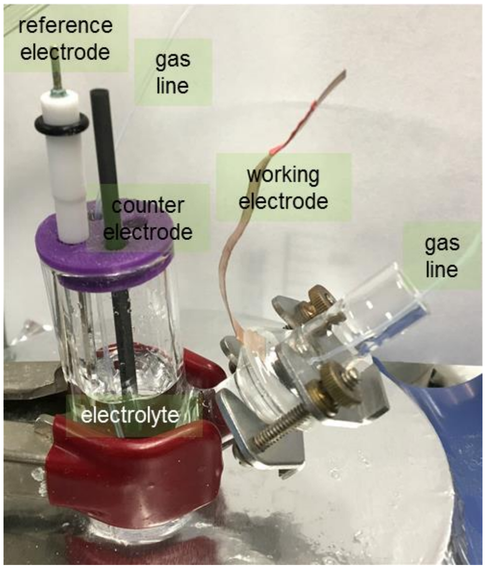

Figure 35. Schematic illustration of the first generation batch reactor.Credit: Qianhong Zhu.

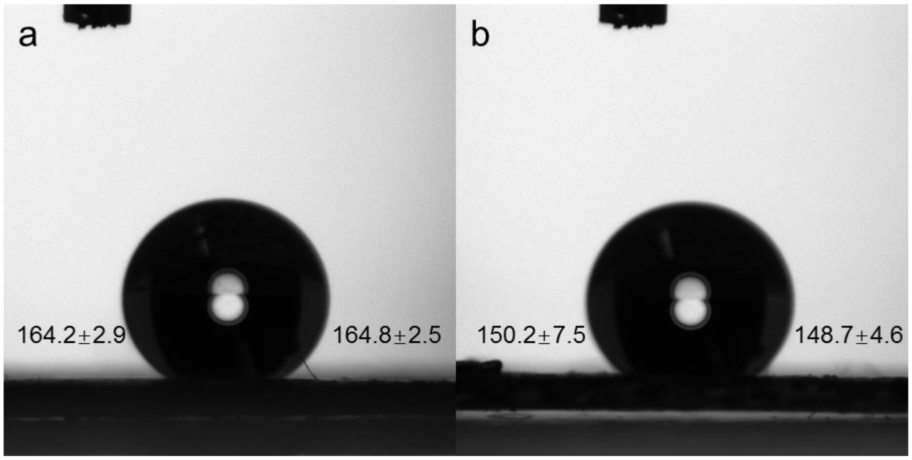

Figure 36. Contact angle measurements of electrode surface. A sessile water droplet (1 μL) on Toray 120 carbon paper: a) before experiment, b) after 10 hours of electrolysis. The values reported are averages of 30 measurements in 10 seconds.

As shown in Figure 37, the GDE setup achieved a much higher current density than the IE setup within the electrochemical window. The AQ–C_3N_4 GDE exhibited 6.9 times larger reduction current density (-7.00 mA cm^{-2}) than the AQ–C_3N_4 IE (-1.02 mA cm^{-2}) at -0.22 V vs.

RHE (orange dash line). Note that both electron transfer and H_2O_2 diffusion steps would be independent of cell configurations. The larger current density for GDE is, therefore, mostly due to the faster O_2 mass transport to the electrocatalyst/electrolyte/gas interface. Since O_2 in air (molecular diffusivity = 0.2 cm^2 s^{-1}) transports orders of magnitude faster than in water (2×10^{-5} cm^2 s^{-1}),[14] the O_2 depletion on the catalyst surfaces is readily avoided in the GDE setup. Consequently, ORR at the electrode surface would become less diffusion-limited and more kinetics-limited, which is evidenced by the lack of distinct reduction peak in CV (Figure 37a). At a fixed potential of -0.22 V vs. RHE, the AQ–C_3N_4 GDE produced 4.3 times H_2O_2 (60.1 mmol $g_{catalyst}^{-1}$) at higher Faradaic efficiency (42.2 ±1.3%) than the AQ–C_3N_4 IE (14.0 mmol $g_{catalyst}^{-1}$ and 31.0% FE) over a one-hour period (Figure 37 b and c). This large enhancement was achieved because the sufficient O_2 supply eliminated the build-up of O_2 concentration overpotentials, which otherwise would have increased the applied overpotential and thus shifted the reaction selectivity from selective ORR towards HER.

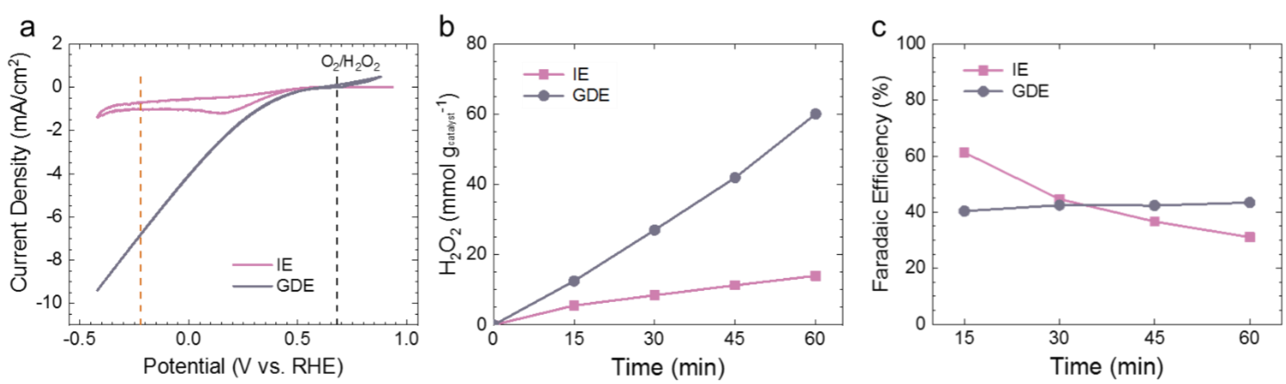

Figure 37. Electrochemical performance of AQ–C_3N_4 in IE and in GDE. (a) Cyclic voltammetry of AQ–C_3N_4 in 0.5 M pH = 9 phosphate buffer on IE (purple) and GDE (grey) purged with O_2. Vertical black dash lines represent redox potentials of O_2/H_2O_2 (0.68 V vs. RHE); orange dash line represents the 0.9 V overpotential for O_2/H_2O_2 (-0.22 V vs. RHE), which is the condition used in (b) and (c). (b) H_2O_2 generation, and (c) Faradaic efficiency for H_2O_2 generation of the two electrode configurations at -0.22 V vs. RHE. All the electrodes had the same area (1 cm^2) and the same catalyst loading (0.5 mg cm^{-2}).

Another observation from Figure 37c is the monotonical decrease of Faradaic efficiency for IE but not or GDE. We believe this is due to the limited O_2 mass transport in IE where O_2 reactants were depleted and became a limiting factor. To prove the O_2 depletion at electrode surface, we first purged the electrolyte with O_2 for 15 min and then applied the an potential bias for 45 min with O_2 gas constantly purging. The external bias was temporarily stopped for 15 min so O_2 gas molecules could be replenished at electrode surface, and then potential was applied again. The cycling process was repeated for two times, and as shown in Figure 38, after the initial ~2 min of sharp current density decrease, AQ–C_3N_4 IE exhibited a gradually decreasing current density for the rest ~43 min of chronoamperometry. The decreasing current density, along with decreasing Faradaic efficiency, proved the insufficient O_2 supply in IE setup even when O_2 gas was bubbled constantly during the experiment, and the deficiency can be significantly improved by a gas diffusion electrode setup.

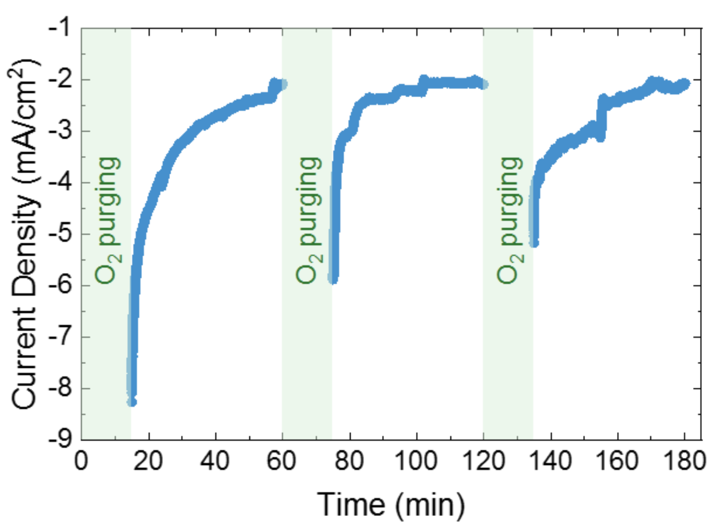

Figure 38. Cycling experiment of AQ-C_3N_4 in IE setup.AQ–C_3N4 IE tested in 0.1M phosphate buffer of pH 9 with repeating cycles of 15 min of O_2 purging (no potential applied) + 45 min of chronoamperometry with constant O_2 purging (-0.22 V vs. RHE biased potential).

6.4.2 AQ-PANI electrocatalysts: IE vs. GDE

The AQ-PANI's capacity to generate H_2O_2 was likely not fully realized by limited O_2 transport in a batch mode and in an immersed electrode setup.[15-17] We fabricated a flow cell equipped with a gas diffusion cathode loaded with AQ-PANI(NS-CNT) as a working prototype (Figure 39).[18] The gas diffusion electrode has been verified in the previous Chapter (6.4.1) to mitigate the O_2 transport limitation.[15] An iridium oxide coated titanium mesh was used as the anode, where water was oxidized to proton and oxygen. Anode and cathode "sandwiched" a cation exchange membrane (Nafion 115) to inhibit the anodic oxidation and/or the self-decomposition of H_2O_2.[15] A thin water channel (1.5 mm) was adopted to minimize charge transfer resistance between the two electrodes.[19] Two passages of electrolytes were flowed parallel to the electrode surfaces, and the flow across cathode in the middle chamber was collected for H_2O_2 quantification.

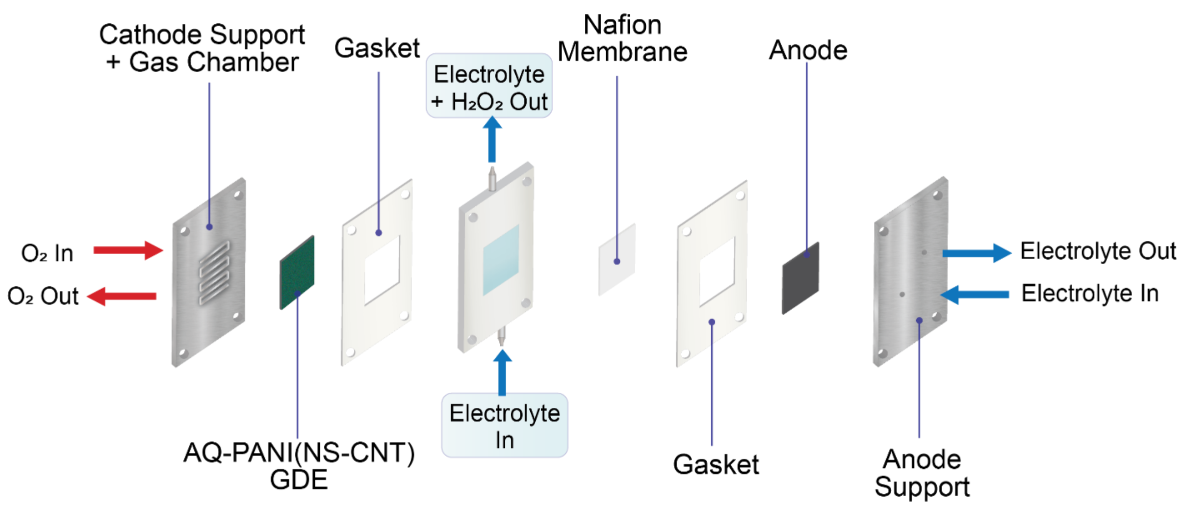

Figure 39. Schematic illustration of the flow cell with gas diffusion cathode. The electrode had an area of 4 cm^2 and total catalyst loading of 1 mg. The distance between cathode and anode was 1.5 mm.

Over a wide range of total current (4 mA to 100 mA), the flow cell showed consistent and high selectivity of H_2O_2 generation (>90%); for example, 1.80 mol $g_{catalyst}^{-1}$ hr^{-1} of H_2O_2 production at 100 mA (25 mA cm^{-2}) with 95.83% selectivity (Figure 40a). Compared with AQ-PANI(NS-CNT) electrode in immersed electrode setup of the same current density (10 mA cm^{-2}, Figure 30), AQ-PANI(NS-CNT) electrode in flow cell setup showed both higher generation (0.68 mol $g_{catalyst}^{-1}$ hr^{-1} vs. 0.21 mol $g_{catalyst}^{-1}$ hr^{-1}) and higher Faradaic efficiency (91.18% vs. 56.75%) due to faster O_2 transport and reaction kinetics.[15] The reactor exhibited a stable H_2O_2 generation capability for 50 hours (>90% Faradaic efficiency), with less than 0.3 V of cell potential increase during the long-term operation (Figure 40b), which makes this electrochemical cell one of the most stable system reported so far (Table 4).

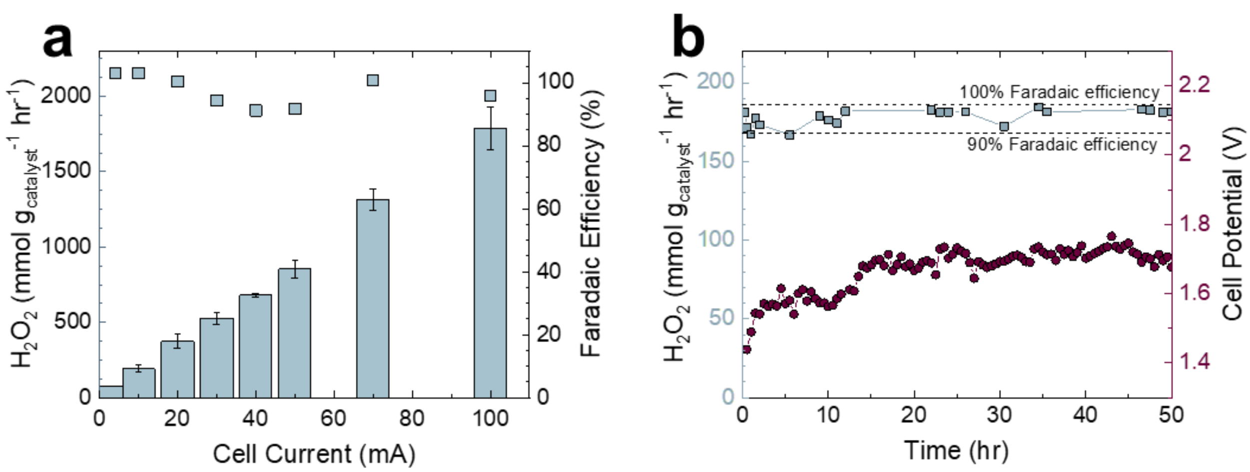

Figure 40. Electrochemical performance of AQ-PANI in GDE cell with electrolyte and O_2. (a) H_2O_2 generation (left y-axis) and Faradaic efficiency (right y-axis) of AQ-PANI(NS-CNT) in flow cell with electrolyte and O_2. The flow rates of O_2 were 10 sccm. The error bars were calculated based on six independent measurements. (b) H_2O_2 generation rate (left y-axis) and cell potential (right y-axis) of the reactor during 50 hours of operation with electrolyte and O_2 at 10 mA.

Table 4. Comparison of 2e- ORR electrocatalysts' stabilities

Catalyst / Electrode	Testing conditions			Performance metrics		Ref.
	Electrolyte	Operation	Duration (h)	Before testing	After testing	
Graphite + carbon black	0.05 M Na_2SO_4 + 100 mg L^{-1} phenol (pH 3)	10 mA cm^{-2}	200	$[H_2O_2]$: 316 mg L^{-1}	260 mg L^{-1} (17.8% loss)	20
Carbon black	Tap water + 0.005 M Na_2SO_4	1.5 mA cm^{-2}	1200	$[H_2O_2]$: 9.8 mg L^{-1}	9.8 mg L^{-1}	6
CoS_xP_y on MWCNTs	0.05 M Na_2SO_4 (pH 3)	25 mA cm^{-2}	6	Current efficiency: 85%	51 – 54%	21
WO on carbon black	0.1 M K_2SO_4	-0.7 V vs. Ag/AgCl	37	$[H_2O_2]$: 479 mg L^{-1}	448 mg L^{-1} (6.5% loss)	22
Oxidized graphite felt	0.05 M Na_2SO_4 (pH 3)	16.7 mA cm^{-2}	15 (10 runs of 1.5 h)	$[H_2O_2]$: 34.4 mg L^{-1}	16.3 mg L^{-1} (47.47% loss)	23
Activated carbon	0.05 M Na_2SO_4 (pH 7)	12.5 mA cm^{-2}	10 (10 runs of 1 h)	$[H_2O_2]$: 8.9 mg L^{-1}	5.6 mg L^{-1} (37% loss)	24
$CoSe_2$ on carbon paper	0.05 M H_2SO_4 (pH 1.2)	0.5 V vs. RHE	6	Faradaic efficiency: 72.2%	53.5%	25
Anthraquinone-modified polyaniline	0.1 M phosphate buffer (pH 8.8)	10 mA (2.5 mA cm^{-2})	50	181 mmol $g_{catalyst}^{-1}$ hr^{-1}	181 mmol $g_{catalyst}^{-1}$ hr^{-1}	This work

In industrial full-scale AOP applications, H_2O_2 concentration of 1 – 4 mg L^{-1} (0.03 – 0.12 mM) is typically used.[26-28] A contour plot describing H_2O_2 concentration in cell outlet at different cell currents and cell electrolyte flow rates was constructed to demonstrate the feasibility of generating highly concentrated H_2O_2, orders of magnitude higher than the concentration typically required for AOP (Figure 41). Note that higher cell current could be readily achieved by cell scale-up, such as enlarging electrode area, stacking layers of electrodes, and operating more reactors.[29-30]

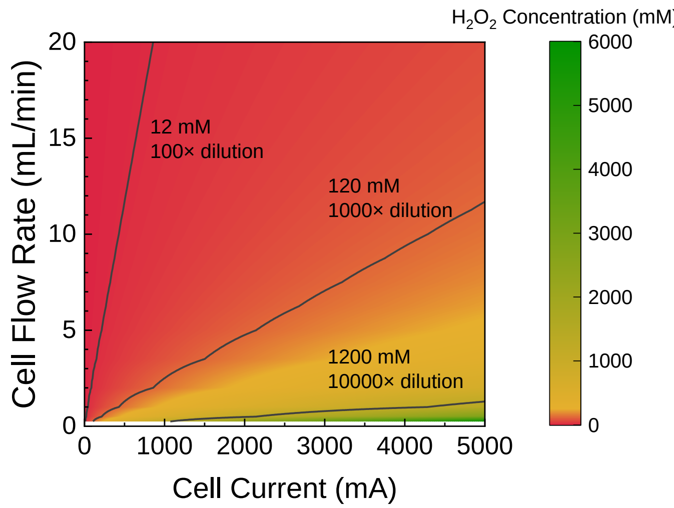

Figure 41. Contour plot of H_2O_2 concentration. H_2O_2 concentration in the cell outlet was plotted with respect to cell current (x-axis) and inlet flow rate (y-axis). Three contour lines indicated concentration of 12 mM (100× dilution), 120 mM (1000× dilution), and 1200 mM (10000× dilution); *i.e.*, dilution to reach the concentration typically employed for AOP. The calculation is based on the assumptions of 90% overall efficiency and negligible performance loss with reactor scale-up.

With considerations of real-world applications, air was supplied to cathode instead of ultrapure O_2 gas. The cell exhibited high selectivity (~90%) and high activity (0.68 mol $g_{catalyst}^{-1}$ hr^{-1} @ 10 mA cm^{-2}, yellow in Figure 42), suggesting $2e^-$ ORR was kinetically favored even with the existence of other inert gases such as nitrogen, although a higher cell potential was needed to drive the reaction. In addition to 0.1 M phosphate buffer (12.57 mS cm^{-1}), the flow cell was able to produce H_2O_2 in simulated wastewater (5.48 mS cm^{-1}) and simulated drinking water (0.865 mS cm^{-1}) as the supporting electrolytes (Figure 42a, Table 5). When electrolyte conductivity decreased in simulated wastewater, the cell maintained its Faradaic efficiency (~80%) and H_2O_2 generation capability at low cell currents (4 – 40 mA). However, the selectivity dropped in simulated drinking water (92.23% @ 4 mA to 66.33% @ 10 mA), possibly due to H_2O_2 degradation by bicarbonate ions.[31] In addition, since the resistance increased both from the solution and from the ion exchange membrane, simulated drinking water required the higher cell potential at the same current density than simulated wastewater and phosphate buffer electrolyte (3.60 V, 1.75 V, 1.35 V @ 4 mA respectively, Figure 42b). This suggested that the largest amount of energy would be necessary to produce unit mass of H_2O_2 in simulated drinking water.

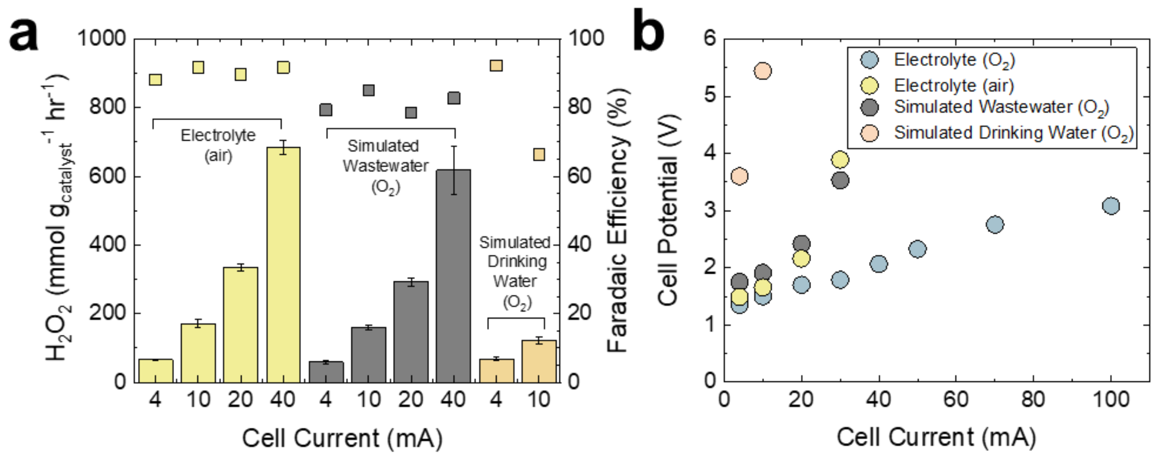

Figure 42. Electrochemical performance of AQ-PANI in GDE cell with other water matrices and air. (a) H_2O_2 generation (left y-axis) and Faradaic efficiency (right y-axis) of AQ-PANI(NS-CNT) in flow cell with electrolyte and air (yellow), simulated wastewater and O_2 (grey), and simulated drinking water and O_2 (orange). The flow rates of O_2 were 10 sccm and the flow rate of air was 50 sccm. The error bars were calculated based on six independent measurements. (b) Cell potential vs. cell current with four different water matrices and gas conditions.

Table 5. Compositions of the water matrices. Due to the complexity of wastewater compositions from various sources, a simple recipe of 5000 mg L^{-1} Na_2SO_4 solution was used to simulate the ionic strength of wastewater.[32-34]

	Synthetic drinking water	Simulated wastewater*	Electrolyte
pH	7.5	7.0	8.8
Conductivity (mS cm^{-1})	0.865	5.48	12.57
Ions (mg L^{-1})			
Bicarbonate (HCO_3^-)	183	0	0
Calcium (Ca^{2+})	40	0	0
Chloride (Cl^-)	71	0	0
Dihydrogen phosphate ($H_2PO_4^-$)	0	0	160
Fluoride (F^-)	1.0	0	
Hydrogenphosphate (HPO_4^{2-})	0	0	9330
Magnesium (Mg^{2+})	12	0	0
Nitrate (NO_3^-)	8.9	0	0
Phosphate (PO_4^-)	0.12	0	0

Silica (SiO_2)	20	0	0
Sodium (Na^+)	89	1620	4510
Sulfate (SO_4^{2-})	48	3380	0
Total Diss. Solids (TDS)	478	5000	14000

Electrical energy per order (E_{EO}), defined as the electrical energy required to reduce the concentration of a contaminant by one order of magnitude (90% reduction) in a unit volume of water, has been widely used to describe the energy effectiveness of a water treatment process.[35] As H_2O_2 could be directly generated in the water source without further purification, energy consumption of H_2O_2 production ($E_{EO,H2O2}$; calculated based on experimental results in simulated drinking water at 4 mA and 3.6 V) could be calculated and compared with the energy consumption of UV irradiation ($E_{EO,UV}$; the second step of on-site AOP) obtained from literature data. As shown in Figure 43 and Table 6,[36-43] the energy consumption of producing H_2O_2 only accounts for 0.2 – 20 % of the overall AOP energy requirement ($E_{EO,H2O2}$ + $E_{EO,UV}$), where a wide range of micropollutants were tested for degradation. The ratio would be much lower in other water matrices with higher conductivities due to their reduced cell potentials.

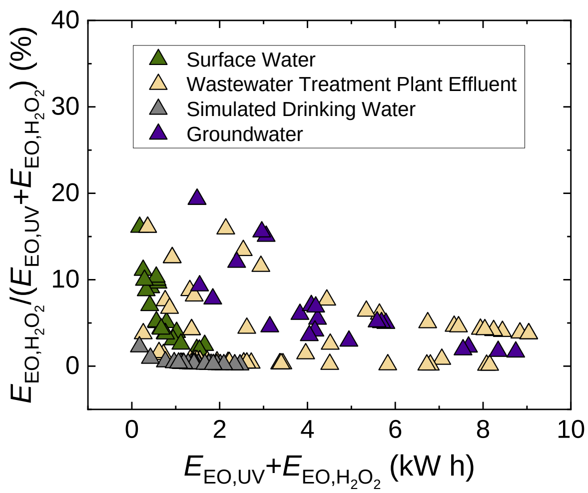

Figure 43. Scatter plot of the percentage of energy consumption of H_2O_2 generation in EEO of overall UV/H_2O_2 AOP process for different water matrices. Each data point represents a set of

experimental data as listed in Table S2. was calculated based on experimental results in simulated drinking water (4 mA, 3.6 V).

Table 6. Energy consumptions of 90% micropollutant degradation via H_2O_2/UV process.Energy was calculated based on cell conditions in simulated drinking water: cell current = 4 mA, cell potential = 3.6 V. At the same current density, it required the highest cell potential to drive the reaction in simulated drinking water, suggesting the highest energy requirement per unit mass of produced H_2O_2 in this condition. The energy consumption, as well as the ratio in overall process, should be lower in other water matrices than those in this table.

Target compound	Target compound concentration	Water matrix	pH	Energy consumption for UV (E_{UV}, kwh m^{-3})	H_2O_2 concentration	Energy consumption for H_2O_2 generation (E_{H2O2}, kwh m^{-3})	$E_{H2O2}/(E_{H2O2}+E_{UV})$ (%)*	Ref
Sulfamethoxazole	0.5 µM	Natural surface water (Lake Zurich)	8	0.39	0.2 mM	0.04	9.09	[36]
p-chlorobenzoic acid				0.75			5.06	
Atrazine				0.98			3.92	
N-Nitrosodimethylamine				1.62			2.41	
Methylparaben	1 µg L^{-1}	Wastewater treatment plant effluent	3	8.1	60 mg L^{-1}	0.34	4.03	[37]
Ethylparaben				5.3			6.03	
Propylparaben				6.4			5.04	
isoButylparaben				7.0			4.63	
Butylparaben				7.9			4.13	
Bisphenol A				8.7			3.76	
isoNonylphenol				7.6			4.28	
Octylphenol				2.6			11.56	
Benzophenone-3				8.5			3.85	
Benzophenone-7				8.7			3.76	
Octyl methoxycinnamate				7.1			4.57	
Homosalate				7.7			4.23	
3-(4-methylbenzyliden) camphor				5.0			6.37	
Octyl dimethylaminobenzoate				4.1			7.66	
17*β*-estradiol	400 ng L^{-1}			2.2			13.39	
ethinylestradiol				1.8			15.89	
Caffeine	50 µg L^{-1}	Pre-treated wastewater treatment plant effluent	7.1	7.0	10 mg L^{-1}	0.06	0.81	[38]
Carbamazepine				3.9			1.45	
Naproxen				1.3			4.23	
Clofibric acid				0.7			7.59	
17*β*-estradiol				1.3			4.23	
Sulphamethoxazole				0.8			6.70	
Diclofenac				0.3			16.08	
Caffeine				4.4	20 mg L^{-1}	0.12	2.55	
Carbamazepine				2.5			4.40	
Naproxen				1.2			8.75	
Clofibric acid				0.8			12.57	
17*β*-estradiol				1.3			8.13	
Sulphamethoxazole				0.8			12.57	
Dimetridazole	1 µg L^{-1}		7	1.74	20 µM	0.004	0.22	[39]

Tinidazole		Simulated drinking water		2.46			0.16	
Omidazole				2.01			0.19	
Metronidazole				1.93			0.20	
Ronidazole				2.34			0.17	
Ibuprofen				1.51			0.26	
Chloramphenicol				1.45			0.27	
Primidone				1.35			0.29	
Venlafaxine				1.13			0.34	
Nalidixic acid				1.18			0.33	
Flumequine				1.42			0.27	
Atenolol				1.39			0.28	
Metoprolol				1.28			0.30	
Erythromycin				1.80			0.22	
Azithromycin				1.93			0.20	
Roxithromycin				2.09			0.19	
Carbamazepine				1.16			0.34	
Caffeine				1.75			0.22	
Gemfibrozil				1.41			0.28	
Naproxen				1.11			0.35	
Propranolol				0.76			0.51	
Clenbuterol				1.66			0.23	
Diclofenac				0.17			2.25	
Trimethoprim				1.18			0.33	
Salbutamol				1.85			0.21	
Ractopamine				0.96			0.41	
Bisphenol A				1.06			0.37	
Sulfamethoxazole				0.42			0.92	
Dimetridazole	1 μg L^{-1}	Secondary wastewater treatment plant effluent	7	3.36	50 μM	0.01	0.29	
Tinidazole				3.36			0.29	
Omidazole				4.50			0.22	
Metronidazole				6.79			0.14	
Ronidazole				3.36			0.29	
Ibuprofen				6.71			0.15	
Chloramphenicol				1.54			0.63	
Primidone				2.18			0.45	
Venlafaxine				2.71			0.36	
Nalidixic acid				0.71			1.36	
Flumequine				2.54			0.38	
Atenolol				2.54			0.38	
Metoprolol				2.21			0.44	
Erythromycin				5.82			0.17	
Azithromycin				8.07			0.12	
Roxithromycin				3.43			0.28	
Carbamazepine				3.39			0.29	
Caffeine				1.93			0.50	
Gemfibrozil				8.14			0.12	
Naproxen				2.54			0.38	
Propranolol				1.71			0.57	
Clenbuterol				1.32			0.73	
Diclofenac				0.25			3.76	
Trimethoprim				1.43			0.68	
Salbutamol				2.61			0.37	
Ractopamine				1.54			0.63	
Bisphenol A				1.47			0.66	
Sulfamethoxazole				0.61			1.58	
Enrofloxacin	1 g L^{-1}	Surface water	7.0	91.7	20 mM	3.91	4.09	[40]
Pefloxacin				176.1			2.17	
Sulfaquinoxaline	4 mg L^{-1}			63.7	5 mM	0.98	1.52	
Sulfolane	200 μg L^{-1}	Groundwater	8.5	4.0	40 mg L^{-1}	0.23	5.44	[41]

				3.6			6.01	
				2.6	80 mg L^{-1}	0.46	15.03	
				2.5			15.54	
	260 µg L^{-1}		7.8	7.5	30 mg L^{-1}	0.17	2.22	
	12.6 mg L^{-1}		9.1	4.0			4.08	
Atrazine	10 µg L^{-1}	Surface water	8.0	0.54	10 ppm	0.06	9.62	42
Bromacil				0.52			9.95	
Ibuprofen				0.50			10.31	
N-nitrosodimethylamine	20 µg L^{-1}			0.30			16.08	
Atrazine	10 µg L^{-1}			0.73	5 ppm	0.03	3.79	
Bromacil				0.91			3.06	
Ibuprofen				0.74			3.74	
N-nitrosodimethylamine	20 µg L^{-1}			0.30			8.74	
1,1,1-trichloorethane	5 – 10 µg L^{-1}			0.23			11.10	
2,4-chloorfenoxy acetic acid				1.45			1.94	
Bentazone				1.51			1.87	
Carbendazim				0.63			4.36	
Clofibrinic acid				0.54			5.05	
Diclofenac				0.15			16.08	
isoproturon				1.09			2.57	
2-methyl-4-chloro-phenoxy acetic acid				0.53			5.14	
Methyl-tertiary-butylether				0.64			4.30	
Metolachlor				0.38			7.03	
Tertiary-amyl-methylether				0.26			9.95	
Methyl tert-butyl ether	2.34 mg L^{-1}	Groundwater	7.0	1.4	25 mg L^{-1}	0.14	9.31	43
			9.0	4.8			2.91	
			7.0	1.2	50 mg L^{-1}	0.29	19.32	
			9.0	3.8			7.03	
	0.963 mg L^{-1}		7.0	3.9	25 mg L^{-1}	0.14	3.55	
			9.0	8.2			1.72	
			7.0	3.9	50 mg L^{-1}	0.29	6.86	
			9.0	5.5			4.96	
	0.029 mg L^{-1}		7.0	17.9	25 mg L^{-1}	0.14	0.80	
			9.0	246.6			0.06	
			7.0	12.9	50 mg L^{-1}	0.29	2.18	
			9.0	40.3			0.71	
	0.198 mg L^{-1}		7.0	3.0	25 mg L^{-1}	0.14	4.57	
			9.0	8.6			1.64	
			7.0	2.1	50 mg L^{-1}	0.29	12.03	
			9.0	5.4			5.05	
	0.033 mg L^{-1}		7.0	1.7	25 mg L^{-1}	0.14	7.79	
			9.0	7.4			1.90	
			7.0	1.2	50 mg L^{-1}	0.29	19.32	
			9.0	5.3			5.14	

6.5 Engineering Implications

In this Chapter, we successfully fabricated two prototype electrocatalytic H_2O_2 generation cells: batch reactor equipped with carbon nitride-anthraquinone composite gas diffusion cathode, and flow reactor equipped with polyaniline-anthraquinone composite gas diffusion cathode. The first one achieved an optimal H_2O_2 production rate of 60.1 mmol $g_{catalyst}^{-1}$ per hour at a maximum Faradaic efficiency of 42.2% in an immersed electrode setup, and the second one demonstrated H_2O_2 production at a rate of 1.80 mol $g_{catalyst}^{-1}$ hr^{-1} at 100 mA (25 mA cm^{-2}) with Faradaic efficiency of 95.83%. The significant improvement is due to not only a more successful catalyst design, but also a more efficient electrode and cell architecture.

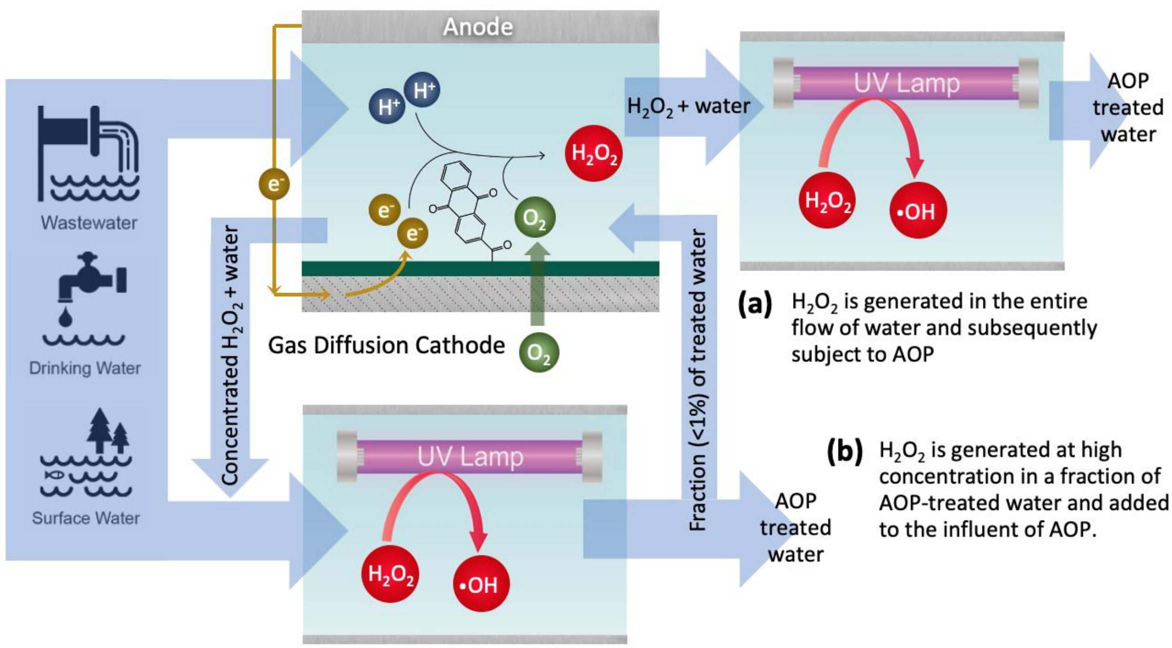

Figure 44. Proposed schematic of on-site AOP process of H_2O_2 generation with AQ-PANI composite in a flow cell and H_2O_2 activation with UV irradiation. (a) H_2O_2 is generated in the entire flow of water and subsequently subject to AOP. (b) H_2O_2 is generated at high concentration in a fraction of AOP-treated water and added to the influent of AOP.

The flow cell's capacity to produce H_2O_2 in various water matrices (phosphate buffer electrolyte, simulated drinking water, and simulated wastewater) underscored its wide feasibility in different scenarios with diverse water qualities (Figure 44a). Assuming a small-scale distributed water treatment at design capacity of 100 L/h, providing H_2O_2 required for typical AOP (*e.g.*, 4 mg L^{-1} or 0.12 mM) would require a cell with cathode surface of 8.5 cm^2 operated at 85 mA (10 mA cm^{-2}). For simulated surface water and wastewater, this would correspond to cell potentials of 5.44 and 1.91 V, respectively. While other engineering considerations require further investigation, the electrochemical H_2O_2 production cell is ready for deploy, if judged solely based on the capability to provide sufficient amount of H_2O_2 for AOP application. This option is likely more suitable when AOP is applied as a polishing step (i.e., after membrane filtration) as long as the water has a sufficient conductivity.

Instead of flowing the entire volume of water through the H_2O_2 production cell, a small fraction of AOP-treated water can be injected to the H_2O_2 production cell as an electrolyte. This option is likely more suitable for more complex water matrices, with high levels of COD and a greater load of organic constituents. It requires additional piping, but obviates various complications, such as compartment fouling, that may arise by flowing the complex water through the electrochemical cell. This alternative treatment scheme, shown in Figure 44b, is possible due to high H_2O_2 production efficiency of the flow cell developed in this chapter as well as modular, additive nature of electrochemical process wherein the total H_2O_2 production can be readily adjusted by engineering parameters such as electrolyte flow rate and electrode area among others. The simulation shown in Figure 41 suggested that it is possible to produce H_2O_2 at concentration orders of magnitudes higher than required in AOP; for example, 100 times higher than AOP requirement such that only 1% of treated water needs to be recycled to H_2O_2

production cell as an electrolyte. In either scenario, the electricity consumption for H_2O_2 production would be only up to 1/5 of that of subsequent UV step, while a more comprehensive techno-economic analysis including the costs of equipment installation and maintenance should be performed. Regardless, this study demonstrates the feasibility of drastically advancing UV/H_2O_2 AOP to a completely chemical-supply-free process.

6.5 References

1. Näykki, T.; Jalukse, L.; Helm, I.; Leito, I. Dissolved Oxygen Concentration Interlaboratory Comparison: What Can We Learn? *Water* **2013,** *5* (2).

2. Diffusion Coefficients Gases in Water. https://www.engineeringtoolbox.com/diffusion-coefficients-d_1404.html.

3. Schmitz, D.; Anlauf, R.; Rehrmann, P. Effect of Air Content on the Oxygen Diffusion Coefficient of Growing Media. *American Journal of Plant Sciences* **2013,** *4* (5), 955-963.

4. Taqieddin, A.; Nazari, R.; Rajic, L.; Alshawabkeh, A. Review—Physicochemical Hydrodynamics of Gas Bubbles in Two Phase Electrochemical Systems. *Journal of the Electrochemical Society* **2017,** *164* (13).

5. Campos-Martin, J. M.; Blanco-Brieva, G.; Fierro, J. L. G. Hydrogen Peroxide Synthesis: An Outlook beyond the Anthraquinone Process. *Angewandte Chemie International Edition* **2006,** *45* (42), 6962-6984.

6. Barazesh, J. M.; Hennebel, T.; Jasper, J. T.; Sedlak, D. L. Modular Advanced Oxidation Process Enabled by Cathodic Hydrogen Peroxide Production. *Environ Sci Technol* **2015,** *49* (12), 7391-7399.

7. Barros, W. R. P.; Ereno, T.; Tavares, A. C.; Lanza, M. R. V. In Situ Electrochemical Generation of Hydrogen Peroxide in Alkaline Aqueous Solution by using an Unmodified Gas Diffusion Electrode. *ChemElectroChem* **2015,** *2* (5), 714-719.

8. Mathur, V. K.; Crawford, J. Fundamentals of Gas Diffusion Layers in PEM Fuel Cells. In *Recent Trends in Fuel Cell Science and Technology*, Basu, S., Ed. Springer New York: New York, NY, 2007; pp 116-128.

9. Yin, F.; Liu, Y.; Wang, C.; Liu, H. Assessing the electron transfer and oxygen mass transfer of the oxygen reduction reaction using a new electrode kinetic equation. *Physical Chemistry Chemical Physics* **2018,** *20* (23), 16159-16166.

10. Bard, A. J.; Faulkner, L. R. *Electrochemical Methods: Fundamentals and Applications*. 2 ed.; Wiley Global Education: 2000.

11. Cheng, F.; Chen, J. Metal–air batteries: from oxygen reduction electrochemistry to cathode catalysts. *Chemical Society Reviews* **2012,** *41* (6), 2172-2192.

12. Lei, Y.; Sun, R.; Zhang, X.; Feng, X.; Jiang, L. Oxygen-Rich Enzyme Biosensor Based on Superhydrophobic Electrode. *Advanced Materials* **2016,** *28* (7), 1477-1481.

13. Xu, W.; Lu, Z.; Sun, X.; Jiang, L.; Duan, X. Superwetting Electrodes for Gas-Involving Electrocatalysis. *Accounts of Chemical Research* **2018,** *51* (7), 1590-1598.

14. Cussler, E. L. *Diffusion: Mass Transfer in Fluid Systems*. Cambridge University Press: 1997.

15. Zhu, Q.; Pan, Z.; Hu, S.; Kim, J.-H. Cathodic Hydrogen Peroxide Electrosynthesis Using Anthraquinone Modified Carbon Nitride on Gas Diffusion Electrode. *ACS Applied Energy Materials* **2019,** *2* (11), 7972-7979.

16. Siahrostami, S.; Villegas, S. J.; Bagherzadeh Mostaghimi, A. H.; Back, S.; Farimani, A. B.; Wang, H.; Persson, K. A.; Montoya, J. A Review on Challenges and Successes in Atomic-Scale Design of Catalysts for Electrochemical Synthesis of Hydrogen Peroxide. *ACS Catalysis* **2020,** *10* (14), 7495-7511.

17. Zhang, H.; Li, Y.; Zhang, H.; Li, G.; Zhang, F. A Three-dimensional Floating Air Cathode with Dual Oxygen Supplies for Energy-efficient Production of Hydrogen Peroxide. *Scientific Reports* **2019,** *9* (1), 1817.

18. Xia, C.; Xia, Y.; Zhu, P.; Fan, L.; Wang, H. Direct electrosynthesis of pure aqueous H_2O_2 solutions up to 20% by weight using a solid electrolyte. *Science* **2019,** *366* (6462), 226.

19. Hu, S. Membrane-less photoelectrochemical devices for H2O2 production: efficiency limit and operational constraint. *Sustainable Energy & Fuels* **2019,** *3* (1), 101-114.

20. An, J.; Li, N.; Wu, Y.; Wang, S.; Liao, C.; Zhao, Q.; Zhou, L.; Li, T.; Wang, X.; Feng, Y. Revealing Decay Mechanisms of H2O2-Based Electrochemical Advanced Oxidation Processes after Long-Term Operation for Phenol Degradation. *Environ Sci Technol* **2020,** *54* (17), 10916-10925.

21. Ye, Z.; Guelfi, D. R. V.; Álvarez, G.; Alcaide, F.; Brillas, E.; Sirés, I. Enhanced electrocatalytic production of H_2O_2 at Co-based air-diffusion cathodes for the photoelectro-Fenton treatment of bronopol. *Applied Catalysis B: Environmental* **2019,** *247*, 191-199.

22. Paz, E. C.; Aveiro, L. R.; Pinheiro, V. S.; Souza, F. M.; Lima, V. B.; Silva, F. L.; Hammer, P.; Lanza, M. R. V.; Santos, M. C. Evaluation of H_2O_2 electrogeneration and decolorization of Orange II azo dye using tungsten oxide nanoparticle-modified carbon. *Applied Catalysis B: Environmental* **2018,** *232*, 436-445.

23. Wang, Y.; Zhou, W.; Gao, J.; Ding, Y.; Kou, K. Oxidative modification of graphite felts for efficient H_2O_2 electrogeneration: Enhancement mechanism and long-term stability. *Journal of Electroanalytical Chemistry* **2019,** *833*, 258-268.

24. Zhou, W.; Rajic, L.; Chen, L.; Kou, K.; Ding, Y.; Meng, X.; Wang, Y.; Mulaw, B.; Gao, J.; Qin, Y.; Alshawabkeh, A. N. Activated carbon as effective cathode material in iron-free Electro-Fenton process: Integrated H_2O_2 electrogeneration, activation, and pollutants adsorption. *Electrochimica Acta* **2019,** *296*, 317-326.

25. Sheng, H.; Janes, A. N.; Ross, R. D.; Kaiman, D.; Huang, J.; Song, B.; Schmidt, J. R.; Jin, S. Stable and selective electrosynthesis of hydrogen peroxide and the electro-Fenton process on $CoSe_2$ polymorph catalysts. *Energy & Environmental Science* **2020,** *13* (11), 4189-4203.

26. DDB Engineering, I. *Groundwater Replenishment System 2013 Annual Report*; DDB Engineering, Inc., 2013.

27. Wetterau, G.; Chalmers, B.; Schulz, C. *Full-scale testing of UV/chlorine for portable reuse*; IUVA News, 2018.

28. Kwon, M.; Royce, A.; Gong, Y.; Ishida, K. P.; Stefan, M. I. UV/chlorine vs. UV/H2O2 for water reuse at Orange County Water District, CA: a pilot study. *Environmental Science: Water Research & Technology* **2020,** *6* (9), 2416-2431.

29. Goodridge, F.; Scott, K. Electrolytic Reactor Design, Selection, and Scale-up. In *Electrochemical Process Engineering: A Guide to the Design of Electrolytic Plant*, Goodridge, F.; Scott, K., Eds. Springer US: Boston, MA, 1995; pp 177-244.

30. Sulaymon;, A. H.; Abbar, A. H. *Scale-Up of Electrochemical Reactors, Electrolysis*. 2012.

31. Jawad, A.; Chen, Z.; Yin, G. Bicarbonate activation of hydrogen peroxide: A new emerging technology for wastewater treatment. *Chinese Journal of Catalysis* **2016,** *37* (6), 810-825.

32. Chanworrawoot, K.; Hunsom, M. Treatment of wastewater from pulp and paper mill industry by electrochemical methods in membrane reactor. *Journal of Environmental Management* **2012,** *113*, 399-406.

33. El-Ashtoukhy, E. S. Z.; Amin, N. K.; Abdelwahab, O. Treatment of paper mill effluents in a batch-stirred electrochemical tank reactor. *Chemical Engineering Journal* **2009,** *146* (2), 205-210.

34. Santos, I. D.; Dezotti, M.; Dutra, A. J. B. Electrochemical treatment of effluents from petroleum industry using a Ti/RuO_2 anode. *Chemical Engineering Journal* **2013,** *226*, 293-299.

35. Olya, K.; James, B.; Marta, L.; Keith, B.; Thomas, O. Standard reporting of Electrical Energy per Order (EEO) for UV/H2O2 reactors (IUPAC Technical Report). *Pure and Applied Chemistry* **2018,** *90* (9), 1487-1499.

36. Katsoyiannis, I. A.; Canonica, S.; von Gunten, U. Efficiency and energy requirements for the transformation of organic micropollutants by ozone, O_3/H_2O_2 and UV/H_2O_2. *Water Res* **2011,** *45* (13), 3811-3822.

37. Hansen, K. M. S.; Andersen, H. R. Energy Effectiveness of Direct UV and UV/H_2O_2 Treatment of Estrogenic Chemicals in Biologically Treated Sewage. *International Journal of Photoenergy* **2012,** *2012*, 270320.

38. *Guidance Document for Integrating UV-based Advanced Oxidation Processes (AOPs) Into Municipal Wastewater Treatment Plants*; Ministry of the Environment and Climate Change Showcasing Water Innovation Program (SWI): 2015.

39. Guo, K.; Wu, Z.; Yan, S.; Yao, B.; Song, W.; Hua, Z.; Zhang, X.; Kong, X.; Li, X.; Fang, J. Comparison of the UV/chlorine and UV/H_2O_2 processes in the degradation of PPCPs in simulated drinking water and wastewater: Kinetics, radical mechanism and energy requirements. *Water Res* **2018,** *147*, 184-194.

40. Qiu, W.; Zheng, M.; Sun, J.; Tian, Y.; Fang, M.; Zheng, Y.; Zhang, T.; Zheng, C. Photolysis of enrofloxacin, pefloxacin and sulfaquinoxaline in aqueous solution by UV/H_2O_2, UV/Fe(II), and UV/H_2O_2/Fe(II) and the toxicity of the final reaction solutions on zebrafish embryos. *Science of The Total Environment* **2019,** *651*, 1457-1468.

41. Yu, L.; Iranmanesh, S.; Keir, I.; Achari, G. A field pilot study on treating groundwater contaminated with sulfolane using UV/H_2O_2. *Water* **2020,** *12* (4), 1200.

42. Lekkerkerker-Teunissen, K.; Knol, A. H.; Derks, J. G.; Heringa, M. B.; Houtman, C. J.; Hofman-Caris, C. H. M.; Beerendonk, E. F.; Reus, A.; Verberk, J. Q. J. C.; van Dijk, J. C. Pilot Plant Results with Three Different Types of UV Lamps for Advanced Oxidation. *Ozone: Science & Engineering* **2013,** *35* (1), 38-48.

43. Sutherland, J.; Adams, C.; Kekobad, J. Treatment of MTBE by air stripping, carbon adsorption, and advanced oxidation: technical and economic comparison for five groundwaters. *Water Res* **2004,** *38* (1), 193-205.

Chapter 7: H_2O_2 Activation with FeOCl-Based Catalysts: Packed-Bed Reactor and Electro-Fenton

7.1 Introduction

In advanced oxidation process, after H_2O_2 is produced, either via industrial pathway or electrochemical pathway as we previously discussed, it needs to be activated on site to produce hydroxyl radical ($^{\bullet}OH$) for oxidative treatment of wastewater due to $^{\bullet}OH$'s ultra-short lifetime (a few microseconds).[1] In current AOPs, H_2O_2 activation is mostly achieved via UV irradiation and is likely a viable option when AOP is applied as a polishing step. However, in modular, small-scale, distributed application, UV is limited by its high maintenance requirement, prevalent scaling, and high energy cost (*e.g.*, due to low UV absorption by H_2O_2 and as discussed in Chapter 6.5). Low UV transmission in wastewater containing a large amount of organics and NOM with large molecular weights is another huge challenge. Conventional homogeneous Fenton catalysts utilizing dissolved Fe^{2+}/Fe^{3+} redox pair, commonly used in large-scale centralized water treatment plants, is also not applicable in such decentralized scenarios due to their reduced efficiency at neutral pH and formation of large amounts of iron sludge that requires subsequent treatment. The use of heterogeneous catalysts that are independent of continuous chemical inputs and additional treatment measures is an ideal activation strategy for distributed water treatment. Previous studies have suggested that up to 70% removal of COD (up to 3000 mg L^{-1}) from various industrial wastewaters such as textile,[2-3] tannery,[4] and other recalcitrant wastewaters is feasible via heterogenous Fenton,[5-6] which is comparable to that of wet oxidation efficiency.[7]

We aim to develop new heterogeneous catalyst based on the novel Fenton catalyst, FeOCl (Figure 45),[8-9] that function via efficient redox cycling between Fe(III) and Fe(II) on FeOCl nanosheet crystals to promote H_2O_2 activation. The rapid conversion of Fe(III) to Fe(II) (the rate-limiting step for H_2O_2 activation and $^{\bullet}OH$ production) is enabled by regulating the coordination environment of the Fe atom, *i.e.*, Fe reduction potential is increased by electrophilic Cl and O coordination, more efficient single e^- transfer from H_2O_2, and homolytic cleavage of H_2O_2 for selective $^{\bullet}OH$ production. Consequently, the H_2O_2 dehydrogenation energy barrier for FeOCl (0.23 eV)[10] is much lower than that for other catalysts such as Fe_2O_3 (0.76 eV), a benchmark Fenton-like catalyst frequently employed in past works. This unique chemical property makes FeOCl more reactive and pH-insensitive (up to neutral) compared to the most reported iron catalysts, including Fe_2O_3, Fe_3O_4, and FeOOH.[11]

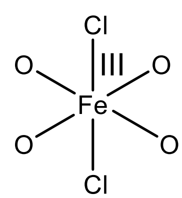

Figure 45. Chemical structure of iron oxychloride.

The as-synthesized FeOCl catalysts are nanoparticles; they were normally tested in a batch reactor with intensive stirring.[8] The FeOCl nanoparticles need to be filtered out after the contaminants degradation, which process would increase the treatment cost and decrease the feasibility and sustainability of the entire treatment option. We thus propose to incorporate FeOCl onto a porous, chemically-stable substrate and fill the catalysts into a packed bed reactor, where H_2O_2 will be activated to $^{\bullet}OH$ at the surfaces of the catalysts. Researchers have developed several packed bed systems, including Fe/carbon,[12-15] Fe/zeolite,[13] copper single atom/carbon nitride,[16] La-Fe montmorillonite,[17] and Fe_2O_3/Al_2O_3.[18] We expect our system to achieve an improved performance compared with the previous studies due to the rapid H_2O_2 activation and the wider pH feasibility of FeOCl catalysts.

We also suggest that a biased reduction potential can expedite the rate-limiting conversion from Fe(III) to Fe(II), and the Fenton-like reaction would be driven electrochemically so the overall contaminant degradation kinetics would be improved. Commonly known as "electro-Fenton" reaction, the concept has been realized in many electrochemical systems, such as Fe/carbon,[19-24] Fe-Cu/carbon,[25] FeOCl/carbon,[26-27] FeOCl/MoS_2/graphite felt,[28] Cu-Fe nano-layered double hydroxide/carbon nanotube,[29] stainless steel,[30] and Pd- iron oxide/indium tin oxide.[31] We hope to expand the toolbox of electro-Fenton cathode materials by combining FeOCl with a conductive carbon substrate and investigating the composite material's degradation capacity and mechanism. With both packed bed reactor and electrochemical reactor, we therefore explored the possibilities of activating H_2O_2 without additional chemical supply and with no or little energy input.

7.2 Experimental Methods

7.2.1 Preparation and tests of FeOCl-based packed bed catalyst

7 grams of iron(III) chloride hexahydrate ($FeCl_3{\cdot}6H_2O$, reagent grade, >98.0%) was mixed with 7 grams of molecular sieve (8-12 mesh, 4 Å beads) in 5 mL of anhydrous ethanol. The molecular sieve spheres have diameters of 1.68 to 2.38 mm. The mixture was sonicated for 2 hours under 40 kHz to ensure a thorough liquid impregnation and subsequently a 22 hours of incubation with continuous shaking at 150 rpm. The suspension was calcinated in a closed

alumina crucible set in muffle furnace for 2 hours at 220°C with a heating ramp rate of 10 °C min^{-1}. The collected beads were then sonicated with 1.2 g mL^{-1} $FeCl_3$/anhydrous ethanol solution for 2 hours, incubated for 22 hours, and calcinated with the same heating program. The final product, named MS-FeOCl, was naturally cooled and rinsed with deionized water for several times to wash off the loosely bound particles and residual impurities, and then dried in a vacuum oven at room temperature for 16 hours. The beads were filled into a packed bed reactor with inner diameter of 1.1 mm and length of 9 cm (Figure 47). The bottom of the reactor was sealed with a fine porous fritted disc filter (Chemglass, 4.0-5.5 µm pore size) and the top was covered with a membrane (Supor 800, 0.8 µm pore size, Pall Corporation) to prevent catalytic beads being flushed out from the reactor. Two streams of H_2O_2 solution (10 mM) and bisphenol A (BPA) solution (400 µM) were injected into the reactor at the same flow rate of 0.16 mL min^{-1} and the effluent was collected for analysis. BPA concentration was measured by an Agilent High-Performance Liquid Chromatography (HPLC) equipped with a C18 reverse phase column (80 Å, Agilent Technologies) and a photodiode array detector. The isocratic mobile phase consisting of 55% 0.1 wt% phosphoric acid and 45% acetonitrile was eluted at a flow rate of 2 mL min^{-1}. The solution pH was measured with a pH meter (Orion Versastar, Thermo Scientific). Chloride concentration was measured by an ion chromatography (930 Compact IC Flex, Metrohm). X-ray diffraction (XRD) patterns were obtained using a Rigaku SmartLab X-ray diffractometer equipped with a Cu-target X-ray tube (λ = 0.154nm) which was operated at 40 mA and 44 kV. Scanning electron microscopy (SEM) analysis was performed using a Hitachi SU8230 cold field-emission SEM microscope.

7.2.2 Preparation and tests of FeOCl-based electrodes

FeOCl was prepared by heating $FeCl_3 \cdot 6H_2O$ in a closed alumina crucible at a ramp temperature rate of 10 °C min^{-1} to 220 °C and maintaining this temperature for 1 hour. The as-synthesized FeOCl and as-purchased graphene (nanoplatelets, surface area 750 m^2 g^{-1}) were mixed with different mass ratios in 25/75 (v/v) and dispersed in water/ethanol mixture with Nafion (15 wt% of the catalyst mass). The catalyst concentration of the suspension was kept at 2 mg mL^{-1} and the suspension was sonicated for 1 hour. The mixture was then slowly and uniformly drop-casted onto carbon paper (Toray Paper 120, Fisher), and dried in a 80 °C oven for 16 hours. A Ag/AgCl electrode filled with saturated KCl solution (CHI111, CH Instruments) was used as the reference electrode; a titanium mesh (Goodfellow) coated with iridium oxide was used as the counter electrode. The electrochemical tests were performed in glass beaker with a lid to maintain the distance between electrodes, and 20 mL of electrolyte (pH = 3.5) was used, containing 0.1 M phosphate buffer, 2 mM H_2O_2, and 50 µM BPA. 100 µL of electrolyte was sampled every 15 minutes within a 90 minutes period for BPA concentration detection.

7.3 Results and Discussion

7.3.1 Packed bed reactor

The successful synthesis of FeOCl and MS-FeOCl were proved by XRD patterns as shown in Figure 46a. For both synthesized FeOCl and MS-FeOCl, four major XRD peaks located at 10.8°, 26.0°, 35.5°, and 38.1° were detected, corresponding to the (010), (110), (021), and (111) crystal facets, respectively, which are consistent with pure sheet-like FeOCl crystals (JCPDS No. 72-0619).[11] SEM image of MS-FeOCl showed the coral-like FeOCl nanorods of

150-250 nm width and 600-800 nm length were attached to the porous surface of molecular sieves. The size of FeOCl nanorods in MS-FeOCl was slightly bigger than that of FeOCl,[11] which probably is due to the heterogeneous nucleation process of MS-FeOCl instead of the homogeneous nucleation process of FeOCl.

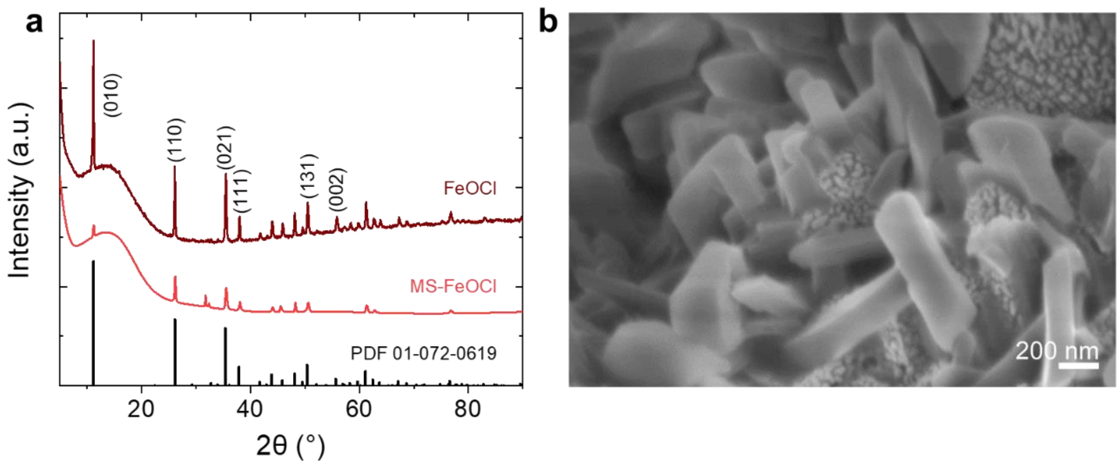

Figure 46. XRD and SEM of FeOCl-based materials.(a) XRD spectra of FeOCl, MS-FeOCl, and powder diffraction file of FeOCl particle crystal. (b) SEM images of MS-FeOCl. The sample was gently ground. The white bars at bottom right corner represent the scales of 500 nm.

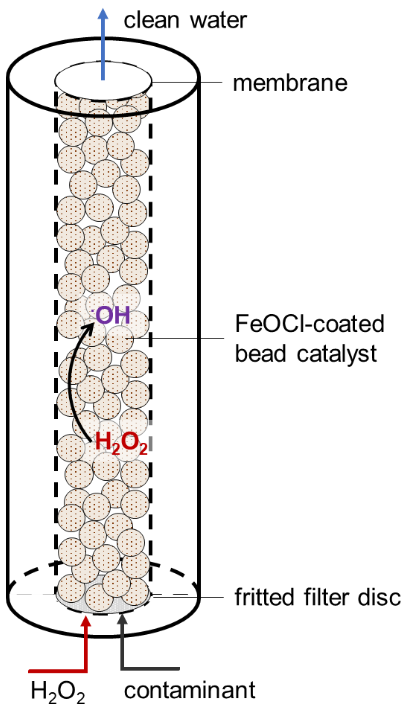

Figure 47. Schematic illustration of packed bed reactor with FeOCl-based catalyst beads.

The MS-FeOCl beads were tested in a packed bed reactor as illustrated by Figure 47, where one stream of 10 mM H_2O_2 and another stream of 400 µM BPA were injected from the bottom of the reactor simultaneously at the same flow rate of 0.16 mL min^{-1}, so the concentration of H_2O_2 and BPA inside the reactor chamber would be 5 mM and 200 µM, respectively. BPA was chosen as the model compound due to its fast reaction kinetics with hydroxyl radicals and its prevalence as a recalcitrant contaminant in the environment.[32-33] The fritted filter disc and the membrane had pore sizes much larger than that the size of BPA, so all the concentration decrease can be attributed to the adsorption or degradation by MS-FeOCl. Samples were collected for each 30 min interval (except the first 30 min), and the averaged BPA concentration and pH were measured within this time interval (i.e., C/C_0 and pH data points at 1 hour represented the averaged C/C_0 and pH for 0.5-1 hour of running time). The catalysts were collected after each 6 hours of operation, washed with DI water, and dried in a vacuum oven at room temperature for 16 hours. As shown in Figure 48, the MS-FeOCl packed bed reactor can degrade 100% of highly concentrated BPA in the first 6-hour run, and over 90% of BPA in the second 6-hour run. At the third 6-hour run, the degradation rate was decreased and over 50% of BPA could be degraded within the period.

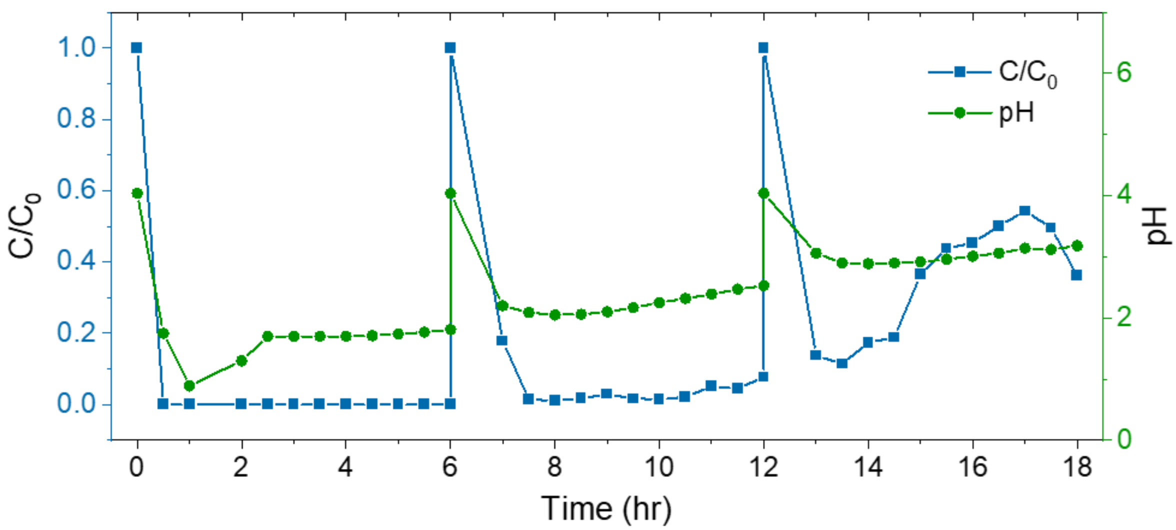

Figure 48. Degradation and pH profile of MS-FeOCl packed bed reactor.

The decline of performance could be attributed to the loss of chloride and iron. The Cl^- concentration measured by ion chromatography was around 600 ppm after 6 hours of operation, which suggested a significant amount Fe-Cl bonds were broken and replaced by Fe-O or Fe-OH bonds. The change of pH further consolidated this speculation: for all three 6-hour runs, pH values dropped dramatically from the inlet value 4.0 to an averaged value of 1.6 (first), 2.2 (second), and 3.0 (third). The pH drop during each operation was due to iron hydrolysis as described by Equation 19,[34] where the reactive Fe(III) was oxidized to the non-reactive $Fe(OH)_3$ and three protons were released. The increasing trend of averaged pH value among the three tests was likely due to the loss of Fe(III) ions available for being oxidized. Therefore, the loss of chloride and iron led to the overall decrease of MS-FeOCl packed bed reactor's degradation performance.

$$Fe^{3+} + 3\ H_2O \rightarrow Fe(OH)_3 + 3\ H^+ \qquad \text{(Equation 19)}$$

The preliminary result proved the possibility of incorporating FeOCl to a chemically-stable substrate and using the catalyst as packed bed materials for contaminant degradation. However, the overall performance decreased during the 18-hour operation, which is likely due to chloride and iron leaching. Future researches need to focus on forming stronger bonding between iron and chloride or stronger coordination between iron and the surrounding atoms, and regenerating the catalyst with a facile and cost and energy-efficient method.

7.3.2 Electro-Fenton reaction

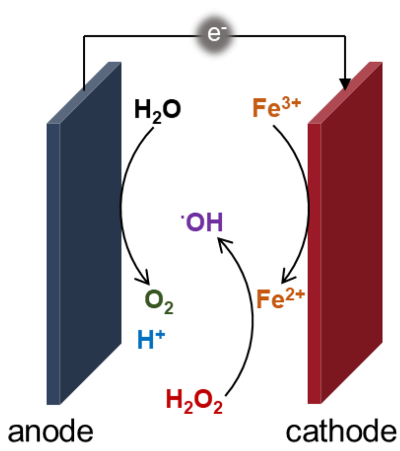

Figure 49. Schematic illustration of electro-Fenton reactions.

In the electro-Fenton reactor (Figure 49), the IrOx/Ti anode oxidized water to oxygen gas and protons, and the cathode reduced the Fe(III) to Fe(II), which catalyzed the activation of H_2O_2 to •OH. The protons produced by the anode helped maintain the low pH preferred for the Fenton-like reaction. As shown in Figure 50a, CVs of FeOCl/graphene samples exhibited additional pairs of redox peaks at $E_{1/2}$ = 0.76 V vs. RHE (1:1) and at $E_{1/2}$ = 0.75 V vs. RHE (3:1) compared with CV of graphene. This redox peak could be attributed to the redox of Fe^{2+}/Fe^{3+}, which has a standard redox potential of 0.77 V vs. RHE. The increase of FeOCl mass ratio in the loaded catalytic material led to the decrease of current density, likely due to the low conductivity of FeOCl crystalline nanoparticles, and the non-conductive FeOCl nanorods blocking the electrochemical active sites of the carbon substrate. This conductivity decrease further induced the inferior degradation capacity of FeOCl/graphene 3:1, with which 75% of initial BPA concentration remained after 90 minutes of electro-degradation, while FeOCl/graphene 1:1 and graphene electrodes can degrade 46% and 52%, respectively (Figure 50b).

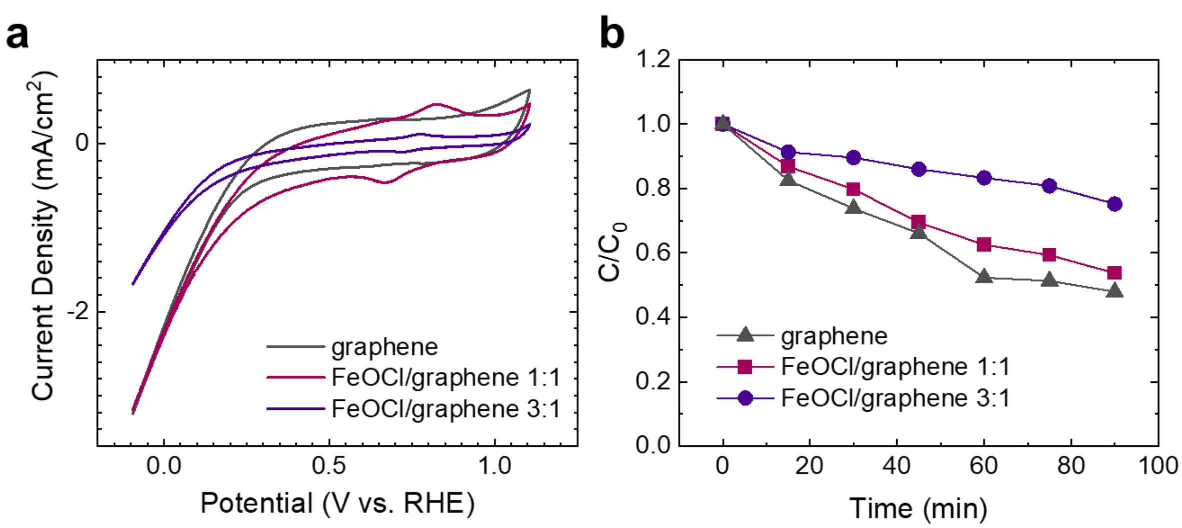

Figure 50. Electrochemical performance of FeOCl-based electrodes.(a) Cyclic voltammetry of FeOCl-based catalytic materials. (b) Degradation profile of FeOCl-based electrodes, where reduction potentials of 0 V vs. RHE (-0.4 V vs. Ag/AgCl) were applied. The electrodes were tested in 20 mL electrolyte (pH = 3.5) containing 0.1 M phosphate buffer, 2 mM H_2O_2, and 50

μM BPA. The numbers in legends (1:1 or 1:3) represented the mass ratios of FeOCl to graphene. All the electrodes had the same geometric area (4 cm^2) and the same catalyst loading (0.25 mg cm^{-2}).

To rule out the interference of the generated H_2O_2 from the oxygen reduction reaction, FeOCl/graphene 1:1 electrode was tested in different gas compositions: nitrogen, oxygen, and no gas purging. The degradation performance in Figure 51a showed that the probable H_2O_2 generated during the process would have limited effect of the BPA oxidation. Figure 51b proved that the BPA adsorbed to the electrode surface was unlikely the major contribution of concentration decrease: less than 7% of BPA was adsorbed in the initial 30 minutes when no external bias was applied, and over 43% of BPA was degraded in the following 60 minutes when 0 V vs. RHE of external bias was applied. The pH values of the electrolytes were maintained for all tests at 3.5.

Compared with other studies using iron-based electro-Fenton electrodes,[19-30] our electrodes did not exhibit superior performance so far. Although the catalyst mass loading and electrode area were both smaller than ones in the other studies, the degradation rates were much slower. We believe that the overall performance could be further improved by the following strategies: 1) creating stronger and more conductive bonding between FeOCl and carbon substrate; 2) optimizing the mass ratio of FeOCl to carbon substrate; 3) utilizing a current collector with larger surface area; 4) designing a flow-through reactor to maximize the contact between contaminant and electrode.

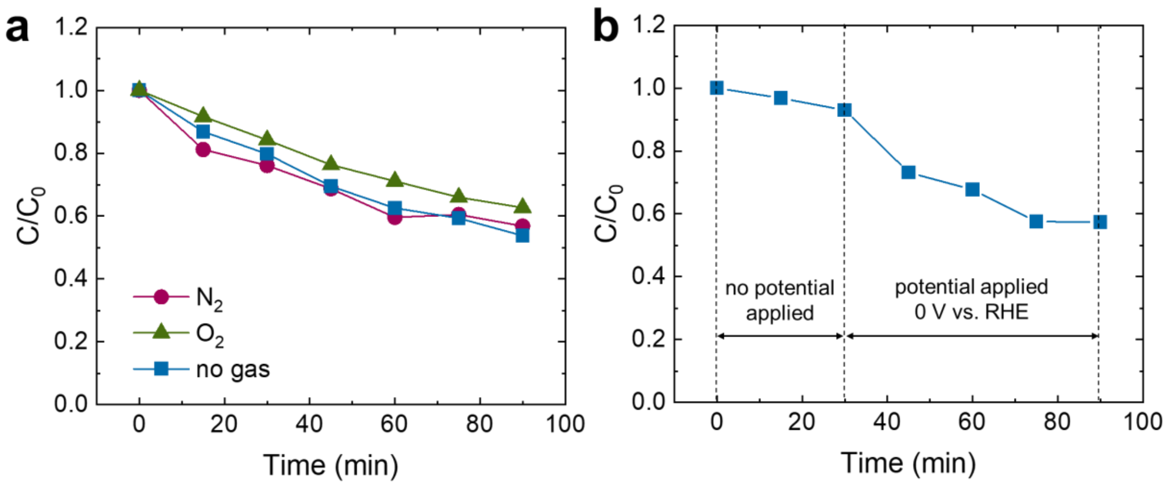

Figure 51. Degradation performance of FeOCl/graphene electrode with different gas compositions and applied potentials.(a) degradation tests with N_2, O_2, and no gas purging. (b) degradation test with no potential applied for the initial 30 minutes and 0 V vs. RHE for the remaining 60 minutes. The electrodes were tested in 20 mL electrolyte (pH = 3.5) containing 0.1 M phosphate buffer, 2 mM H_2O_2, and 50 µM BPA. All the electrodes had the same geometric area (4 cm^2) and the same catalyst loading (0.25 mg cm^{-2}).

7.4 Conclusion

In this chapter, we explored the possibilities of utilizing a heterogeneous Fenton catalyst FeOCl as a potential candidate for both packed bed reactor and electro-Fenton reactor. We successfully attached FeOCl to molecular sieve substrate and the catalytic beads exhibited capacity to degrade high concentration of BPA contaminant for 18 hours in a packed bed reactor. The FeOCl/graphene electrodes were also proven to be able to oxidize BPA.

While the results presented in this chapter are at the very early stage of the proposed objective of the research, the performance are possibly limited by chloride and iron leaching, as well as ineffective bonding between FeOCl and the substrate. Many future research directions need to be executed to advance this research, such as material characterization before and after the test to identify the change of iron coordination environment, investigation of other non-conductive or conductive substrate to maximize FeOCl loading while maintaining and improving the performance, exploration of operation conditions like pH, flow rate, H_2O_2/contaminant concentration, target compound type, etc.

7.5 References

1. Attri, P.; Kim, Y. H.; Park, D. H.; Park, J. H.; Hong, Y. J.; Uhm, H. S.; Kim, K.-N.; Fridman, A.; Choi, E. H. Generation mechanism of hydroxyl radical species and its lifetime prediction during the plasma-initiated ultraviolet (UV) photolysis. *Scientific Reports* **2015,** *5* (1), 9332.

2. GilPavas, E.; Correa-Sanchez, S.; Acosta, D. A. Using scrap zero valent iron to replace dissolved iron in the Fenton process for textile wastewater treatment: Optimization and assessment of toxicity and biodegradability. *Environ Pollut* **2019,** *252*, 1709-1718.

3. Buthiyappan, A.; Raman, A. A. A. Energy intensified integrated advanced oxidation technology for the treatment of recalcitrant industrial wastewater. *J Clean Prod* **2019,** *206*, 1025-1040.

4. Kurt, U.; Apaydin, O.; Gonullu, M. T. Reduction of COD in wastewater from an organized tannery industrial region by Electro-Fenton process. *J Hazard Mater* **2007,** *143* (1-2), 33-40.

5. Xu, P.; Xu, H.; Zheng, D. Y. The efficiency and mechanism in a novel electro-Fenton process assisted by anodic photocatalysis on advanced treatment of coal gasification wastewater. *Chemical Engineering Journal* **2019,** *361*, 968-974.

6. Barndok, H.; Blanco, L.; Hermosilla, D.; Blanco, A. Heterogeneous photo-Fenton processes using zero valent iron microspheres for the treatment of wastewaters contaminated with 1,4-dioxane. *Chemical Engineering Journal* **2016,** *284*, 112-121.

7. Melero, J. A.; Martinez, F.; Botas, J. A.; Molina, R.; Pariente, M. I. Heterogeneous catalytic wet peroxide oxidation systems for the treatment of an industrial pharmaceutical wastewater. *Water Res* **2009,** *43* (16), 4010-4018.

8. Sun, M.; Chu, C.; Geng, F.; Lu, X.; Qu, J.; Crittenden, J.; Elimelech, M.; Kim, J.-H. Reinventing fenton chemistry: iron oxychloride nanosheet for pH-insensitive H2O2 activation. *Environmental Science & Technology Letters* **2018**.

9. Zhang, S.; Sun, M.; Hedtke, T.; Deshmukh, A.; Zhou, X.; Weon, S.; Elimelech, M.; Kim, J.-H. Mechanism of Heterogeneous Fenton Reaction Kinetics Enhancement under Nanoscale Spatial Confinement. *Environ Sci Technol* **2020,** *54* (17), 10868-10875.

10. Ji, X. X.; Wang, H. F.; Hu, P. J. First principles study of Fenton reaction catalyzed by FeOCl: reaction mechanism and location of active site. *Rare Metals* **2019,** *38* (8), 783-792.

11. Sun, M.; Chu, C.; Geng, F.; Lu, X.; Qu, J.; Crittenden, J.; Elimelech, M.; Kim, J.-H. Reinventing Fenton chemistry: Iron oxychloride nanosheet for pH-insensitive H_2O_2 activation. *Environ. Sci. Technol. Lett.* **2018,** *5* (3), 186-191.

12. Duarte, F.; Morais, V.; Maldonado-Hódar, F. J.; Madeira, L. M. Treatment of textile effluents by the heterogeneous Fenton process in a continuous packed-bed reactor using Fe/activated carbon as catalyst. *Chemical Engineering Journal* **2013,** *232*, 34-41.

13. Mesquita, I.; Matos, L. C.; Duarte, F.; Maldonado-Hódar, F. J.; Mendes, A.; Madeira, L. M. Treatment of azo dye-containing wastewater by a Fenton-like process in a continuous packed-bed reactor filled with activated carbon. *J Hazard Mater* **2012,** *237-238*, 30-37.

14. Zhang, C.; Ren, G.; Wang, W.; Yu, X.; Yu, F.; Zhang, Q.; Zhou, M. A new type of continuous-flow heterogeneous electro-Fenton reactor for Tartrazine degradation. *Separation and Purification Technology* **2019,** *208*, 76-82.

15. Shao, Y.; Chen, H. Heterogeneous Fenton oxidation of phenol in fixed-bed reactor using Fe nanoparticles embedded within ordered mesoporous carbons. *Chemical Engineering Research and Design* **2018,** *132*, 57-68.

16. Xu, J.; Zheng, X.; Feng, Z.; Lu, Z.; Zhang, Z.; Huang, W.; Li, Y.; Vuckovic, D.; Li, Y.; Dai, S.; Chen, G.; Wang, K.; Wang, H.; Chen, J. K.; Mitch, W.; Cui, Y. Organic wastewater treatment by a single-atom catalyst and electrolytically produced H2O2. *Nature Sustainability* **2021,** *4* (3), 233-241.

17. Fida, H.; Zhang, G.; Guo, S.; Naeem, A. Heterogeneous Fenton degradation of organic dyes in batch and fixed bed using La-Fe montmorillonite as catalyst. *Journal of Colloid and Interface Science* **2017,** *490*, 859-868.

18. di Luca, C.; Massa, P.; Fenoglio, R.; Cabello, F. M. Improved Fe2O3/Al2O3 as heterogeneous Fenton catalysts for the oxidation of phenol solutions in a continuous reactor. *Journal of Chemical Technology & Biotechnology* **2014,** *89* (8), 1121-1128.

19. Liu, D.; Zhang, H.; Wei, Y.; Liu, B.; Lin, Y.; Li, G.; Zhang, F. Enhanced degradation of ibuprofen by heterogeneous electro-Fenton at circumneutral pH. *Chemosphere* **2018,** *209*, 998-1006.

20. Lu, J.-Y.; Yuan, Y.-R.; Hu, X.; Liu, W.-J.; Li, C.-X.; Liu, H.-Q.; Li, W.-W. MOF-Derived Fe2O3/Nitrogen/Carbon Composite as a Stable Heterogeneous Electro-Fenton Catalyst. *Industrial & Engineering Chemistry Research* **2020,** *59* (5), 1800-1808.

21. Dong, P.; Wang, H.; Liu, W.; Wang, S.; Wang, Y.; Zhang, J.; Lin, F.; Wang, Y.; Zhao, C.; Duan, X.; Wang, S.; Sun, H. Quasi-MOF derivative-based electrode for efficient electro-Fenton oxidation. *J Hazard Mater* **2021,** *401*, 123423.

22. Xu, D.; Song, X.; Qi, W.; Wang, H.; Bian, Z. Degradation mechanism, kinetics, and toxicity investigation of 4-bromophenol by electrochemical reduction and oxidation with Pd–Fe/graphene catalytic cathodes. *Chemical Engineering Journal* **2018,** *333*, 477-485.

23. Gao, G.; Zhang, Q.; Hao, Z.; Vecitis, C. D. Carbon Nanotube Membrane Stack for Flow-through Sequential Regenerative Electro-Fenton. *Environ Sci Technol* **2015,** *49* (4), 2375-2383.

24. Fdez-Sanromán, A.; Acevedo-García, V.; Pazos, M.; Sanromán, M. Á.; Rosales, E. Iron-doped cathodes for electro-Fenton implementation: Application for pymetrozine degradation. *Electrochimica Acta* **2020,** *338*, 135768.

25. Zhao, H.; Qian, L.; Guan, X.; Wu, D.; Zhao, G. Continuous Bulk FeCuC Aerogel with Ultradispersed Metal Nanoparticles: An Efficient 3D Heterogeneous Electro-Fenton Cathode over a Wide Range of pH 3–9. *Environ Sci Technol* **2016,** *50* (10), 5225-5233.

26. Li, Z.; Shen, C.; Liu, Y.; Ma, C.; Li, F.; Yang, B.; Huang, M.; Wang, Z.; Dong, L.; Wolfgang, S. Carbon nanotube filter functionalized with iron oxychloride for flow-through electro-Fenton. *Applied Catalysis B: Environmental* **2020,** *260*, 118204.

27. Tang, H.; Zhu, Z.; Shang, Q.; Tang, Y.; Zhang, D.; Du, Y.; Liu, M.; Yin, K.; Liu, C. Highly Efficient Continuous-Flow Electro-Fenton Treatment of Antibiotic Wastewater Using a Double-Cathode System. *ACS Sustainable Chemistry & Engineering* **2021,** *9* (3), 1414-1422.

28. Liu, Z.; Wan, J.; Ma, Y.; Wang, Y. In situ synthesis of FeOCl@MoS2 on graphite felt as novel electro-Fenton cathode for efficient degradation of antibiotic ciprofloxacin at mild pH. *Chemosphere* **2021,** *273*, 129747.

29. Ghasemi, M.; Khataee, A.; Gholami, P.; Soltani, R. D. C.; Hassani, A.; Orooji, Y. In-situ electro-generation and activation of hydrogen peroxide using a CuFeNLDH-CNTs modified graphite cathode for degradation of cefazolin. *Journal of Environmental Management* **2020,** *267*, 110629.

30. Weng, C.; Chuang, Y.-H.; Davey, B.; Mitch, W. A. Reductive Electrochemical Activation of Hydrogen Peroxide as an Advanced Oxidation Process for Treatment of Reverse Osmosis Permeate during Potable Reuse. *Environ Sci Technol* **2020,** *54* (19), 12593-12601.

31. Huang, L.-Z.; Zhu, M.; Liu, Z.; Wang, Z.; Hansen, H. C. B. Single sheet iron oxide: An efficient heterogeneous electro-Fenton catalyst at neutral pH. *J Hazard Mater* **2019,** *364*, 39-47.

32. Rosenfeldt, E. J.; Linden, K. G. Degradation of Endocrine Disrupting Chemicals Bisphenol A, Ethinyl Estradiol, and Estradiol during UV Photolysis and Advanced Oxidation Processes. *Environ Sci Technol* **2004,** *38* (20), 5476-5483.

33. Schecter, A.; Malik, N.; Haffner, D.; Smith, S.; Harris, T. R.; Paepke, O.; Birnbaum, L. Bisphenol A (BPA) in U.S. Food. *Environ Sci Technol* **2010,** *44* (24), 9425-9430.

34. Stefánsson, A. Iron (III) hydrolysis and solubility at 25 degrees C. *Environ Sci Technol* **2007,** *41* (17), 6117-23.

Chapter 8: Summary and Outlook

8.1 Summary of Research and Novel Contributions

The work presented in this dissertation has developed new anthraquinone-based catalysts for H_2O_2 electrosynthesis and their applications in advanced oxidation process. The integrated efforts including catalysis synthesis, electrode and reactor design, and system integration are made to achieve the final goal of autonomous, modular, and electrified next-generation water treatment system. Chapter 2 presented the background and fundamentals of the industrial process, state-of-the-art electrocatalysts, electrode architecture, electrochemical cell design, and advanced oxidation process. Based on the short literature review, the research objectives and hypotheses were stated in Chapter 3.

Chapter 4 and 5 explored two types of conductive substrates on which anthraquinone molecular catalysts can be attached to and thus the homogeneous chemistry can be transferred to the heterogeneous chemistry: polymeric carbon nitride (Chapter 4) and polyaniline (Chapter 5). The electrocatalytic activities, Faradaic efficiencies, and H_2O_2 generation rates were tested and compared. Chapter 4 also explored the possibility of utilizing the same synthesis method and architecture to construct a spatially-separated photocatalyst system. Polyaniline-anthraquinone composite material exhibited a much higher activity and selectivity compared with carbon nitride-anthraquinone composite material due to PANI's higher intrinsic conductivity and larger number of terminal amine groups, which leads to the higher AQ mass loading.

Chapter 6 discussed the advantages of adopting gas diffusion electrodes for H_2O_2 electrosynthesis, which could greatly enhance oxygen mass transfer at the triple-phase boundary layer. Both AQ-C_3N_4 and AQ-PANI electrocatalysts were tested and compared in the immersed electrode setup and the gas diffusion electrode setup, and the GDE design could significantly improve both the Faradaic efficiency and the electrocatalytic activity due to the more efficient gas transport at the electrode interface. The GDE-based flow cell was further tested with more complicated conditions, such as different gas compositions and simulated water matrices, to demonstrate the system's adaptability. Energy analyses based on the experimental results proved that the electrical energy consumption of H_2O_2 generation is relatively small compared with the energy consumption of the benchmark technology for H_2O_2 activation, UV irradiation. Depends on the water compositions and treatment objectives, two flow process designs were proposed so the whole procedure could be tailored for higher efficiency.

The more energy and chemical-efficient H_2O_2 activation method based on iron oxychloride was proposed in Chapter 7, where FeOCl was constructed as the packed bed heterogeneous catalyst and the electrocatalyst. The preliminary results proved the feasibility of the concept, while a few research directions need to be continued to realize the design goals.

The novel contributions made by this research can be outlined as follows:

- The development of a facile, one-step synthesis method to attach anthraquinone molecular catalyst to various conductive substrates
- The synthesis of anthraquinone-based electrocatalysts that can effectively and efficiently produce H_2O_2 with high activity and selectivity
- The fabrication of modular and electrified hydrogen peroxide generation cell and the verification of its ability to generate H_2O_2 at high concentration stably and constantly
- The preparation of iron oxychloride-based heterogeneous catalyst in packed bed reactor and electrocatalyst for efficient H_2O_2 activation and contaminant degradation

8.2 Future Directions and Outlook

Moving forward, there are many additional researches that could be done to achieve the final goal of electrified, modular, autonomous, and decentralized water treatment devices. Besides the research covered by this thesis, many other studies have been conducted to focus on hydrogen peroxide electrosynthesis only, while many are not applicable for water treatment, and significant fundamental questions remain unanswered. Many studies developed efficient 2-e^- ORR catalysts using synthetic electrolytes with high ionic strength and idealized experimental conditions, such as those described in Table 1, Table 3, and Table 4. Most ORR studies focus on the cathodic reaction only, neglecting parasitic reactions possible in any complex water matrix, such as metal ions being reduced at the cathode side and halogenated organic compounds being formed at the anode side. Almost all H_2O_2 research neglect the occurrence of organic matter that can foul electrodes and diminish the performance. They also neglect potential binding on divalent cations and potential precipitation and scale formation on oxygen reduction centers especially due to local high pH resulting from ORR. We recognize that the effective translation of research-related heuristics into practical technologies requires the broad consideration of all relevant challenges instead of centering on a singular problem from an isolated standpoint (*e.g.*, focusing on new electrode material performance without taking into account water stream composition and various process options). Thus, a comprehensive evaluation of process flow options, cell design, catalyst and electrode materials, and the impacts of feedwater to determine system practicality and long-term robustness will be necessary to be conducted simultaneously to advance. This optimization shall be accompanied by systems-level strategies and techno-economic analysis to maximize the economic benefits and to ensure that our invention achieves pipe parity in small-scale distributed water treatment systems.

Once the reactor is designed and tested in more realistic conditions, its capacity needs to be increased from lab-sale to industrial-scale, which process requires careful analysis of geometric, kinematic, thermal, chemical, and electrical similarities.[1] The geometric similarity can be achieved by balancing between increasing the electrode size of each cell at the expense of reduced mass transfer and increasing the number of cells at higher cost. Kinematic and chemical similarities will be achieved by maintaining similar gas and liquid flow velocities across electrode surfaces. For large cells, it is important to achieve thermal similarity by minimizing internal resistance (e.g., distance between electrodes and ion exchange membrane) and therefore minimizing the Ohmic heating. The most important and challenging criteria of electrochemical reactor scale-up is electrical similarity, which can be described by Wagner number ($Wa = (k/L)(dV/di)$), where k is the electrolyte conductivity, L is the characteristic length, V is the electrode potential, and i is the current density. It is critical to maintain a uniform current distribution over the electrode surface as these variables change with increasing dimension. With the scaled-up prototypes, the performance measures such as current efficiency, chemical yield, space-time yield, and energy yield need to be systematically evaluated to optimize the design and operating conditions,[2] for a comprehensive techno-economic analysis based on experimental data and consideration of changes in electricity cost and potential use of renewable energy.

We envision a set of working prototypes that can be applied to a wide range of source water types and end-user scenarios. The cells and reactors can be tailored for different application scenarios – *i.e.*, fit-for-purpose AOP modules depending on the types of wastewater and treatment goals. Different process flow options, design options for H_2O_2 synthesis cell and

AOP reactor, and catalyst material options need to be carefully screened under a range of operating conditions. An in-depth fundamental study needs to be performed on the factors that negatively impact the cell/reactor performance and develop a holistic strategy to overcome these limitations.

8.5 References

1. Abbar, A. H. S. a. A. H. Scale-Up of Electrochemical Reactors. *InTechOpen* **2012**.

2. Goodridge, F.; Scott, K. Electrolytic Reactor Design, Selection, and Scale-up. In *Electrochemical Process Engineering: A Guide to the Design of Electrolytic Plant*, Goodridge, F.; Scott, K., Eds. Springer US: Boston, MA, 1995; pp 177-244.